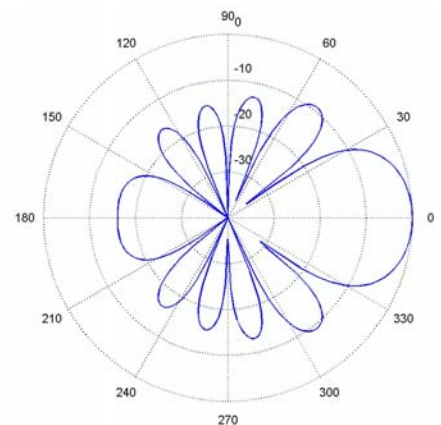
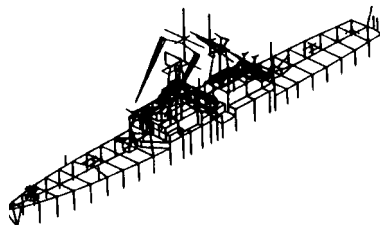
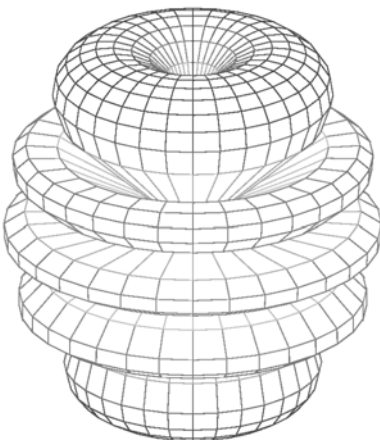
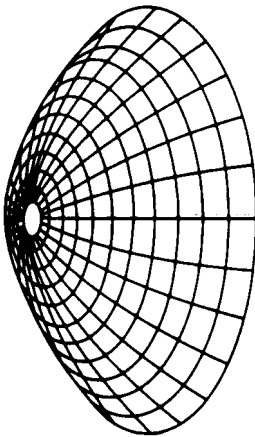
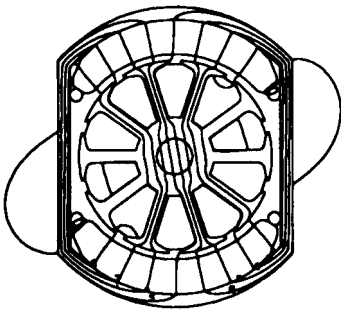
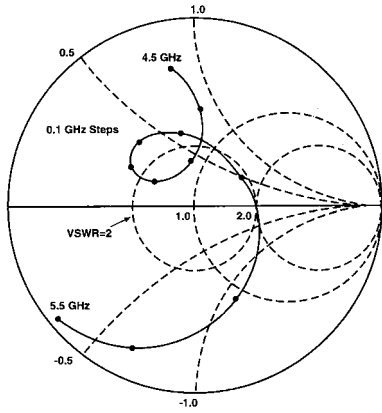


# Applied Computational Electromagnetics Society Journal



Editor-in-Chief  
Ataf Z. Elsherbeni

November 2003  
Vol. 18 No. 3  
ISSN 1054-4887

**GENERAL PURPOSE AND SCOPE:** The Applied Computational Electromagnetics Society (*ACES*) Journal hereinafter known as the *ACES Journal* is devoted to the exchange of information in computational electromagnetics, to the advancement of the state-of-the art, and the promotion of related technical activities. A primary objective of the information exchange is the elimination of the need to “re-invent the wheel” to solve a previously-solved computational problem in electrical engineering, physics, or related fields of study. The technical activities promoted by this publication include code validation, performance analysis, and input/output standardization; code or technique optimization and error minimization; innovations in solution technique or in data input/output; identification of new applications for electromagnetics modeling codes and techniques; integration of computational electromagnetics techniques with new computer architectures; and correlation of computational parameters with physical mechanisms.

**SUBMISSIONS:** The *ACES Journal* welcomes original, previously unpublished papers, relating to applied computational electromagnetics. Typical papers will represent the computational electromagnetics aspects of research in electrical engineering, physics, or related disciplines. However, papers which represent research in applied computational electromagnetics itself are equally acceptable.

Manuscripts are to be submitted through the upload system of *ACES* web site <http://aces.ee.olemiss.edu> See “Information for Authors” on inside of back cover and at *ACES* web site. For additional information contact the Editor-in-Chief:

**Dr. Atef Elsherbeni**  
Department of Electrical Engineering  
The University of Mississippi  
University, MS 386377 USA  
Phone: 662-915-5382 Fax: 662-915-7231  
Email: [atef@olemiss.edu](mailto:atef@olemiss.edu)

**SUBSCRIPTIONS:** All members of the Applied Computational Electromagnetics Society who have paid their subscription fees are entitled to receive the *ACES Journal* with a minimum of three issues per calendar year and are entitled to download any published journal article available at <http://aces.ee.olemiss.edu>.

**Back issues**, when available, are \$15 each. Subscriptions to *ACES* is through the web site. Orders for back issues of the *ACES Journal* and changes of addresses should be sent directly to *ACES* Executive Officer:

**Dr. Richard W. Adler**  
ECE Department, Code ECAB  
Naval Postgraduate School  
833 Dyer Road, Room 437  
Monterey, CA 93943-5121 USA  
Fax: 831-649-0300  
Email: [rwa@attglobal.net](mailto:rwa@attglobal.net)

Allow four week’s advance notice for change of address. Claims for missing issues will not be honored because of insufficient notice or address change or loss in mail unless the Executive Officer is notified within 60 days for USA and Canadian subscribers or 90 days for subscribers in other countries, from the last day of the month of publication. For information regarding reprints of individual papers or other materials, see “Information for Authors”.

**LIABILITY.** Neither *ACES*, nor the *ACES Journal* editors, are responsible for any consequence of misinformation or claims, express or implied, in any published material in an *ACES Journal* issue. This also applies to advertising, for which only camera-ready copies are accepted. Authors are responsible for information contained in their papers. If any material submitted for publication includes material which has already been published elsewhere, it is the author’s responsibility to obtain written permission to reproduce such material.

# **APPLIED COMPUTATIONAL ELECTROMAGNETICS SOCIETY JOURNAL**

Editor-in-Chief  
Atf Z. Elsherbeni

November 2003  
Vol. 18 No. 3

ISSN 1054-4887

**The ACES Journal is abstracted in INSPEC, in Engineering Index, and in DTIC.**

The first, fourth, and sixth illustrations on the front cover have been obtained from the Department of Electrical Engineering at the University of Mississippi.

The third and fifth illustrations on the front cover have been obtained from Lawrence Livermore National Laboratory.

The second illustration on the front cover has been obtained from FLUX2D software, CEDRAT S.S. France, MAGSOFT Corporation, New York.

**THE APPLIED COMPUTATIONAL ELECTROMAGNETICS SOCIETY**  
**<http://aces.ee.olemiss.edu>**

**ACES JOURNAL EDITORS**

**EDITOR-IN-CHIEF/ACES/JOURNAL**  
**Atef Elsherbeni**  
University of Mississippi, EE Dept.  
University, MS 38677, USA

**ASSOCIATE EDITOR-IN-CHIEF**  
**Alexander Yakovlev**  
University of Mississippi, EE Dept.  
University, MS 38677, USA

**MANAGING EDITOR**  
**Richard W. Adler**  
833 Dyer Rd, Rm 437 EC/AB  
NPS, Monterey, CA 93943-5121, USA

**EDITORIAL ASSISTANT**  
**Matthew J. Inman**  
University of Mississippi, EE Dept.  
University, MS 38677, USA

**EDITOR-IN-CHIEF, EMERITUS**  
**Ducan C. Baker**  
EE Dept. U. of Pretoria  
0002 Pretoria, South Africa

**EDITOR-IN-CHIEF, EMERITUS**  
**Robert M. Bevensee**  
Box 812  
Alamo, CA 94507-0516, USA

**EDITOR-IN-CHIEF, EMERITUS**  
**David E. Stein**  
USAF Scientific Advisory Board  
Washington, DC 20330, USA

**EDITOR-IN-CHIEF, EMERITUS**  
**Allen Glisson**  
University of Mississippi, EE Dept.  
University, MS 38677, USA

**EDITOR-IN-CHIEF, EMERITUS**  
**Ahmed Kishk**  
University of Mississippi, EE Dept.  
University, MS 38677, USA

**ACES JOURNAL ASSOCIATE EDITORS**

**Giandomenico Amendola**  
Universita' della Calabria  
Rende , Italy

**Chun-Wen Paul Huang**  
Anadigics, Inc.  
Warren, NJ, USA

**Edmund K. Miller**  
LASL  
Santa Fe, NM, USA

**John Beggs**  
NASA Langley Research Center  
Hampton, VA, USA

**Todd H. Hubing**  
University of Missouri-Rolla  
Rolla, MO, USA

**Krishna Naishadham**  
Wright State University  
Dayton, OH, USA

**John Brauer**  
Ansoft Corporation  
Milwaukee, WI, USA

**Nathan Ida**  
The University of Akron  
Akron, OH, USA

**Giuseppe Pelosi**  
University of Florence  
Florence, Italy

**Magda El-Shenawee**  
University of Arkansas  
Fayetteville AR, USA

**Yasushi Kanai**  
Niigata Institute of Technology  
Kashiwazaki, Japan

**Vicente Rodriguez**  
ETS-Lindgren  
Cedar Park, TX, USA

**Pat Foster**  
Microwave & Antenna Systems  
Gt. Malvern, Worc. UK

**Leo C. Kempel**  
Michigan State University  
East Lansing MI, USA

**Harold A. Sabbagh**  
Sabbagh Associates  
Bloomington, IN, USA

**Cynthia M. Furse**  
Utah State University  
Logan UT, USA

**Andrzej Krawczyk**  
Institute of Electrical Engineering  
Warszawa, Poland

**John B. Schneider**  
Washington State University  
Pullman, WA, USA

**Christian Hafner**  
Swiss Federal Inst. of Technology  
Zurich, Switzerland

**Stanley Kubina**  
Concordia University  
Montreal, Quebec, Canada

**Abdel Razek Sebak**  
University of Manitoba  
Winnipeg, MB, Canada

**Michael Hamid**  
University of South Alabama,  
Mobile, AL, USA

**Samir F. Mahmoud**  
Kuwait University  
Safat, Kuwait

**Amr M. Sharawee**  
American University  
Cairo, Egypt

**Andy Harrison**  
Radiance  
Huntsville, AL

**Ronald Marhefka**  
Ohio State University  
Columbus, OH, USA

**Norio Takahashi**  
Okayama University  
Tsushima, Japan

# THE APPLIED COMPUTATIONAL ELECTROMAGNETICS SOCIETY

## JOURNAL

Vol. 18 No. 3

November 2003

### TABLE OF CONTENTS

“Bistatic Scatterer and Antenna Imaging” S. Inge.....	136
“Reducing Electromagnetic Coupling in Shielded Enclosures using a Genetic Algorithm – Finite-Difference Time-Domain Solver” R. I. Macpherson and N. J. Ryan.....	144
“Impact of Some Discontinuities on the Convergence of Numerical Methods in Electromagnetics” M. M. Bibby.....	151
“Wireless Propagation in Non Line of Sight Urban Areas using Uniform Theory of Diffraction” G. A. Ellis.....	162
“Automatic Calculation of Band Diagrams of Photonic Crystals Using the Multiple Multipole Method” J. Smajic, C. Hafner, and D. Erni.....	172
“Analysis of Conventional and Novel Delay Lines: A Numerical Study” O. Ramahi.....	181
“An Empirical Approach for Design of Wideband, Probe-Fed, U-Slot Microstrip Patch Antennas on Single-layer, Infinite, Grounded Substrates” V. Natarajan and D. Chatterjee.....	191
“Utilizing Particle Swarm Optimization in the Field Computation of Non-Linear Magnetic Media” A. A. Adly and S.K. Abd-El-Hafiz.....	202
“An Approach to Multi-Resolution in Time Domain Based on the Discrete Wavelet Transform” C. Represa, C. Pereira, A.C.L. Cabeceira, I Barba, and J. Represa.....	210



## BISTATIC SCATTERER AND ANTENNA IMAGING

Steve Inge (in-j)

Broadcast Communications Ltd.

P.O. Box 98, Wellington, New Zealand

**ABSTRACT:** Two computing techniques to create an image of the radiating centres on an antenna or scatterer using Fourier optics is presented.

---

*Steve Inge died on October 24, 2002 at the age of 61 after this article was submitted for publication. The reviewers accepted this article subject to revisions. Since that is not possible, this article is published as submitted.*

*The late Ian McEnnis, Chief Antenna Engineer at Broadcast Communications Limited in New Zealand, and one of Steve's colleagues, notified us of his death and had the following remembrances of Steve, which we print below.*

*Steve had been with our organization for 42 years. His immense intellect enabled him to become a "guru" in any area he focused on. Most of BCL's in house engineering software has been developed by Steve. BCLIPPS (BCL's Interactive Planning and Propagation Software) was Steve's crowning. It has formed the basis of our coverage work for the past 10 years and has enabled us to be a leader in this area. Steve was the engineer who solved the most difficult of problems and he was the one his colleagues turned to when they were having difficulty. His mathematical ability was awesome and once he got his teeth into a problem he would not let it go until he had it sorted. There is nothing Steve liked more than to share his knowledge with others. Having said all that, in the end Steve was just a "good bloke" who will be sorely missed by many.*

---

### Introduction

Bistatic k-space (BSKS) imaging from antenna currents was introduced by John Shaeffer et al (Ref 1). It is a technique to graphically show the active

radiating centers on a conducting body. The currents on the body are found using either a computer program or measurements, for a particular excitation. The excitation may be a plane wave being scattered by the body, or sources on the body for an antenna. This paper describes two simple approaches to imaging a radiator.

### Brief Overview

The radiation emanating from any antenna (or scatterer) may be visualised by simple operations upon the antenna currents. First choose the far field direction from which to look at the antenna. Create a plane surface at the antenna, normal to the look direction. Project all of the antenna currents onto this surface, adjusting the phase as necessary, to maintain the same phases and polarisation in the far field. Filter the current image on the surface by removing all spatial frequencies above one cycle per wavelength. Display the current intensity as brightness in a 2D graphic image, which will show which parts of the antenna are "glowing" when viewed from this direction. This is repeated for both polarisations, which may be combined into a single total radiation image if desired.

### Imaging theory

How does it work? By flattening the currents on to a surface we create a two dimensional current plane. If

we now take the Fourier transform (FT) of this current surface, we create a new description of the currents. The FT creates a set of sinusoidal waves equivalent to the original currents. Since the currents occupied a finite area on the surface, the FT range is infinite. Each point on the FT surface represents a particular uniform linear phase advance, and thus represents a plane wave propagating in a single direction. This is known as a plane wave spectrum of the radiation. The  $F_x$ ,  $F_y$  positions on the spectrum are the direction cosines of the plane wave direction. The  $z$  component of the radiation is  $F_z = \sqrt{1 - (F_x^2 + F_y^2)}$ . The centre of the plane (0,0) is constant phase, which creates a wavefront propagating toward the look direction. When  $F_x^2 + F_y^2 = 1$ , the wave direction is normal to the look direction. All points on this unit circle correspond to a phase advance of one cycle per wavelength. The spectrum outside this circle gives direction cosines  $> 1$ , indicating imaginary angles. This energy does not radiate, but represents evanescent waves which eventually return to the antenna as reactive energy. (Ref.3)

The antenna image is created by projecting the currents onto a normal plane, and removing spatial frequencies greater than one cycle per wavelength. The latter process may be achieved by setting the FT spectrum to zero at all points outside the one cycle per wavelength circle and inverse FT, or equivalently by convolving the current surface with the  $J_1(\pi\rho)/(\pi\rho)$  point spread function (PSF), where  $J_1()$  is the Bessel function of the first kind and order one, and  $\rho$  is the radius. This point spread function is known from optics as the Airy disk.

The image is a view of the far field antenna radiation toward the look direction. For scatterers, the look direction may be the same as the incident illumination, which is the monostatic (single antenna) radar case. Similarly, when the look direction is different to the illumination direction, we have the bistatic (separate antennas) radar case.

### Imaging process

1. Given the locations and currents of wire segments, from a NEC (Ref 4) analysis for example, calculate the contribution to far field (Efar) for each segment, in a chosen (theta, phi) radiation direction. The two polarisations are treated separately. The contribution from a single segment is

$$\Delta E_p = j30kI \exp(jk\hat{R} \cdot \vec{S}) \{ (\hat{R} \cdot \Delta \vec{L}) \hat{R} - \Delta \vec{L} \} \cdot \hat{p} \quad (1)$$

where  $\hat{p}$  is the chosen polarisation unit vector,  $I$  is the current,  $\Delta \vec{L}$  is the segment length vector,  $\hat{R}$  is the far field direction unit vector,  $\vec{S}$  is the coordinate vector of the segment centre and  $k$  is the wave number  $2\pi/\lambda$ . Note that the  $1/r$  distance factor is omitted, making the units in volts. This is the same operation as calculating the far field radiation pattern, without summing the voltages. The code can be extracted from a suitable antenna program far field radiation pattern routine.

2. Each segment is replaced with an isotropic source in the same location, with the magnitude and phase of the Efar contribution to the chosen polarisation. By placing this light source at each point, we create an image, viewable from any direction. At this point all the detail can be seen, so that wires with



rapidly varying phase from a particular viewpoint are visible. This does not agree with radiation reality.

3. Filter the image to remove spatial frequencies above one cycle per wavelength. This physical limit is due solely to the wave nature of light. Note that even the tiniest point source appears as a circular blob, surrounded by faint rings, known as the Airy disk. The Airy disk has the form of  $J_1(u)/u$ , where  $J_1$  is the Bessel function of the first kind and order 1. The resolution limit is the Raleigh criterion of 0.61 wavelength, which is where the maximum of one Airy disk overlaps with the first minimum of another.

Starting with the Efar elements, we Fast Fourier Transform (FFT) the (1D, 2D, or 3D) space, remove all spatial frequencies above one cycle per wavelength, and inverse FFT. The wanted spatial frequencies are found in the line, circle or sphere sectors in the corners of the transformed matrix, the remainder are set to zero.

4. Now the image appears as it would in our "microwave microscope". Note that optical microscopes have the same limit to magnification, where a point is reached where more magnification just gives more blur. Hence the move to higher frequencies and electron microscopes. These images may be named radio wave photographs, since they show the luminosity of each part of the antenna or scatterer.

**Example** Consider a long wire with a sinusoidal standing or traveling wave current pattern. If we view

the currents from broadside, we can see the alternating pattern. However if we apply the blur filter, we find that at all internal points along the wire, the cyclic currents integrate to zero. Only at the ends is the last current pattern not cancelled by its neighbour, so we see a bright spot centred on each wire end. This illustrates the maxim "radiation is due to the acceleration of charge". See the first example below.

### ***Taper windows***

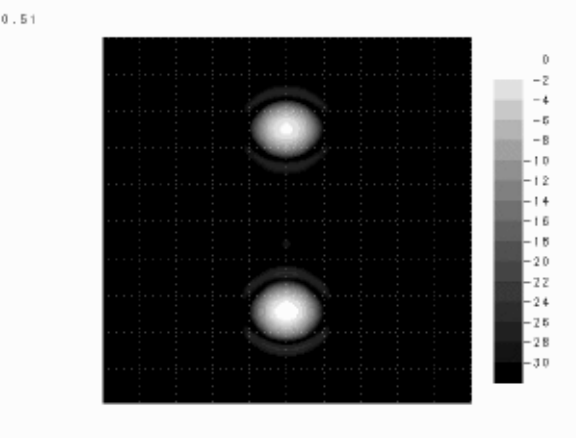
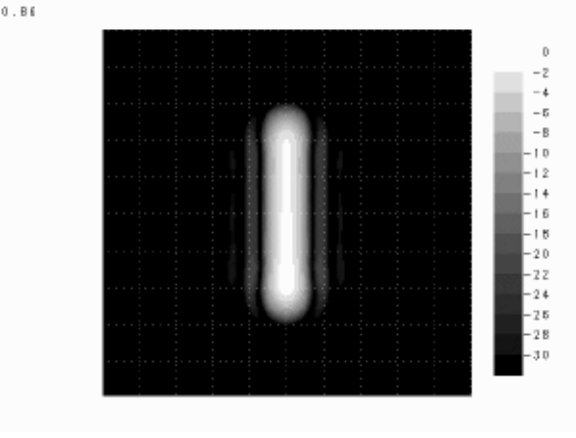
Tapering of the spatial window illumination reduces both resolution and sidelobe levels. The taper function used is  $(1 - \rho^2)^p$  where rho is the fraction of the window radius, and  $p$  is the taper exponent. In 2D, the resulting blur function form is  $J_{p+1}(u)/u^{p+1}$  giving both reduced resolution and sidelobe levels as  $p$  increases.  $p = 0$  for uniform illumination,  $p = 1$  for parabolic taper, etc.

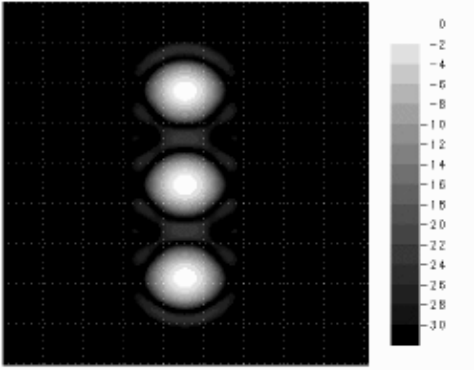
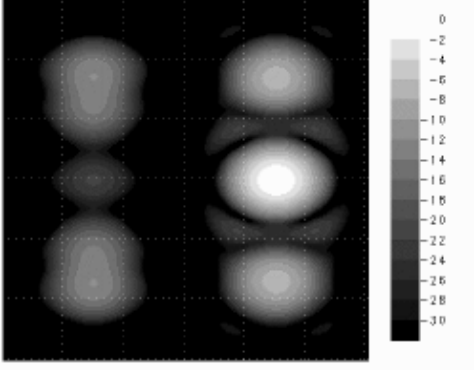
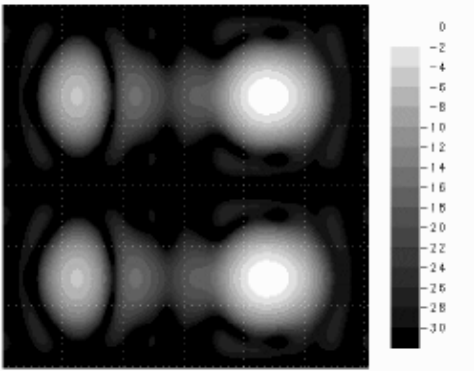
### ***Example radio wave photographs***

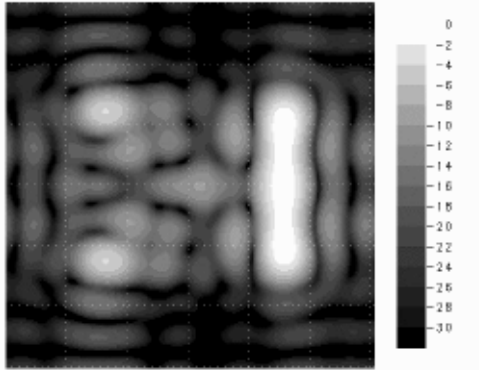
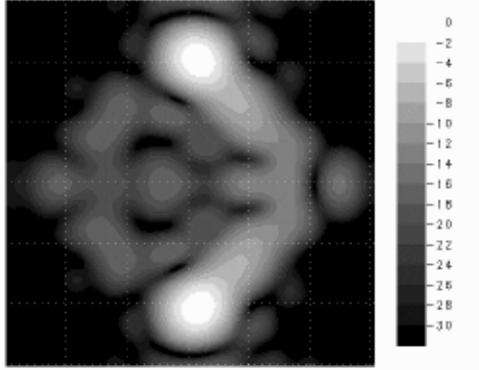
The grey scale is in decibels. The number at top left of each image is the maximum "brightness" across the image. The look direction for all the images is from the zenith,  $\theta = 0$ ,  $\phi = 1^\circ$ . The small  $\phi$  offset is to ensure that the polarisation is properly defined. All these images used NEC-2 to calculate the current distributions. Unless specified, horizontal (Ephi) polarisation is used. The faint grid lines are spaced one wavelength apart. A multidimensional mixed radix FFT is used (Ref 5), with each image as 200x200 pixels. In the largest image spaces the pixel size is  $\lambda/20$ .

**Table 1. Window Taper Performance**

Taper Exponent $p$	0	1	2	3	4	5	6	7
Relative beam width	1	1.10	1.21	1.34	1.47	1.62	1.78	1.94
Sidelobe level dB.	-17	-24	-30	-36	-41	-46	-50	-54

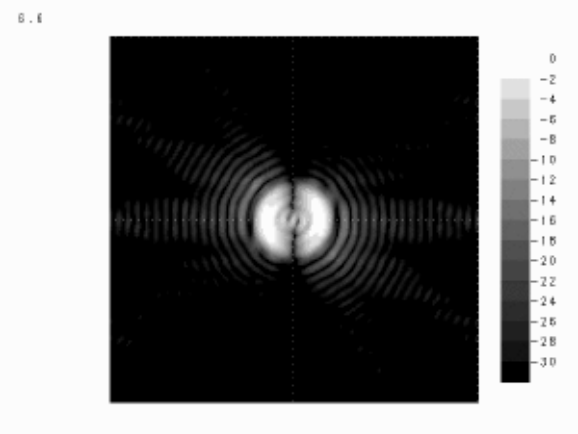
<p>Long wire, end fed</p> <p>This image is taken from broadside to a 5 wavelength wire, fed near the bottom end. The broadside radiation pattern is formed by the interference of the radiation from the two end points.</p> <p>(Image size <math>10 \lambda</math> square)</p>	
<p>Long wire, end fed, radiation in main lobe.</p> <p>This image shows the radiation in the direction of the main lobe, from all along the wire. The contribution decreases from the feed point toward the far end.</p> <p>(Image size <math>10 \lambda</math> square)</p>	

<p>Long wire, centre fed, broadside radiation.</p> <p>This is the same 5 wavelength wire, but centre fed. The current discontinuity causes radiation from the feed point as well as the end points. (Image size = <math>10\lambda</math> square)</p>	<p>0.25</p> 
<p>Loop, radiation towards far right.</p> <p>This is a <math>3 \times 3 \lambda</math> square loop antenna, in the horizontal plane. The radiation from the feed point, and from the four corners is visible. (Image size <math>6 \lambda</math>)</p>	<p>4.86E-02</p> 
<p>Loop, radiation toward bottom of page.</p> <p>In this direction there is radiation only from the corners. (Image size <math>6\lambda</math>)</p>	<p>2.56E-02</p> 

<p>Square plate, edge normal to illumination.</p> <p>This is a <math>3\lambda</math> square PEC plate in the horizontal plane. (Actually modelled as a grid of wires at <math>\lambda/10</math> spacing). The image shows the radar cross section when illuminated with a plane wave from the right. The bright line shows where the wave E field is shorted out by the conducting plate. Also there is some radiation from the trailing corners. Note the number of spurious image points, even beyond the plate, due to the untapered 1 cycle per <math>\lambda</math> filter. (Image size <math>6\lambda</math>)</p>	<p><math>3.11E-04</math></p> 
<p>Square plate, illuminated diagonally.</p> <p>This shows the radar cross section when the same <math>3\lambda</math> square plate is illuminated by a plane wave arriving diagonally from the right. The main contribution to the radar echo comes from the outer corners. (Image size <math>6\lambda</math>)</p>	<p><math>7.48E-05</math></p> 

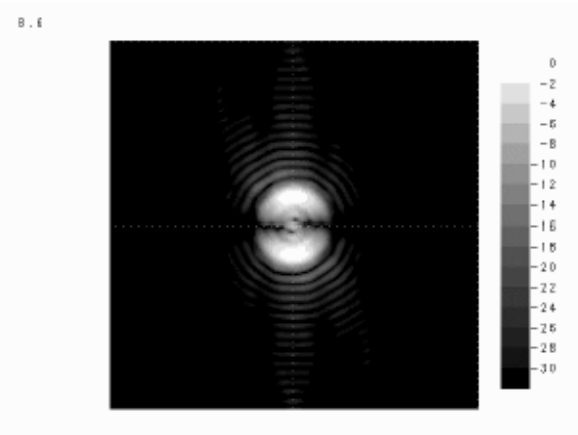
Archimedian spiral, Etheta polarisation

Because the image filtering process is separated from the radiation integral, it is possible to make near field images, as well as far field. This image is a near field image of an horizontal Archimedian spiral antenna viewed from above. This is a near field view of the image formed from the far field radiation. The spiral diameter overall is half a wavelength. Resolution  $0.1\lambda/\text{cycle}$ . The faint outer rings are filtering artefacts. (Image size  $2\lambda$ )



Archimedian spiral, Ephi polarisation

The same antenna, but Ephi. Together these two images show the circular polarised radiation coming from the spiral turns where the turn circumference equals one wavelength. (Image size  $2\lambda$ )



### **Radio Camera**

An alternative imaging process is to emulate a camera. In this process a plane is created in the far field of the antenna/scatterer, and the E field is calculated at many points on the plane (usually in a rectangular grid). This array of complex field values is a numerical hologram. A reference wave is not needed, as the phase is recorded in the complex E field value. This numerical hologram may be reconstructed using a camera lens, or equivalently by taking the FT of the 2D complex field values. The image is formed at one focal length behind the camera lens. The radiation integral has already removed the evanescent energy, so it is not necessary to filter the image any further. Note that the point spread function may be larger than the theoretical Airy disk, since the finite lens aperture (or grid size) can only worsen the resolution. In microscopy this reduction is known as the "numerical aperture". Using NEC for example, we can evaluate the far field over a rectangular grid of points on a plane normal to the look angle. The difference from the previous imaging process is that the plane is in the far field. The antenna/scatterer should be rotated (with a GM card) so that the desired look angle is moved to the x axis. The near field command (NE) is used to create a planar grid of field values in the YZ plane. There are still two polarisations required. After gathering the output values into a suitable matrix form, the FT image may be formed using Matlab or Mathematica etc.

### **Acknowledgement**

I wish to thank John Shaeffer and Edmund Miller for introducing the concept of imaging at their ACES

short course, and also for the many conversations since that helped further my understanding of the subject.

### **Conclusion**

Two practical radiator imaging techniques have been described. These are thought to be new, but similarities to near field measuring techniques and holography suggests that they have simply been rediscovered. However, it is timely to bring imaging to the attention of CEMists as a useful tool in understanding radiation. The author has used the first technique to examine currents induced in a support tower, which caused an unwanted null in the radiation pattern. Viewing the currents only confused the situation, since most of the currents did not radiate in the null direction.

### **References**

1. "Bistatic  $k$ -Space Imaging for Electromagnetic Prediction Codes for Scattering and Antennas", John F. Shaeffer, Kam W. Hom, Craig Baucke, Brett A. Cooper, and Noel A. Talcott, Jr. NASA Technical Paper 3569 (1996). <http://techreports.larc.nasa.gov/ltrs/PDF/NASA-96-tp3569.pdf>
2. High Resolution Radar Imaging, Dean L. Mensa, Artech House Inc., 1981. Describes a related technique to BSKS imaging.
3. "Introduction to Fourier Optics", by Joseph W. Goodman, McGraw Hill, 1968. Chapters 2 & 3.
4. "Numerical Electromagnetic Code (NEC) – Method of Moments", Naval Electronic Systems Command Technical Document 116, Part III Users Guide, GJ Burke and AJ Poggio, 1977.
5. Subroutine FFT, multivariate complex Fourier transform, computed in place using mixed-radix fast Fourier transform algorithm. R. C. Singleton, Stanford Research Institute, Sept. 1968.

# Reducing Electromagnetic Coupling in Shielded Enclosures using a Genetic Algorithm – Finite-Difference Time-Domain Solver

Russell Iain Macpherson<sup>1</sup> and Nick J Ryan<sup>2</sup>

Department of Engineering

King's College

University of Aberdeen

Aberdeen AB24 3UE

United Kingdom

r.macpherson@ieee.org<sup>1</sup>, n.j.ryan@eng.abdn.ac.uk<sup>2</sup>

**Abstract:** Comprehensive shielding in modern electronic equipment may lead to resonant behaviour within the equipment enclosure. This paper presents a method for optimising the placement of sources of electromagnetic (EM) energy and susceptors to this EM energy within an enclosed resonant cavity. The source and susceptor are placed on a dielectric slab within a perfectly conducting enclosure to reduce the level of EM coupling between the two. Optimisation is facilitated using a genetic algorithm coupled with a finite-difference time-domain solver. Results are presented for single objective optimisation and multi-objective optimisation cases.

## 1 Introduction

The explosive increase in the use of electronic equipment in the information age has led to electromagnetic compatibility (EMC) and electromagnetic interference (EMI) issues becoming more important to designers of electronic equipment. These issues must be considered at the time of design and not once designs are at the prototype stage. Higher clock speeds and faster switching transitions lead to greater levels of electromagnetic emissions, while higher component integration and lower power demands lead to greater sensitivity. So at once systems are becoming more prone to generating and also more sensitive towards EMI.

An area of interest to the authors is electronic enclosures and the placement of devices inside these enclosures. Modern electronic items have many different sources of EMI. These sources are often placed inside a rectangular shaped metal box to limit the EM emissions from the equipment. Care is taken to ensure the shielding is as comprehensive as possible thus apertures are kept to a minimum and covered in metallic blanking plates. Such a shielded, rectangular enclosure has a good chance of forming a resonant cavity so that field strengths generated by the circuit may well be enhanced once the circuit is mounted within the casing. Normally the circuit may have a number of sources within the enclosure, all of which add to the EM fields within; changing the positions of the various sources will change the amount of resonance and constructive interference, [1]. There are also likely to be a number of susceptors at multiple locations throughout the circuit.

There is obviously an optimal size and shape of enclosure and component layout however, exhaustively placing components inside enclosures and then computing the resultant fields is a task that that would require a massive undertaking on behalf of the designer. A far better approach to component placement is to use some kind of optimisation method to place the components to achieve a desired radiation level. This paper describes the novel use of a genetic algorithm (GA) and a finite-difference time-domain (FDTD) solver to optimise source and susceptor placement inside a perfectly conducting structure, building upon initial work completed in [2].

Genetic algorithms are briefly introduced in section 2 and then the Finite-Difference Time-Domain method is introduced in section 3. Section 4 describes the setup of the computer simulation and section 5 discusses the results of these simulations, finally section 6 presents conclusions from the work.

## 2 Genetic Algorithms

GAs are a stochastic search mechanism with their operation firmly rooted in natural selection and survival of the fittest, [3] and [4]. GAs have been shown to provide robust search and optimisation in complex spaces, [3] and [5]. They use simple operations on a population of individuals, which lead to an emergent evolution of an individual or individuals. Each individual in the population represents a potential solution to the given problem scenario and as such is evaluated. After an individual has been evaluated a figure of merit (FoM) is attributed to the individual. This FoM is a measure of how well the individual solves the problem. GAs can lead to the optimal solution to a problem, more often however, they are used to optimise a problem towards an improved solution facilitating a trade-off between excessive computational time and meaningful results. The GA process can be summarised graphically as shown in figure 1.

The GA methodology used in this work is the micro genetic algorithm ( $\mu$ GA). The  $\mu$ GA technique has been shown to reach the optimal area of multi-modal solution spaces earlier than conventional GA methods, with min-

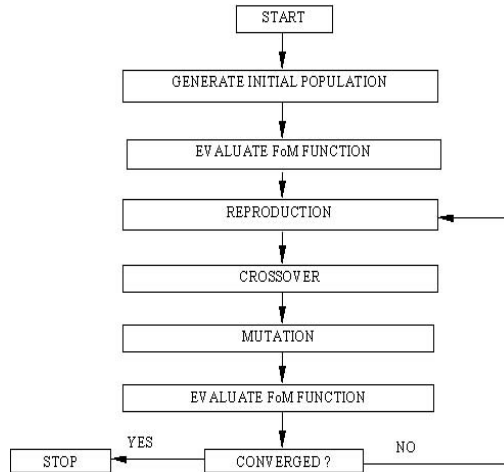


Figure 1: *GA Process Flowchart.*

imal computing time, [6]. It has already been demonstrated that the  $\mu$ GA can be successfully linked with an FDTD solver, [7], for optimisation in EM problems. Initially in a GA a fixed size population is created and populated with randomly generated individuals of a fixed length, this length is determined by the encoding of the problem parameters. The population size for the  $\mu$ GA is generally kept small *e.g.* five, this is different from the classic GA where the population size is typically much larger, in the order of 100s. These individuals are all possible solutions to the same given problem. They are assessed and each one given a score, the FoM, which is then used to determine the likelihood of reproduction into the next generation. The FoM is analogous to fitness in the natural world where fitter individuals survive longer and hence have a better chance of continuing their genetic lineage. The particularly successful, higher scoring individuals may be reproduced more than once into the next generation. In the  $\mu$ GA used here tournament selection is employed, this is perhaps the most effective for many application types as it has been shown to provide better convergence towards a solution in the initial stages of optimisation, [8]. Tournament selection works by randomly choosing  $N$  members of the population and in this instance as in many others  $N = 2$ . These individuals are then pitched against each other to determine which has the better FoM, the winner of the tournament being selected to be a member of the new population; this is repeated until the new population is filled. In conjunction with tournament selection elitist reproduction is also employed, this guarantees that the best individual from a population is present in the next population, hence preserving the best current solution to the given problem and maintaining a good genetic stock. After reproduction the individuals undergo crossover. Here two randomly picked individuals are mated together, swapping information between their chromosomes. In a classic GA mutation is also applied, however in the  $\mu$ GA mutation is turned off. Mutation serves to alter the genetic makeup of these new offspring with a small fixed probability. Once again mimicking nature, mutation can lead to either a detrimental or beneficial effect on performance. Mutation allows, in a classic GA, random search to take place and hopefully leads to the avoidance

of local optima. Once the population has converged to a determined optimal value then further GA operating is no longer needed and the GA can be halted. Due to the small population size used in the  $\mu$ GA premature convergence is often seen to be happening, to prevent this a restart mechanism is used. This restart mechanism involves checking for convergence in the current generation of individuals and then restarting the next generation with only the elite individual and new randomly created individuals. The use of a restart operator ensures random search takes place and leads  $\mu$ GA away from local optima. Convergence is checked for in this application by measuring the changes in the chromosomes, the individuals, between generations. Once there are few changes between generations then the population can be considered to be converged, the setting of this limit is a parameter that the user has control over. An important component of any GA code is the device by which random numbers are generated, or to be more correct pseudo-random numbers. This is usually a portable pseudo-random number generator (PRNG) that produces the same sequence of *random* numbers for a given seed value. The *quality* of the PRNG is an important factor. The area of PRNG research is vast and not going to be, for brevity, discussed here. Common references on the subject are [9], [10], [11] and [12].

A clear difference can be seen here between optimisation based on calculus methods and GA based optimisation. GAs make use of interim performance in the optimisation problem, calculus based methods are only concerned with optimisation toward an overall optimal point and do not “remember” any interim performances.

### 3 The FDTD Method

The FDTD method, [13], [14], has become one of the most popular methods for solving Maxwell’s equations. It is a volumetric domain decomposition technique that is second order accurate in space and time, easily implemented in software and accurately models the physical world. It is a widely used method for EMC/EMI work, [15], as well as radar, bioengineering and antenna analysis. The FDTD method is described widely in the literature, [16], and so only a very brief description is given here.

Maxwell’s equations, in differential form, equations (1) - (2), are simply modified to central-difference equations, discretised, and implemented in software. The equations are solved in a leap-frog manner, [14], *i.e.* the electric field is solved at a given instant in time, then the magnetic field is solved at the next instant in time, and the process is repeated over and over again. In equations (1) and (2)  $\mathbf{H}$  and  $\mathbf{E}$  have their usual meanings.

$$\frac{\partial \mathbf{H}}{\partial t} = - \left( \frac{1}{\mu} \nabla \times \mathbf{E} + \frac{\rho'}{\mu} \mathbf{H} \right), \quad (1)$$

$$\frac{\partial \mathbf{E}}{\partial t} = \frac{1}{\epsilon} \nabla \times \mathbf{H} - \frac{\sigma}{\epsilon} \mathbf{E}. \quad (2)$$

Using a three dimensional Cartesian co-ordinate system we can now write out the vector components of the curl operator. Given below is only one of these components, namely the  $x$  component of the  $\mathbf{H}$  field,



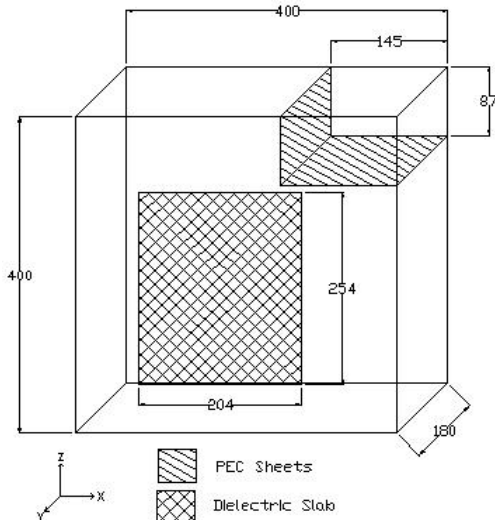


Figure 2: Enclosure geometry showing the representations of the internal structure and dielectric slab, all sizes are in millimetres, mm.

$$\frac{\partial H_x}{\partial t} = \frac{1}{\mu} \left( \frac{\partial E_y}{\partial z} - \frac{\partial E_z}{\partial y} - \rho' H_x \right), \quad (3)$$

where  $\mu$  is magnetic permeability and  $\rho'$  is a magnetic loss parameter. It is the complete set of coupled partial differential equations, six in total, that are the fundamental basis of the numerical FDTD algorithm. The discretised form of equation (3) is shown below:

$$\begin{aligned} m &= MEDIA_{H_x}|_{i,j,k}, \\ H_x|_{i,j,k}^{n+\frac{1}{2}} &= D_a(m) H_x|_{i,j,k}^{n-\frac{1}{2}} \\ &+ D_b(m) \begin{pmatrix} E_y|_{i,j,k+\frac{1}{2}}^n - E_y|_{i,j,k-\frac{1}{2}}^n \\ + E_z|_{i,j-\frac{1}{2},k}^n - E_z|_{i,j+\frac{1}{2},k}^n \end{pmatrix}, \end{aligned} \quad (4)$$

where  $n$  is the time step under consideration and  $i, j, k$  are the three orthogonal spatial co-ordinates. The integer array MEDIA defines material conditions for each field vector component. This allows the medium at each point to be mapped out. The arrays  $D_a, D_b$  are magnetic field update coefficients, there are corresponding electric field update coefficients also. A full explanation of all of these equations is presented in [13].

## 4 Simulation Setup

The initial results are obtained from using the GA to place a source and susceptor point relative to each other on the surface of a dielectric slab (DS) to achieve the lowest electromagnetic coupling between the two. The complete simulation is implemented in Fortran 77 compiled on a SUN ENTERPRISE server with 512MB of RAM utilising 4 of 8 processors.

### 4.1 Physical Problem Description

The problem geometry is that of a simplified metal box, which has perfectly electrically conducting (PEC) walls, an internal structure and DS representation. The internal structure is modelled as two PEC sheets in the top corner of the geometry. The DS can be thought of as a representation of the substrate of a printed circuit board (PCB). The problem geometry is shown in figure 2. The DS has a relative permittivity,  $\epsilon_r$ , of 4 and possesses unity magnetic permeability  $\mu_r$ .

### 4.2 $\mu$ GA and FDTD Setup

The  $\mu$ GA used is based on the implementation by Carroll, [17], modified to accommodate the given task of moving the source point and susceptor point on the DS. The two points are specified in a three dimensional Cartesian system with the  $y$  ordinate being held constant as this represents the surface of the DS. Binary encoding is used in the  $\mu$ GA and this leads to a chromosome string length of 24 bits, 4 bits per  $x, y$  and  $z$  co-ordinate of the source and susceptor. It should be noted that it would be possible to omit the  $y$  ordinate from the chromosome however the memory saving would be insignificant especially when compared to the coding effort required to convert the GA for this one specific case. Care must be taken to avoid the  $y$  ordinate being altered during reproduction and crossover, this is achieved using a uniform crossover operator. Uniform crossover, [18], has also been found to give faster convergence than single point crossover in a  $\mu$ GA, [6], [19]. The population size is maintained at five. These co-ordinate values are passed to the FDTD solver which computes the resulting field distribution inside the enclosure. The peak electric field at the susceptor point is returned as the FoM to the  $\mu$ GA, no fitness scaling is used as tournament selection is the method of selection employed in this GA implementation, [18]. The  $\mu$ GA attempts to minimise this FoM, *i.e.* minimise the peak electric field at the susceptor point.

The FDTD solver is based on the equations given in [13]. The DS is one cell thick and has one cell of free space between itself and the enclosure wall. The PEC sheets are modelled as infinitely thin. A soft  $E_z$  directed sinusoidal, continuous wave, ideal Hertzian dipole of  $2.05GHz$  frequency and amplitude of  $10Vm^{-1}$  is used as the source in the FDTD simulation. The domain is discretised into dimensions of  $7.2727mm$  in the  $x$  and  $z$  directions and  $7.2mm$  in the  $y$  direction. Based on these dimensions and the material within the computational domain the time step size for the solver is set at the Courant limit, in this instance approximately  $14ps$ .

Initially two optimisation cases are run; a non-lossy and then a lossy dielectric slab, in the lossy case the conductivity is set to  $0.04Sm^{-1}$ . After this a multi-objective simulation is run where two objectives are to be optimised, these being the reduction in coupling between source and susceptor points at two specific frequencies.

## 5 Results

### 5.1 Single Objective Optimisation

The progress of the optimisation process can be seen in figure 3 where the results of both the non-lossy and lossy simulations are presented. This figure shows the evolution of the best individual in the simulation, the elite individual. While this individual remains the best the FoM remains at the same value, when a superior one is bred, a step change occurs indicating the presence of a new elite value.

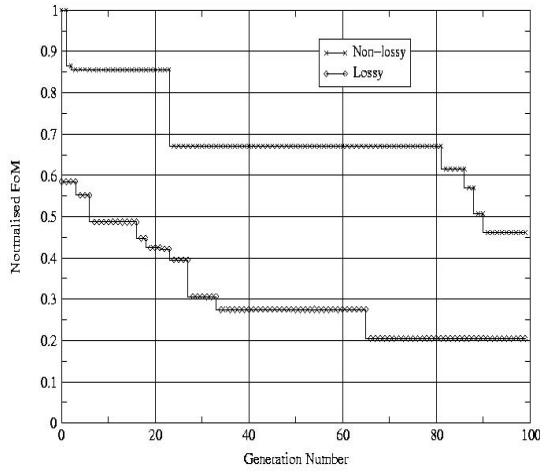


Figure 3: *Generation optimisation of both the non-lossy and lossy cases.*

The final value for the non-lossy case is  $0.0541Vm^{-1}$  from an initial value of  $0.1172Vm^{-1}$  and the final value for the lossy case is  $0.0240Vm^{-1}$  from a value of  $0.0685Vm^{-1}$ . Both of the curves are normalised to the value of  $0.1172Vm^{-1}$  for ease of comparison. As expected the values of field strength for the lossy case are lower than those for the non-lossy case as in the lossy case energy is dissipated in the dielectric slab. Figure 3 also shows us that the lossy case reaches its best FoM at generation 66, earlier than the non-lossy case which reaches its best FoM at generation 91. This is a random dynamic of the GA and attributable to the solution surface topology and the choice of PRNG used with the  $\mu$ GA. The number of generations was limited to 100 as experience with this code has shown that there is a minimal return on computing time by exceeding this point. Testimony to this is given by the fact that running the code to 200 generations gives only a final value of  $0.0507Vm^{-1}$  for the non-lossy case and  $0.0204Vm^{-1}$  for the lossy case, a marginal increase in performance for a doubling of computation time. This embraces one philosophy of using a GA, namely to produce an acceptable improvement toward an optimal point for a limited amount of effort.

The final field distribution on the surface of the DS can be seen in figure 4 for the non-lossy case and in figure 5 for the lossy case. These plots are generated by applying a peak hold to the  $E_z$  component at each location on the surface of the DS throughout the simulation.

The final positions of the source and susceptor points on

the DS are indicated; for the non-lossy case these are at (2,16) and (3,35) respectively, and for the lossy case the co-ordinates are (2,35) and (23,11). These co-ordinate values given are of course on the  $x$  and  $z$  axes as the  $y$  ordinate is constant. These false colour plots clearly show that the  $\mu$ GA has indeed found good solutions but not the best solutions, the global minimum point in figure 4 is at (2,2) with a value that is  $2.1dB$  down on the position found by the  $\mu$ GA. In figure 5 the global minimum is at (12,14) with a value that is  $1.4dB$  down the  $\mu$ GA position. The final values found by the  $\mu$ GA are  $57.6dB$  and  $64.6dB$  down on the global maximum for the non-lossy and lossy cases respectively. It should be noted that the patterns presented in these figures are ones of over 1 million possible patterns due to source and susceptor placement, finding the global minimum on each of them would require direct evaluation of each pattern, the  $\mu$ GA vastly cuts down on the number of evaluations required to arrive at an acceptable result.

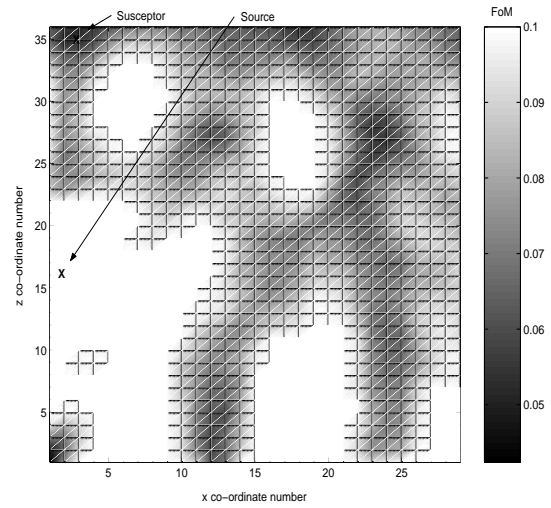


Figure 4: *False colour plot of final field distribution on surface of dielectric slab after non-lossy simulation. The  $x$  and  $z$  axes are marked in FDTD cells. Source and susceptor positions are indicated on the figure.*

### 5.2 Multi-objective Simulations

Multi-objective optimisation (MO) is often sought in practice as often compliance in one particular objective upsets the compliance of another objective. MO aims to achieve a solution that can not be improved upon, simultaneously, in each of the objectives. This is called a Pareto optimal solution and the set of all these solutions is called the Pareto optimal set, [20]. For the MO simulations some changes had to be made to the GA-FDTD code. As two objectives were being optimised a method of measuring their fitness at one and the same time is required, to accomplish this the method of objective weighting is used, [20]. This method is explained mathematically by equation (5),

$$Z = \sum_{i=1}^N w_i f_i(\mathbf{x}) \quad \text{where } \mathbf{x} \in \mathbf{X}. \quad (5)$$

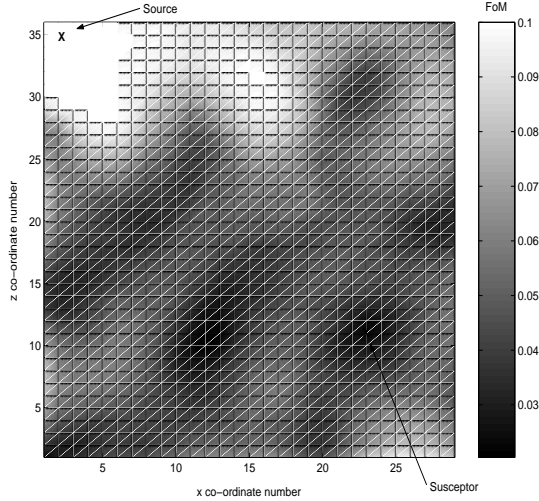


Figure 5: *False colour plot of final field distribution on surface of dielectric slab after lossy simulation. The x and z axes are marked in FDTD cells. Source and susceptor positions are indicated on the figure.*

In equation (5)  $Z$  is a scalar valued variable that is a weighted sum of the individual objectives, where there are  $N$  objectives in total. The function  $f$  is the function that returns the FoM, in this case the FDTD solver, and  $\mathbf{x}$  represents the parameters of the function, co-ordinate values in this case. The feasible region of solutions is denoted by  $\mathbf{X}$ . The sum of the individual weights adds to 1 and each weight lies in the range 0 to 1 *i.e.*  $0 \leq w_i \leq 1$ . It is the scalar value  $Z$  that is optimised by the GA. The method of objective weighting is an easily implementable scheme that produces a solution from the Pareto optimal set.

The problem setup for the MO optimisation involves the same geometry as previously with the only change being the source. A Gaussian pulse modulated onto a sine wave is now used as the source. This gives a symmetrical spectrum about the carrier frequency, no DC component, and a bandwidth controlled by the length of the pulse. Its mathematical form given in [13] is described by equation (6),

$$E_z = E_0 e^{-\left[\frac{n-n_0}{n_{decay}}\right]^2} \sin(2\pi f_0(n-n_0)\Delta t). \quad (6)$$

The Gaussian pulse is centred around frequency  $f_0$  at step  $n_0$  with a  $1/e$  characteristic decay of  $n_{decay}$  steps, and  $\Delta t$  is the step size. The time series and frequency response of the source is shown in figure 6. The centre frequency for the source is chosen at  $1.500GHz$  and the objectives for optimisation were chosen as the minimisation of the  $1.002GHz$  and  $2.004GHz$  components in the frequency response which is computed on the fly as the FDTD simulation progresses as detailed in [13]. These frequencies were chosen as they tie in with equipment used in a related measurement study. Only non-lossy simulations were run in this setup.

The resulting frequency response from the  $E_z$  component at the susceptor point the simulations can be seen in figure 7. The dashed line in figure 7 shows the initial DFT

before the optimisation process begins, the solid line in the figure displays the final DFT after completion of the optimisation process. A clear difference in the two curves at the respective objective frequencies can be seen. Also, it can be clearly seen that the field values at the objective frequencies, on the final DFT, are considerably lower than at other frequencies, within the same response, excepting of course at the tails of the response where there is minimal energy from the source. The values of the objectives on the final response are  $54dB$  down for the  $1.002GHz$  objective on the max value in the response and the value at  $2.004GHz$  is  $44dB$  down. Relative to the initial DFT the final response is down  $27dB$  at the  $1.002GHz$  objective and down  $35dB$  at the  $2.004GHz$  objective.

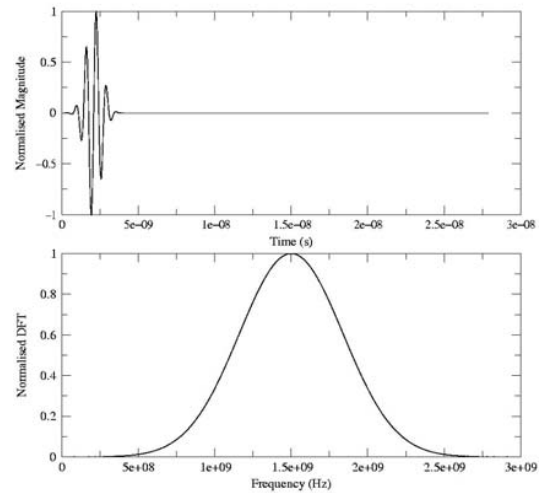


Figure 6: *Time series of the pulsed source, upper graph, and its DFT, lower graph. This is the source characteristic used in the multi-objective optimisation simulations.*

## 6 Conclusions

A method of using a  $\mu$ GA in conjunction with a FDTD solver to facilitate electromagnetic optimisation has been shown. The conjoining of the two codes allows a difficult design problem to be tackled, namely that of radiating and susceptible component placement within an arbitrary metallic structure to minimise coupling. The  $\mu$ GA technique is used as this gives a significant reduction in computation time with little loss in performance of the final optimised result. Ensuring that the  $\mu$ GA finds the global optimum in difficult optimisation problems is an area that needs further attention but the ability of the technique to reach a near optimal solution has been demonstrated. Both single and multiple objectives for optimisation have been presented with promising results from each. It is worth noting that if an exhaustive search were to be completed on the problems presented then over one million simulations would be required taking over one year to complete; the GA based search, however, took approximately four hours.

The design optimisation cases presented are rather simplistic but do prove the concept of the hybrid code. More

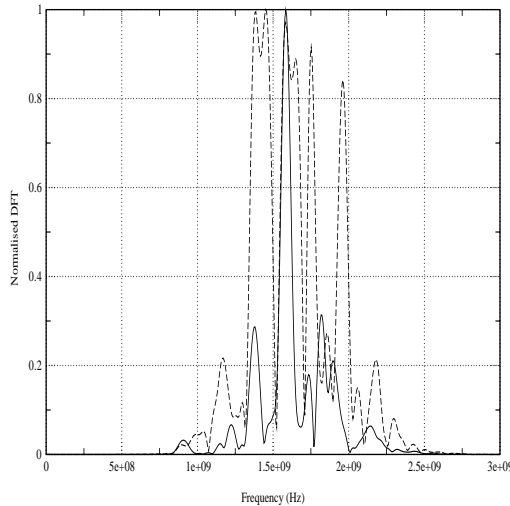


Figure 7: DFTs of  $E_z$  at the susceptor point of the multi-objective simulation with objective of minimising the 1.002GHz and 2.004GHz frequency components of the response. Shown are the initial DFT before optimisation begins (dashed line) and the final DFT after optimisation (solid line).

challenging problem geometries can easily be accommodated in the FDTD code with little burden to computing time as once the domain has been discretised it is the number of resulting cells that chiefly determines the computation time. It is envisaged that this tool can be used to provide design rules for component placement within an enclosed resonant cavity and that it can also be used to assess specific designs.

## References

- [1] J. Mix, G. Haussmann, M. Piket-May, and K. Thomas, "EMC/EMI design and analysis using FDTD," in *IEEE Int. EMC Symp.*, vol. 1, (Denver, CO), pp. 177–181, 1998.
- [2] R. I. Macpherson and N. J. Ryan, "The use of a genetic algorithm and the FDTD method for limiting resonance in shielded enclosures," in *Proceedings of EMC Europe 2000, Brugge, 4<sup>th</sup> European Symposium on Electromagnetic Compatibility*, vol. 2, pp. 203–208, September 2000.
- [3] D. Goldberg, *Genetic Algorithms in Search, Optimization and Machine Learning*. Reading, MA: Addison-Wesley, 1989.
- [4] R. L. Haupt and S. E. Haupt, *Practical Genetic Algorithms*. John Wiley & Sons, 1998.
- [5] J. Holland, *Adaption in Natural and Artificial Systems*. The University of Michigan Press, 1975.
- [6] K. Krishnakumar, "Micro-genetic algorithms for stationary and non-stationary function optimization," *SPIE: Intelligent Control and Adaptive Systems*, vol. 1196, pp. 289–296, 1989.

- [7] J. Jiang and G. P. Nordin, "A rigorous unidirectional method for designing finite aperture diffractive optical elements," *Optics Express*, vol. 7, no. 6, pp. 237–242, 2000.
- [8] G. J. E. Rawlins, ed., *Foundations of Genetic Algorithms*. Morgan Kaufmann, 1991.
- [9] D. E. Knuth, *The Art of Computer Programming*, vol. 2, Semi-numerical Algorithms. Reading, Massachusetts: Addison-Wesley, 2 ed., 1981.
- [10] P. Hallekalek, "Good random number generators are (not so) easy to find," *Mathematics and Computers in Simulation*, vol. 46, pp. 485–505, 1998.
- [11] P. L'Ecuyer, "Uniform random number generation," *Ann. Oper. Res.*, vol. 53, pp. 77–120, 1994.
- [12] P. L'Ecuyer, *Random Number Generation*. New York: In Handbook of Simulation, Jerry Banks (ed.) Wiley, 1997.
- [13] A. Taflov, *Computational Electrodynamics: The Finite-Difference Time-Domain Method*. Boston, MA: Artech House, 1995.
- [14] K. S. Yee, "Numerical solution of initial boundary value problems involving Maxwell's equations in isotropic media," *IEEE Transactions on Antennas and Propagation*, vol. 14, pp. 302–307, Mar. 1966.
- [15] B. Archambeault, O. M. Ramahi, and C. Brench, *EMI/EMC Computational Modeling Handbook*. Kluwer Academic Publishers, 1998.
- [16] J. B. Schneider and K. Shlager, "Finite-Difference Time-Domain literature database." WWW. Available at <http://www.fdt.org> Last Accessed 20<sup>th</sup> April 2002.
- [17] D. L. Carroll, "Fortran Genetic Algorithm driver." WWW. Available at <http://cuerospace.com/carroll/ga.html> Last Accessed 20<sup>th</sup> April 2002.
- [18] M. Mitchell, *An Introduction to Genetic Algorithms*. MIT Press, 5 ed., 1999.
- [19] D. L. Carroll, *Genetic Algorithms and Optimizing Chemical Oxygen-Iodine Lasers*, vol. XVIII of *Developments in Theoretical and Applied Mechanics*, pp. 411–424, H. Wilson, R. Batra, C. Bert, A. Davis, R. Schaper, D. Stewart, and F. Swinson eds. Gunterville, AL: The University of Alabama, 1996.
- [20] N. Srinivas and K. Deb, "Multiobjective optimization using nondominated sorting in genetic algorithms," *Evolutionary Computation*, vol. 2, no. 3, pp. 221–248, 1994.



Russell Macpherson graduated with a MEng (Hons) degree in electrical and electronic engineering degree from the University of Aberdeen, Scotland, U.K. in 1999. Currently he is pursuing his PhD studies at the same institution. His research interests include genetic algorithms, artificial neural networks and fuzzy logic and how these methods can be applied to electromagnetic optimisation problems.



Nick Ryan received the BEng degree in electrical and electronic engineering from the University of Bristol, U.K. in 1990 and the PhD degree from the department of electronic and electrical engineering, University of Sheffield, U.K. in 1998. He joined the department of engineering in the University of Aberdeen, U.K. in 1997 where he currently lectures safety and reliability in electronic systems. His research interests include computational electrodynamics, electromagnetic compatibility, and renewable energy systems.

## Impact of Some Discontinuities on the Convergence Of Numerical Methods in Electromagnetics.

Malcolm M. Bibby  
Gullwings, Weston, MA 02493  
e-mail: [mbibby@gullwings.com](mailto:mbibby@gullwings.com)

**Abstract.** The effect of discontinuities at edges and at feed-points of antennas on numerical convergence rates is investigated. In the case of edges, higher order representations of the edge-mode, expressed with the aid of Hermite splines, are shown to provide improved convergence in both global and local measures. When using a magnetic frill to excite an antenna, it is shown that when the current representation allows for the “charge jump” across the frill, then convergence is accelerated. The use of both sub-domain and entire-domain functions is explored.

### Introduction.

The treatment of edge conditions in electromagnetic problems is generally thought to be well understood, particularly after the publication by Meixner [1] of the relationship between ‘edge angle’ and the power of the distance from the discontinuity. An extensive review by Van Bladel [2] brought together much of the evidence in support of the phenomenon’s existence. Nevertheless, the model proposed by Meixner, while widely accepted, has not benefited from further development. More recently, Shen, et al., [3][4] reported on an analytical solution for the current and charge distributions at the ends of a tubular dipole. Their work showed that the Meixner method applied only at the very ends of such a dipole. While extending our knowledge in this area, their work is, nevertheless, restricted to current/charge distributions on a tubular dipole.

A different form of discontinuity arises at the feed-point of an antenna. This fact is less well recognized. The author knows of only one report that discusses it quantitatively. In this report, Popovic, Dragovic and Djordjevic [5, p38] pointed out that “as a consequence of the annular magnetic-current frill excitation, the current derivative has a discontinuity at the frill location”. They then went on to quantify the charge jump that occurs in this situation.

Unfortunately, it is not clear, from the balance of their writing, how they consistently incorporated this observation into their work in a general manner.

Recently, the author published reports [6][7] that examined the use of higher order basis functions in modeling a tubular dipole antenna/scatterer. The results presented in these reports did not support the expectation that higher-order basis functions would provide faster convergence properties. The models used in these investigations employed splines up to fifth order. They also incorporated the Meixner edge condition. Subsequent analysis has shown that the application of the simple form of the edge condition actually inhibited the convergence properties of the higher order models. The simple form of the Meixner edge condition has only one degree of freedom - it’s amplitude. In order for the splines covering the rest of the antenna/scatterer to meet their potential, the number of degrees of freedom in the edge model were increased (in this study) to match those of the adjacent spline.

As part of the analysis referred to in the preceding paragraph an appreciation for the problem associated with the charge jump across the magnetic frill developed. The problem exhibits itself through a slow convergence and/or oscillation in the input admittance of the antenna as the model size is increased. The slow convergence problem was found to occur for both entire-domain and sub-domain basis functions.

### The Basis Functions.

The sub-domain basis functions used on the main portion of the antenna/scatterer are all splines and are shown in Table I. They are the same as those used in [6][7]. They include the linear spline, which acts as a reference for the performance of the higher-order functions. As the results when using the 3-term-sin/cos

Expansion Function	Mathematical Description
<b>3-term sin/cos</b>	$I(y) = A_i + B_i \sin(k(y - y_i)) + C_i(\cos(k(y - y_i)) - 1)$ where $y_i \leq y \leq y_{i+1}$
<b>Linear Spline</b>	$I(y) = a_i + b_i(y - y_i) \quad y_i \leq y \leq y_{i+1}$
<b>Quadratic Spline</b>	$I(y) = a_i + b_i(y - y_i) + c_i(y - y_i)^2 \quad y_i \leq y \leq y_{i+1}$
<b>Cubic Spline</b>	$I(y) = a_i + b_i(y - y_i) + c_i(y - y_i)^2 + d_i(y - y_i)^3$ where $y_i \leq y \leq y_{i+1}$
<b>Quartic Spline</b>	$I(y) = a_i + b_i(y - y_i) + c_i(y - y_i)^2 + d_i(y - y_i)^3 + e_i(y - y_i)^4$ where $y_i \leq y \leq y_{i+1}$

Table I. Definitions of the splines considered in this study.

$$a_{N+1} = \sum_{i=1}^N c_i \Delta_i^2 + 2 \sum_{i=1}^{N-1} c_i \Delta_i \sum_{j=i+1}^N \Delta_j + b_1 \sum_{i=1}^N \Delta_i + a_1 \quad (1a) \quad b_{N+1} = 2 \sum_{i=1}^N c_i \Delta_i + b_1 \quad (1b)$$

functions were almost identical to those found when using the quadratic spline, only the latter are reported. The reader should be aware however that the 3-term-sin/cos functions were studied. When using splines such as those found in Table I, one asserts as much continuity at the junction of contiguous cells as the functions allow. For example, a quadratic spline, which is of order 3 and degree  $p = 2$ , provides  $C^1$  continuity. Hence, in the case of a quadratic spline both the amplitude and the first derivative can be matched. By this means the number of variables is reduced. In the case of the quadratic spline, for  $N$  cells, one needs to determine only the free variables

$$a_1, b_1, \sum_{i=1}^N c_i, b_{N+1}, a_{N+1}.$$

The amplitude and first derivative at one extremity are related to those at the other extremity through the relationships given in equations (1a) and (1b) above.

The sub-domain edge/end basis functions used in this study are based on the form given in [2, p120]:

$$E_z = d^v (a_0 + a_1 d + a_2 d^2 + a_3 d^3 + \dots) \quad (2)$$

where  $E_z$  is the electric field normal to the edge/end,  $d$  is the distance from the edge/end,  $v$  is a number greater than  $-1.0$  and the series  $a_0, a_1, a_2, a_3, \dots$  are constants to be determined. Expression (2) needs to be matched up, at its cell boundary, with each of the functions shown in Table I. Thus derivatives of this function are required. Straightforward differentiation of the

function can be performed no more than once while still maintaining a function that can be integrated, and thus might be employed with the quadratic spline. However, it would fail for higher order splines. An alternative, and numerically superior, method is to apply the concepts found in the development of Hermite splines.

Hermite splines are different from most splines found in computational electromagnetic studies which are concerned only with amplitudes. The splines in Table I are examples of this latter situation. The constants at the open ends of these splines are the source of much writing on ways to handle them. – see, for example, [8]. The derivatives of these splines are functions of these constants. In the development of Hermite splines the issue of derivatives is tackled directly. Hermite splines are typically of odd degree, including  $p = 1$ , and are defined in terms of their amplitude and  $(p - 1)/2$  derivatives at each end. The process for developing Hermite cubic splines is covered in [9] and the more general case, with applications to CEM, is described in [10]. In the case of equation (2) only one end is open and the development for a two term expression will be described next. Two terms will provide amplitude,  $f(1)$ , and derivative,  $f'(1)$ , information that can be used directly with the quadratic spline described earlier.

Equation (2) is restated as

$$P(u) = f(1)H_1(u) + f'(1)H_2(u), \quad u = \left( \frac{h - z'}{\Delta} \right),$$

$(h - \Delta) \leq z' \leq h$ ,  $\Delta$  is the width of the cell and  $h$  is identified with a cell boundary.  $H_1(u)$  is a polynomial of order 2 selected so that  $H_1(1) = 1$  and  $H_1'(u) = 0$ . Similarly,  $H_2(u)$  is a similar polynomial selected so that  $H_2(1) = 0$  and  $H_2'(1) = 1$ . When these conditions are applied, the solution is given by:

$$P(u) = u^v((1 + v) - vu)f(1) + u^v(1 - u)\Delta f'(1) \tag{3}$$

This provides us with what we are looking for – a function that separates the amplitude and the first derivative at the open end and one that can be integrated in a straightforward manner. This concept can be extended to functions of higher orders, and is done in this study for use with the cubic and quartic splines of Table I.

When investigating the discontinuity at a magnetic frill, a structure that possesses no other discontinuities is useful for investigative purposes. A circular loop is such a structure and is examined here. The ‘natural’ basis functions to use in this situation are Fourier series. Due to symmetry, only cosine terms are typically used. The expansion series is then:

$$I = \sum_{i=0}^N a_i \cos(i\phi) \quad 0 \leq \phi \leq 2\pi \tag{4a}$$

This expansion has been in use for decades and the results of its use are well documented [11]. When one examines the reported results, the lack of finality in the convergence of the admittance at the feed-point is notable. Zhou and Smith [12] attributed this poor convergence to the use of a delta-function source. Their results using a magnetic frill source demonstrated that indeed the frill source performed better than the delta-function source. However the admittance curves still did not fully converge until  $N$  in (4a) was extremely large. This is surprising given the ‘natural’ suitability of

the functions in (4a). The work reported here shows that the model in (4a) is deficient for use when dealing with the magnetic frill as it does not account for the ‘charge jump’ across the frill. The derivatives of (4a) are all continuous, and what is needed is a set of functions that allows for this ‘charge jump’. Instead of discarding (4a), one can modify it as in (4b) below.

$$I = a_0 + \sum_{i=1}^N (a_i \cos(i\phi) + b_i \sin((2i - 1)|\phi|/2)) \tag{4b}$$

The derivatives of this series are such that a ‘charge jump’ can be modeled properly. As discussed in [10], in the immediate vicinity of the frill it is the odd derivatives of the current that must be in anti-phase on opposite sides of the frill.

**Solution Tools**

The equations used in the analysis that follows are based on the Electric Field Integral Equation, EFIE, formulation. In particular, in the case of the linear dipole, the equation is Hallen’s derivation [13], shown in (5) below. In (5)  $I$  is the desired current,  $G$  is the Green’s function,

$$R = \sqrt{(z - z')^2 + (2a \sin(\frac{\phi'}{2}))^2}, \text{ the radius is } a, C$$

is a constant to be determined and  $E_i$  is the incident excitation. The dipole, which is an open circular cylinder with an infinitesimally thin wall thickness, is located with its center at the origin of a cylindrical coordinate system with its length aligned with the  $z$  axis.

When investigating the loop, the derivation due to Mei [14], specialized for a loop is used – see (6) below. The center of the loop is located at the origin of a cylindrical coordinate system, with  $s = R_b\phi$ . The loop itself lies in the  $\rho, \phi$  plane with its feed-point at  $\phi = 0$ . In this case, the expression for  $R$  in  $G$  is  $R = a^2 + 2R_b^2(1 - \cos\phi') + 2aR_b(1 - \cos\phi')\cos\theta'$ , where  $\theta'$  is a local variable around the circular cross-section of the loop element. Here the

$$\int_{-h}^{+h} I(z')G(z, z')dz' + C \cos(kz) = \frac{1}{j\eta} \int_0^z E_i(z') \sin(k(z - z'))dz' \tag{5}$$

$$\int_{c's'} \int J(s') \left[ G(s, s') - k \int_0^s \sin k(s - \xi)G(\xi, s')(1 - \hat{\xi} \cdot \hat{s}')d\xi \right] ds' + C \cos ks = \frac{1}{j\eta} \int_0^s (\bar{E}_i \cdot \hat{\xi}) \sin k(s - \xi)d\xi \tag{6}$$

where  $G(z, z') = \frac{1}{4\pi} \int_{\phi=0}^{2\pi} \frac{e^{-jkR}}{R} d\phi'$



Extended Boundary Condition is used and the net electric field on the axis of the loop is zero. The numerical solutions for  $I$  in equations (5) and (6), which are expressed in the usual  $ZI = V$  system, are obtained with the aid of the Boundary Residual Method, BRM, [15][16]. This is a Least Squares Method variant that has two important elements. The first significant element is that the entries in the  $Z$  and  $V$  matrices are calculated as they would be for a point-matching method. However the location of the matching points is not arbitrary. Specifically they are located at the nodes of an appropriate integration rule such as Gauss-Legendre. Furthermore, the number of sample points exceeds the number of free variables, typically by a ratio of 2:1 or higher. This means the  $Z$  matrix is rectangular and the matrix equations are solved using QR or SVD methods [17]. The second important element is that the rows in the  $Z$  and  $V$  matrices are weighted by the weights from the same integration rule used to establish the nodes mentioned earlier. This has the important result of minimizing the residuals integrated over the entire surface being studied. Formally, this statement is  $\min \rho_{LS}^2 = \|ZI - V\|_2^2$ . This is an important measure. It reports on the performance of the solution over the complete surface and hence it is referred to here as a global measure. For comparative purposes, it is best to normalize this function. The normalized residual is:

$$\rho_{norm}^2 = \frac{\|ZI - V\|_2^2}{\|V\|_2^2} \quad (7)$$

### The Dipole as a Scatterer.

In order to calculate the currents on a straight dipole excited by a plane wave equation (5) is evaluated in conjunction with the basis functions shown in Table I. The boundary condition,  $I(\pm h) = 0$ , is satisfied in one of three ways. In the first method  $a_1$  and  $a_{N+1}$  are set to zero. In the second approach, the two end cells support the basic/conventional end function  $I(z') = a_0 \sqrt{(h - |z'|)/\Delta}$  and then enforce  $a_0 = a_1 = a_{N+1}$ . The derivatives,  $b_1$  and  $b_{N+1}$  and higher, are left unconstrained. In the third approach, the special Hermite end splines defined earlier are used and all applicable constraints are enforced. In the case of the linear spline, the second and third approaches

utilize the same function. For the quadratic case, a two term end spline is used, for the cubic case a three term end spline is used and the quartic spline employs a four term end spline. The plane wave is polarized parallel to the axis of the dipole and is normally incident.

Figure 1a shows the results for the current at the center of a half-wave dipole, with a radius of  $0.007\lambda$ . As the order of the spline is increased the results without the inclusion of any special end sections show only a small benefit from the inclusion of higher order terms. The inclusion of the conventional end spline provides an improvement, particularly for the lower order splines. Interestingly, the convergence curves for all four splines look very similar. It is only when the Hermite type end splines are added that the real benefit of using high order splines is observed.

Figure 1b reports the results for the Normalized Residual. It is observed that the conventional end function improves the performance of the lower order basis functions. However, the performance of the Hermite end functions is consistently better.

### The Loop Antenna.

As mentioned above, the circular loop is used to investigate the discontinuity associated with a magnetic frill. The basis functions defined in equations (4a) and (4b) are used in conjunction with equation (6) to evaluate the currents at the feed-point of the antenna. When using equation (4b) the value of  $N$  is only half that of the corresponding value used with equation (4a). The circumference of the loop is one wavelength and  $\Omega = 2 \ln(2\pi R_b / a) = 10.0$ , where  $R_b$  is the radius of the loop and  $a$  is the radius of the loop element.

The convergence curves for the central current are shown in Figure 2a and the associated normalized residuals are shown in Figure 2b. The results show clearly the superiority of a series that accommodates the 'charge jump' at the feed-point, thereby confirming the presence of the phenomenon. Only 32 terms are considered in these graphs. If the number of terms were increased substantially, the results for the cosine series only would eventually converge to those observed with the use of the supplemented basis functions.

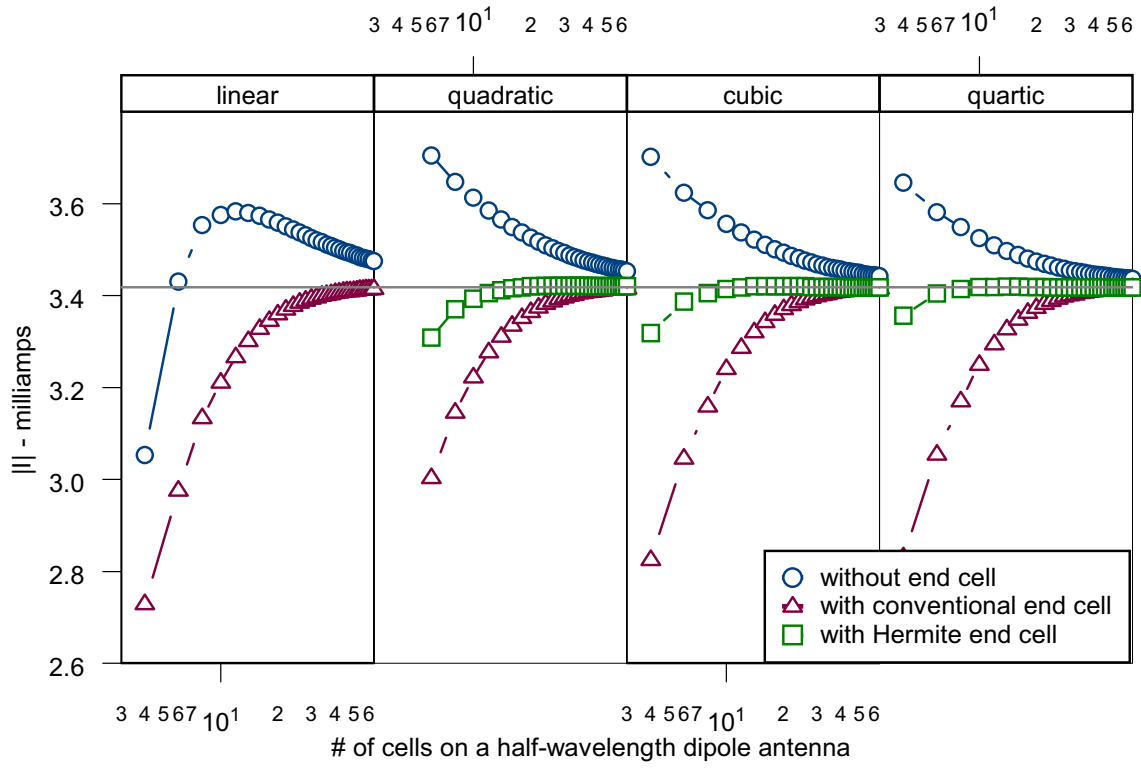


Figure 1a. Plots of the current on a dipole excited by a plane wave modeled with four splines

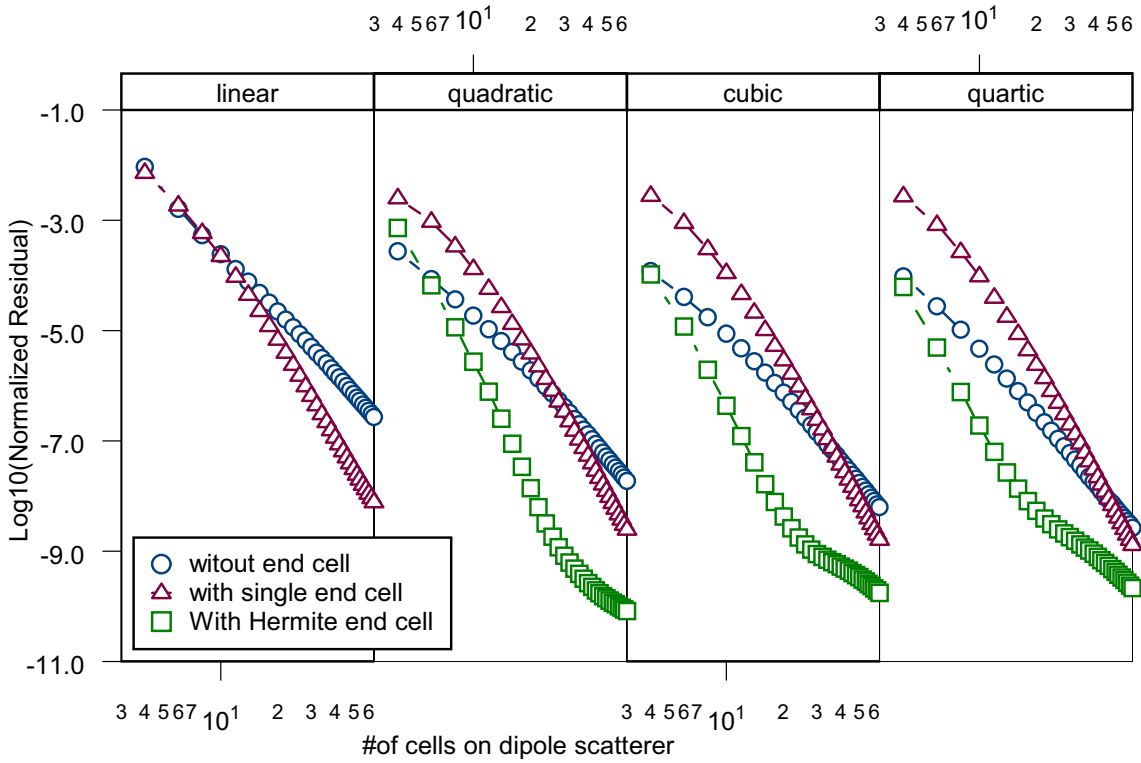


Figure 1b. Plots of the normalized residual on a half-wave dipole excited by a plane wave.

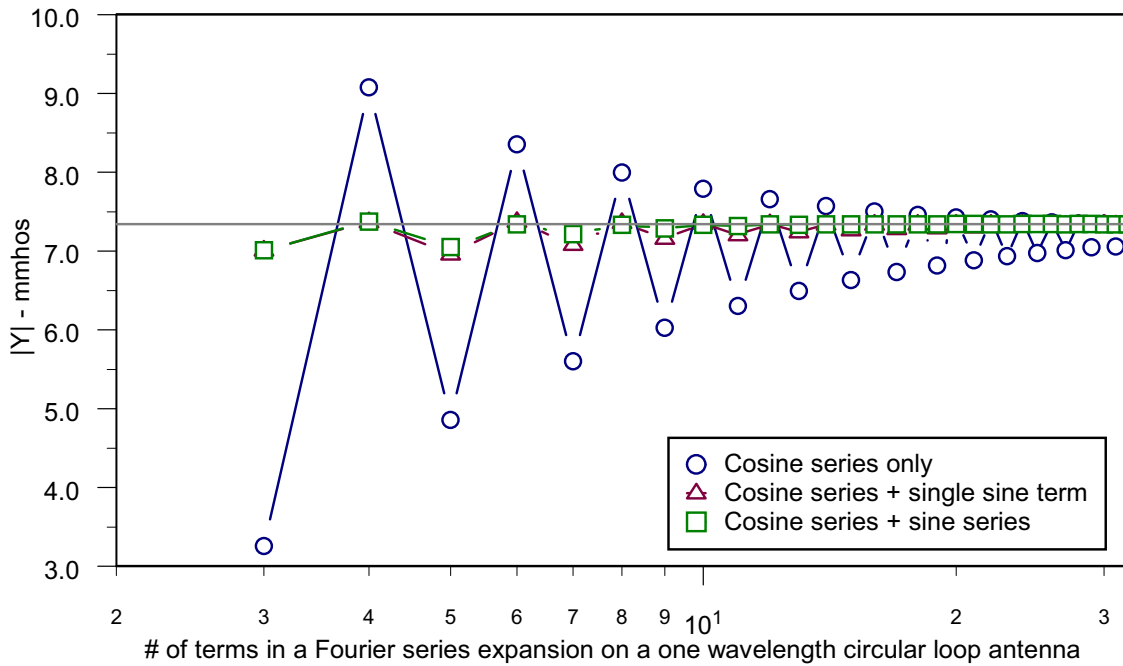


Figure 2a. Plots of the input admittance of a circular loop excited by a magnetic frill.

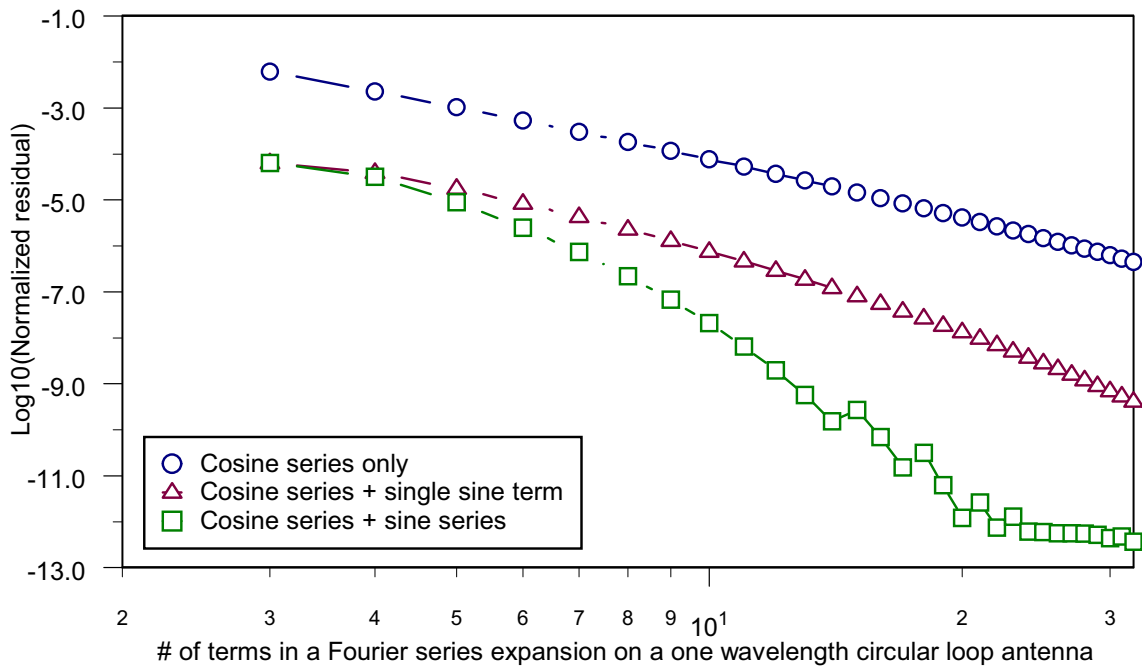


Figure 2b. Plots of the normalized residual for a circular loop excited by a magnetic frill.

$$I = a_0 + \sum_{i=1}^N a_i \cos(i\pi z'/h) \sqrt{h - |z'|} \quad (8a)$$

$$I = a_0 + \sum_{i=1}^N (a_i \cos(i\pi z'/2h) + b_i \sin((2i - 1)\pi |z'|/2h)) \sqrt{h - |z'|} \quad (8b)$$

### The Dipole as an Antenna.

The dipole antenna incorporates both of the types of discontinuity already discussed. Here, it has radius,  $a$ , of  $0.007\lambda$ . The frill has dimension of  $b/a=2.3$  where  $b$  is the outer radius of the frill. The combination of these two discontinuities is explored initially using sub-domain functions. The sub-domain functions are the same as those used earlier with a dipole scatterer. However, at the center of the dipole, the phase in the terms representing the first and third derivatives is shifted  $180^\circ$  when these derivatives exist. The impact on the convergence of the current at the feed-point can be seen in the results reported in Figure 3a. The results for the associated normalized residuals are shown in Figure 3b. It is clear, from both sets of data, that the phase reversal of the odd order derivatives at the frill contributes significantly to an improved model for the current.

Entire-domain functions have long been used to model the current on a linear dipole antenna. A study that compared ten such functions was published recently [18]. That study concluded that entire-domain functions performed poorly on the linear dipole. Historically, however, the choice for an entire-domain function on a linear dipole has been one of various forms of a Fourier series. In the absence of a better alternative, such a series is used here. The particular form of the Fourier series used is shown in (8a) above. In order to accommodate the "charge jump" at the magnetic frill, a modified form of the latter was investigated – this is shown in (8b) above.

The results, for the input admittance of a half-wavelength antenna, using these two series are shown in Figure 4a. The corresponding findings for the normalized residuals are shown in Figure 4b. When using equation (8b) the value of  $N$  is only half that of the corresponding value used with equation (8a). Both figures clearly demonstrate the utility of incorporating terms that address the issue of discontinuity across the frill.

### Discussion.

*End Effects.* When considering the results reported in Figure 1a, one must bear in mind that, for the linear spline, the conventional end term and the Hermite end term are one and the same. Adding a single end term to any of the splines produces an observable improvement in the convergence of the current at the center of the dipole compared with not using one at all. This is particularly true for the lower order splines. As mentioned earlier, the convergence curves obtained when using a single conventional end term all appear to have the same convergence characteristics. This suggests that the end term is limiting the convergence process. When the higher order end terms are included, to the maximum order possible, the convergence process is speeded up significantly. When viewed from a global perspective, as reported in Figure 1b, the conventional end term is important in the case of the linear spline. For the higher order splines the benefits become less as the order of the spline is increased. However, when the higher order end terms are included, the global results are distinctly better for all splines.

*Magnetic Frill.* The importance of properly incorporating "charge jump" properties into models of current flowing on an antenna excited by a magnetic frill is dramatically illustrated in Figures 2-4. The significant oscillations seen when employing a Fourier series containing only cosine terms is an indication of its lack of suitability – for both the loop and the linear dipole! To be sure that the oscillations were the result of the feed mechanism and nothing else, the excitation was changed from the magnetic frill to a plane wave. The oscillations disappeared in the case of the loop and were highly attenuated on the linear dipole. This allowed the conclusion that the oscillations are indeed a result of using the magnetic frill excitation and not something else. The addition of the sine terms in the current model, while improving the convergence results significantly, does raise the condition number of the impedance matrix from the region of  $\sim 10^4$  up to

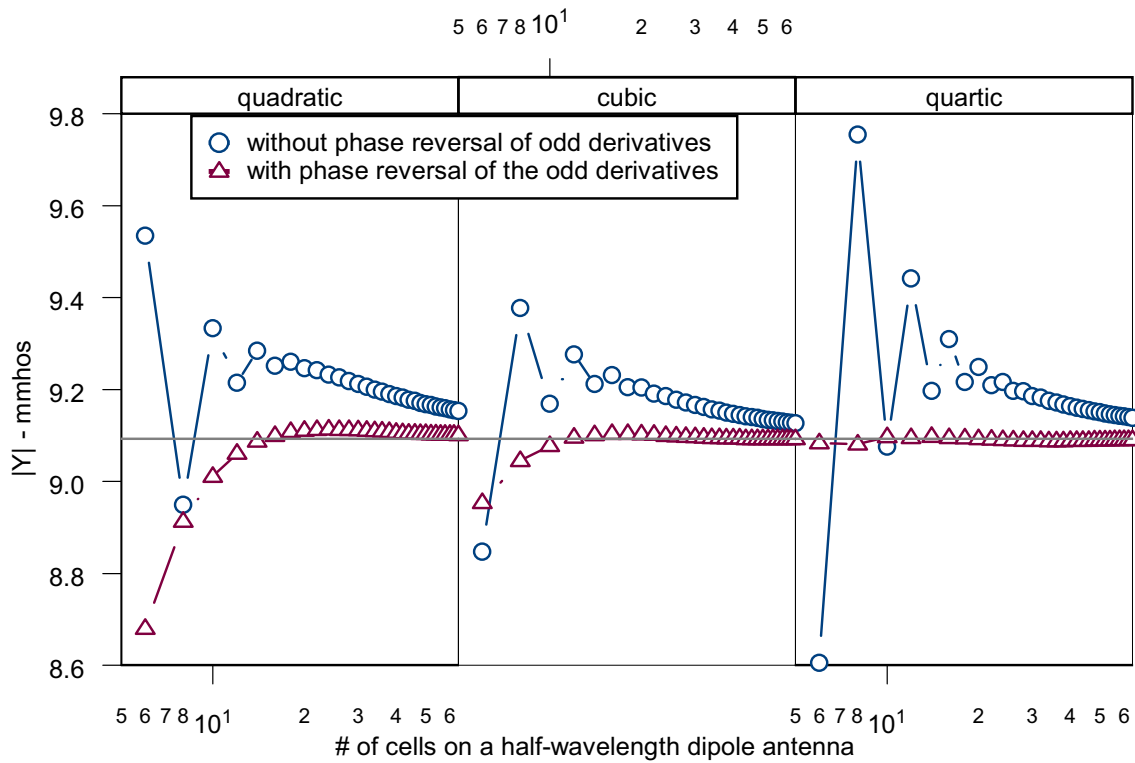


Figure 3a. Plots of admittance on a dipole excited by a magnetic frill for three splines.

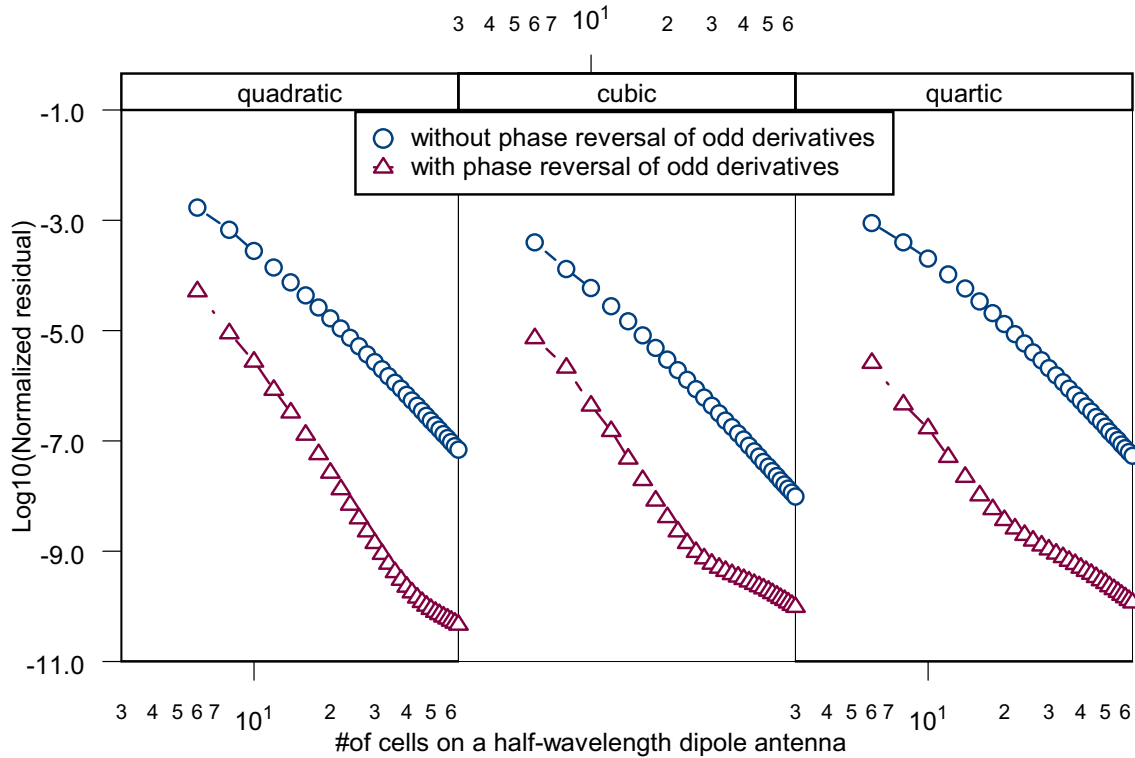


Figure 3b. Plots of the normalized residual on a dipole with magnetic frill for three different splines.

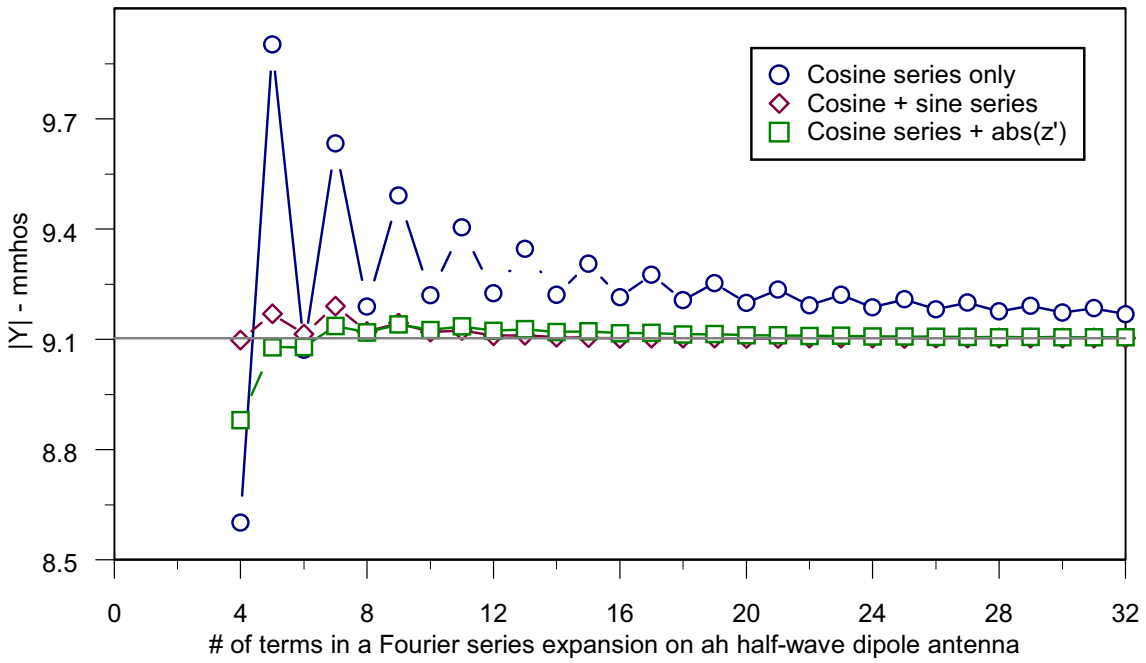


Figure 4a. Plots of the admittance of a half-wave dipole excited by a magnetic frill

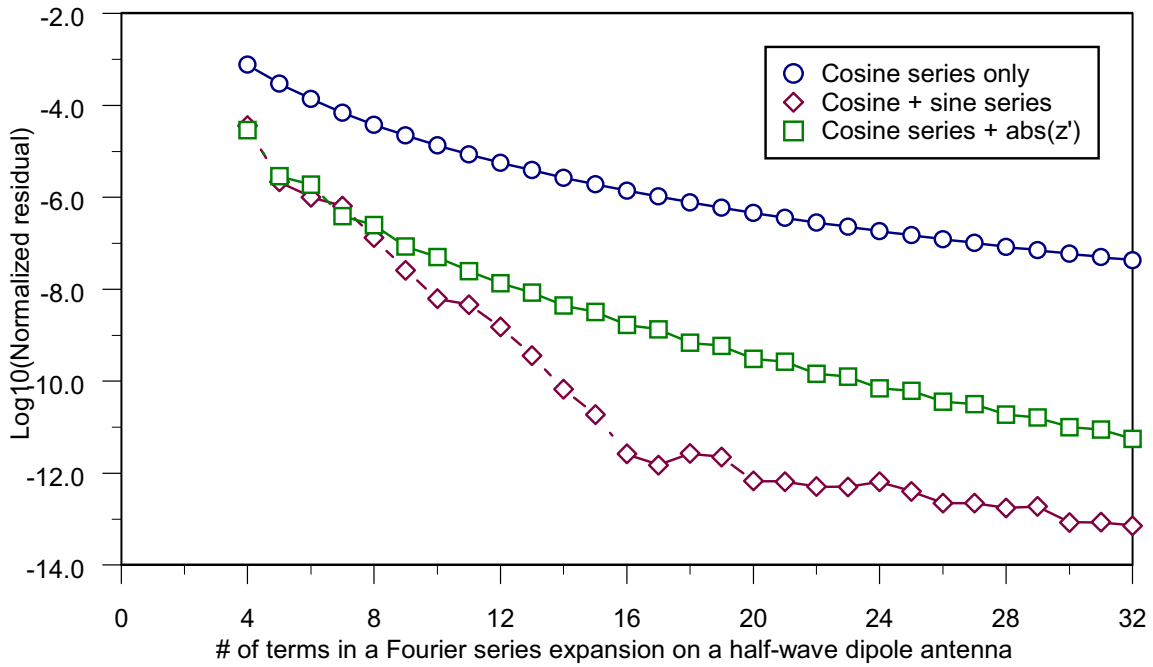


Figure 4b. Plots of the normalized residual on a half-wave dipole excited by a magnetic frill

$\sim 10^{10}$  when more than 12 terms are used in the series.

The linear dipole problem was also solved using a Method-of-Moments solution, using the standard Pocklington equation. This was done as a check on the testing method and the integral equation formulation. The testing functions were pulses of equal dimensions, the basis functions were again the Fourier series of (8a) and (8b) and the Pocklington equation was regularized per the procedure described in [19]. The results of using (8b) converged significantly faster than when using (8a) while the oscillations noted in connection with Figure 4 were almost completely attenuated. These findings provided further confirmation of the need to accommodate the discontinuity at the feed-point.

The presence of a high condition number in the entire domain solutions that include a series expansion of the absolute value of sine terms makes them unattractive. Consequently, the effect of incorporating a single term only was investigated. In the case of the loop this term was  $\sin(|\phi'|/2)$ . In the case of the dipole it was simply  $|z'|$ . The associated results are shown in Figures 2 and 4 respectively. Use of just these single terms contributes significantly to alleviating the convergence problem. The condition numbers were comparable to those observed when using the cosine terms only. This suggests that one judiciously selected term could significantly speed up the convergence rate in these situations. However, the ones tested here are not those functions – otherwise they would exhibit normalized residual curves at least as steep as those shown by the addition of the sine series.

The basic EFIE for a loop is shown in equation (9a). After some manipulation, this assumes the form shown in (9b). When the current is represented by (4a) the form in (9c) results. The last term on the right-hand side of this latter

equation evaluates to zero. But this is the term that represents the “charge jump”. Therefore the representation of (4a) is inadequate. A term, or terms, that permit(s) the current derivative at the origin to be discontinuous is necessary. The inadequacy of the representations of (4a) and (8a), is believed to be the main source of the oscillations seen in the relevant convergence curves.

In 1980, Richmond [20] reported that the incorporation of a term that represented an outgoing wave on an infinite dipole improved convergence considerably on a finite dipole. This was confirmed in [18], where it was also noted that the condition numbers were high. This outgoing term is essentially a log term at the feed-point and consequently presents a discontinuity there. It is possible that this discontinuity had more to do with the improvement realized by Richmond than the form of the term itself.

## Conclusions.

This study was motivated by the apparent failure of high-order basis functions to improve convergence rates when compared with basis functions of lower order [6][7]. As a result of this work, it is believed that the reasons for this failure originate with inadequate current modeling in the vicinity of discontinuities. Specifically, it has been demonstrated that to achieve superior convergence properties one must bear in mind three things.

1. Current models in the vicinity of discontinuities must support the same level of continuity as that supported by the models employed away from the discontinuities.
2. When an isolated excitation source, such as a magnetic frill, is part of the system, the current model(s) must have sufficient flexibility to accommodate issues such as “charge jump” in the excitation region.
3. The above comments apply to both sub-domain and entire-domain models.

$$\frac{E_i(\phi)}{j\omega\mu} = \int_{-\pi}^{\pi} \cos(\phi - \phi') I(\phi') G(\phi, \phi') R d\phi' + \frac{1}{k^2 R^2} \int_{-\pi}^{\pi} \frac{dI}{d\phi'} \frac{dG}{d\phi} R d\phi' \quad (9a)$$

$$\frac{k^2 R}{j\omega\mu} E_i(\phi) = \left[ \left[ \int_{-\pi}^{0^-} + \int_{0^+}^{\pi} \right] \right] \left( \cos(\phi - \phi') k^2 R^2 I(\phi') + \frac{d^2 I}{d\phi'^2} \right) G d\phi' + \frac{dI}{d\phi'} G \Big|_{0^-}^{0^+} \quad (9b)$$

$$\frac{kR}{j\eta} E_i(\phi) = \left[ \left[ \int_{-\pi}^{0^-} + \int_{0^+}^{\pi} \right] \right] \left( \cos(\phi') k^2 R^2 a_0 + \sum_{j=1}^N (\cos(\phi') k^2 R^2 - j^2) a_j \cos(j\phi') \right) G d\phi' + \sum_{j=1}^N -j a_j \sin(j\phi') G \Big|_{0^-}^{0^+} \quad (9c)$$

### Acknowledgements.

The author thanks Professor Andrew Peterson of the Georgia Institute of Technology for his encouragement and useful suggestions in connection with the preparation of this paper.

### References.

- [1] L. Meixner, "The Behavior of Electromagnetic Fields at Edges", *IEEE Trans. on Ant. & Prop.*, Vol. 20, No. 4, pp.442-446, 1972.
- [2] J. Van Bladel, *Singular Electromagnetic Fields and Sources*, Chapter 4, Clarendon Press, 1991.
- [3] H. Shen and T. T. Wu, "The Universal Current Distribution Near the End of a Tubular Antenna", *J. Math. Phys.*, 30(11), Nov., 1989.
- [4] H. Shen, R. W. P. King and T. T. Wu, "The Combination of the Universal End-Current and the Three-Term Current on a Tubular Dipole", *J. of Electromagnetic Waves and Applications*, Vol. 4, No. 5, 189-200, 1990.
- [5] B. D. Popovic, M. B. Dragovic and A. R. Djordjevic, *Analysis and Synthesis of Wire Antennas*, Research Studies Press, 1982.
- [6] M. M. Bibby, "A Comparative Study of Expansion Functions Using the Boundary Residual Method on a Linear Dipole – Part II: Sub-Domain Functions", *Journal of the Applied Computational Electromagnetic Society*, Vol. 17, No. 1, pp. 54-62, March 2002.
- [7] M. M. Bibby, "An adaptive Approach to Faster Convergence in the Solution of Electromagnetic Problems by Using non-Uniform Cell Sizes", *Proc. 18<sup>th</sup>. Annual Review of Progress in Applied Computational Electromagnetics*, pp. 457-463, Monterey, CA., March, 2002.
- [8] C. F. Gerald, *Applied Numerical Analysis*, 2<sup>nd</sup>. Ed., pp. 477-482, Addison-Wesley Publishing Co., 1978.
- [9] J. F. Epperson, *An Introduction to Numerical Methods and Analysis*, pp. 171-181, John Wiley & Sons, 2002.
- [10] M. M. Bibby, "Hermite Splines and Their Application in Electromagnetic Problems", in preparation.
- [11] R. W. P. King, & G. S. Smith, *Antennas in Matter*, pp. 529-537, The MIT Press, 1981.
- [12] G. Zhou & G. S. Smith, "An Accurate Theoretical Model for the Thin-Wire Circular Half-Loop Antenna", *IEEE Trans. on Ant. & Prop.*, Vol. 39, No. 8, pp1167-1177, 1991.
- [13] E. Hallen, "Theoretical Investigations into the Transmitting and Receiving Qualities of Antennae", *Nova Acta Regiae Soc. Sci. Upsaliensis*, Ser. IV, No. 4, pp. 1-44, 1938.
- [14] K. K. Mei, "On the Integral Equations of Thin Wire Antennas", *IEEE Trans. on Ant. & Prop.*, Vol. 13, pp. 374-378, May 1965.
- [15] K. J. Bunch & R. W. Grow,, Numerical Aspects of the Boundary Residual Method", *Int. J. of Numerical Modeling: Electronic Networks*, Vol. 3, pp.57-71, 1990.
- [16] K. J. Bunch & R. W. Grow, "On the Convergence of the Method of Moments, the Boundary Residual Method and Point-Matching Method with a Rigorously Convergent Formulation of the Point-Matching Method", *Journal of the Applied Computational Electromagnetic Society*, Vol. 8, No. 2, pp. 188-202, 1993.
- [17] C. L. Lawson & R. J. Lawson, *Solving Least-Squares Problems*, Prentice-Hall, Inc., 1974.
- [18] M. M. Bibby, "A Comparative Study of Expansion Functions Using the Boundary Residual Method on a Linear Dipole – Part I: Entire-Domain Functions", *Journal of the Applied Computational Electromagnetic Society*, Vol. 17, No. 1, pp. 42-53, March 2002.
- [19] D. B. Miron, "The Singular Integral Problem in Surfaces", *IEEE Trans. on Ant. & Prop.*, Vol. Ap-32, No. 3, May 1983.
- [20] J. H .Richmond, "On the Edge Mode in the Theory of Thick Cylindrical Monopole Antennas", *IEEE Trans. on Ant. & Prop.*, Vol. 28, No 6, pp. 916-920, Nov. 1980.

**Malcolm M. Bibby** received the B.Eng. and Ph.D. degrees in Electrical Engineering from the University of Liverpool, England in 1962 and 1965 respectively. He has been interested in the numerical aspects associated with antenna design for the last twenty years.



## Wireless Propagation in Non Line of Sight Urban Areas using Uniform Theory of Diffraction

Grant A. Ellis

Department of Electrical and Computer Engineering  
National University of Singapore

*Abstract:* This paper describes a three-dimensional electromagnetic propagation model for signal power prediction in a non line of sight urban area located in Singapore. The model, which is implemented using the Ohio State NEC-BSC V4.2 basic scattering code and is based on ray theory and uniform theory of diffraction (UTD) takes into account first-order, second order, and third order effects including triple reflections and diffractions. The simplified propagation model of Raffles Place, the central business district of Singapore, uses more than 360 geometrical structures and is compared with data measured at 937.6 MHz along a drive route at the site. The results from the propagation model produced reasonable agreement with the measurements showing that a simplified model using UTD can be used to simulate the gross features of electromagnetic scatter in an urban area. It is shown that use of penetrable dielectric building walls are also necessary for accurate prediction of radio wave propagation in urban areas under non line of sight conditions. It is also found that third order scattering effects can be dominant in non line of sight situations and may be necessary for accurate predictions.

### 1 INTRODUCTION

As cellular mobile communications systems become more widely used, there is an increasing need to develop reliable planning tools for base station deployment. Part of this growth is due to frequency reuse whereby the same frequencies are utilized in geographically distinct areas or cells such that signal path loss over distance can be exploited. Frequency reuse provides for significantly greater capacity. One of the drawbacks with frequency reuse however, is the potential for interference between nearby cells. As cells become smaller in size, the use of reliable planning tools becomes even more necessary. In these environments, accurate signal strength prediction plays an important role in controlling intercell interference and providing coverage for low-power handheld units. The use of reliable planning tools means that the use of expensive and time-consuming measurements in the field can be

minimized. These tools can also provide a cost effective means of anticipating problems at the early stages of base station deployment and of optimizing parameters such as antenna location and orientation.

Several techniques have been developed [1-6] for analysis of multipath and other propagation effects in macrocellular and microcellular environments. In several of these approaches, ray tracing or launching techniques are combined with GTD/UTD (Geometrical Theory of Diffraction /Uniform Theory of Diffraction) to analytically determine the sum of all incident, reflected, and diffracted fields at the receiver location. The use of GTD/UTD is appropriate, since the frequencies used in mobile communications (e.g. > 900 MHz) are usually high enough such that the assumption that the features of most building structures are much larger than the wavelength used becomes valid. In [2], a computer based propagation model is used to obtain a time delay representation of the received signal. In [3, 4], a multislit waveguide with randomly distributed gaps between the sides of buildings is considered as a model of straight streets under line of sight conditions. In [5], a ray launching technique is used to detect the intersection of a ray with an object and the diffracted and reflected rays are then computed. This process is repeated until a maximum number of reflections is exceeded. In [6], 2D FDTD is corrected to account for spherical wave spreading and applied to a simple outdoor environment. Each building in the model consists of a perfectly conducting core with a dielectric coating.

In this paper, a particular urban area was selected, a three-dimensional model was created and the propagation characteristics were simulated using NEC-BSC V4.2 (Numerical Electromagnetic Code-Basic Scattering Code) [7]. The model presented includes contributions to the received signal from all possible propagation paths, including ground and wall reflections from diffracted and specularly reflected signals both in the LOS (Line of Sight) and NLOS (Non Line of Sight) regions using GTD/UTD. This code is structured such that all of one type of scattered

field or interaction is computed at one time to increase efficiency. Buildings having an arbitrary layout can be modeled even if the streets are not rectilinear and the buildings walls on each side of the streets are not coplanar.

The purpose of this research is to investigate how accurately UTD could predict electromagnetic scattering in a non line of sight urban environment using a simplified model consisting of plates and curved surfaces. In order to evaluate the limitations of the model, predictions from the model considering 1<sup>st</sup>, 2<sup>nd</sup>, and 3<sup>rd</sup> order scattering mechanisms were compared to CW test data measurements from a private cellular provider. This paper is organized as follows: Section 2 describes the urban propagation model, Section 3 compares the measured vs. predicted results, and Section 4 summarizes the results and provides some directions for future research.

## 2 URBAN PROPAGATION MODEL

The goal of this investigation was to determine how well UTD could be used to predict electromagnetic scattering in a heavily urbanized environment using a simplified model of the site. Raffles Place, the central business district of Singapore was chosen as an appropriate site for this study due to its high building density. Other reasons for choosing Raffles Place were:

1. The building layout does not lie completely in a rectangular grid. This allows for investigations to be carried out in an area without a rectangular grid layout and having a somewhat random building orientation.
2. Drive routes can be investigated which are mainly non-line-of-sight (NLOS).
3. The building heights in this area range from 5 to 282 meters. The effects of diffraction from the edges of rooftops and sides of buildings can be investigated.

Figure 1 shows a three-dimensional view of the geographical layout of Raffles Place used in the UTD model with the drive route shown. The drive route begins along Cecil Street and follows onto Collyer Quay up to Fullerton Square then turns left onto Battery Road where it ends on Chulia Street. The area covered is about 500 m by 500 m and the length of the drive route is 1.12 km. The data predicted along this route is compared with the measured drive data collected by MobileOne, a private cellular network provider in Singapore. In all field measurements, GPS was used to record the

location of the measured signal power along the route. The following input model parameters are required in the NEC-BSC UTD code [7]:

1. Coordinates of the plates, curved surfaces, and other structures necessary to simulate building exterior and roofs.
2. Estimate of the electrical permittivity, conductivity, and thickness of the building exteriors.
3. Transmitter and receiver locations.
4. Transmitter and receiver antenna patterns.
5. Operating frequency used.
6. Types and order of UTD interactions to be included in the simulation.

The coordinates of the building exteriors were extracted from an aerial map by using an overlay having a fixed origin selected on the map. The corners of the buildings were measured relative to this origin. Most building shapes were modeled using only plates, which were assumed to be flat surfaces having average electrical permittivity and conductivity. Structures having low curvature sections were modeled using multiple plates to form a piecewise linear approximation of that section. When the radius of curvature of the structure was substantial, cylinders or truncated cones were used. Elliptic cylinders were also used to model some building structures.

The ground plane was simulated using a single homogeneous half space of a relative dielectric permittivity  $\epsilon_r = 10$  and conductivity  $\sigma = 0.001$  S/m, which can be considered reasonable for a typical ground. Preliminary studies suggest that the predicted signal power near the ground is somewhat insensitive to the ground dielectric constant and conductivity. The seawater surface was also included in the model and was modeled as a dielectric coated plate with a relative permittivity of  $\epsilon_r = 80$  and electrical conductivity  $\sigma = 4$  S/m

The model database used in the UTD propagation model consists of 360 plates and 5 cylinders to represent the 64 buildings and other structures located at Raffles place. The number of plates in the model could easily exceed 500 if the entire area is to be accurately modeled. However, following the assumption that effects from structures like trees, lamp posts, telephone boxes, Mass Rapid Transit station buildings, etc can be ignored, these structure were not included in the model [8]. Every attempt was made to define the model in more detail in areas where it was illuminated strongest by the antenna. Because of

the wide variation in building heights, the detailed description in the model is not limited to the area local to the transmitter. Since the model used omnidirectional antennas for the transmitter and receiver, the entire area including but not limited to the region between the transmit antenna and the receiver field point was modeled. As a result of the above, the number of plates required for modeling was quite large to account for all the possible ray paths.

The building exteriors were modeled as dielectric plates to approximate materials, such as glass windows, absorbing panels, concrete, etc. Research is still underway to produce useful approximations for the thickness, permittivities and conductivities of these dielectric layers [8]. The choice of a good approximation for the electrical properties is of utmost importance, since the Fresnel reflection coefficients depend on these values. These coefficients dictate the reflection coefficient of the materials influencing the modeled results.

The buildings located at Raffles Place were constructed using a variety of materials, such as concrete, glass, and steel. It is difficult to identify the electromagnetic properties of each individual building exterior and it is assumed that all the building walls have electrical property values averaged over those of glass and concrete. The building walls were modeled using plates and cylinders coated with dielectric on one side to simulate the building exterior and a perfect electric conductor on the other. The material properties were chosen as  $\epsilon_r = 15$ ,  $\sigma = 7$  S/m, and thickness = 0.5 meter [9, 10]. The accuracy of the model is limited by the lack of accurate building and street databases and the approximation of building exteriors to be "smooth" flat surfaces having an average relative permittivity and conductivity.

Both the transmitter and receiver antennas were simulated using vertically polarized half-wave dipoles. The transmitter input power was 32.4 dBm. The transmitter dipole antenna was placed 3 m above the machine room on the rooftop of Ocean Building, a building of about 120 m in height. The receiver was placed 2 m above the ground to simulate mounting of a vertical monopole on top of a car. The measured data was taken at intervals of between 28 - 59 m using a GPS based measurement system. The simulated data is sampled in 20 m intervals with and without spatial averaging. All UTD scattering mechanisms were selected during the simulation. The NEC-

BSC UTD code however, allows for the individual scattering terms to be selected to investigate their behavior along the route.

### 3 COMPARISON OF THE MEASURED VS. PREDICTED RESULTS

Three sets of simulation cases were considered. The first simulation case considers only the 1<sup>st</sup> and 2<sup>nd</sup> order interaction terms listed in Table 1. The second simulation case considers up to and including the 3<sup>d</sup> order interactions. The additional 3<sup>d</sup> order interaction terms are listed in Table 2. For these first two cases, the building walls only reflect and diffract the radio waves using the material dielectric properties given. The third simulation case considers 1<sup>st</sup>, 2<sup>nd</sup>, and 3<sup>d</sup> order interactions listed in Tables 1 and 2 using penetrable dielectric plates as building walls. For this case, radio waves are both reflected and transmitted through the plates to simulate propagation through building structures.

Figure 2 shows a comparison between the predicted signal powers resulting from the first two simulation cases (1<sup>st</sup> and 2<sup>nd</sup> order interactions only, and 1<sup>st</sup>, 2<sup>nd</sup> and 3<sup>rd</sup> order interactions) and the measured fields. The 1<sup>st</sup> and 2<sup>nd</sup> order interaction terms listed in Table 1 result in a total of 5015 ray paths along the drive route. Table 2 lists the 3<sup>d</sup> order interaction terms resulting in an additional 42850 ray paths. The curve showing all 1<sup>st</sup>, 2<sup>nd</sup> and 3<sup>d</sup> order interactions appears to give better agreement with the measured field data.

The greatest discrepancy between the measured and predicted data for cases 1 and 2 occurs over the 0.2 km stretch located immediately before point D near Fullerton Square (Figure 1). The predicted results for the case of up to 3<sup>rd</sup> order interactions underestimate the measured data by more than 20 dB. This is difficult to explain using the model because there are no nearby structures located in this area on which the rays can get scattered. Along the drive route to the right of Collyer Quay is an open area immediately adjacent to Marina Bay. One possible explanation for the discrepancy between the measured and predicted data is the lack of radio wave propagation through buildings since modern office-building interiors are composed of mostly air. Studies have shown that radio waves may penetrate into buildings with only between 9-11 dB attenuation at 900 MHz [11]. Our model was modified to allow the building walls to be penetrable by radio waves such that the total attenuation through the building structures is

between 12-15 dB. The properties of the building walls were changed to  $\epsilon_r = 15$ ,  $\sigma = 0.0023$  S/m, and thickness = 1 m and were simulated as penetrable dielectric plates. Shown in Figure 2 is the measured vs. predicted signal power along the drive route in Figure 1 using penetrable walls. The correspondence between measured and predicted power is much better than for the cases where the building walls only provide reflection and diffraction. It can be observed that use of penetrable building walls results in 11 dB less variation in the predicted field along the drive route than for the case of 3<sup>rd</sup> order scatter only. Table 3 lists the RMS error and standard deviation for each simulation case.

Additional observations can be made from the measured vs. predicted signal power results shown in Figure 2. At location A on Cecil Street, the peak in the measured received field may be attributed to 3<sup>rd</sup> order interactions since this peak cannot be seen in the 2<sup>nd</sup> order results. For instance, in the prediction, a 3<sup>rd</sup> order reflection occurs between the Singapore Land Tower building, the OUB Center, and a second reflection from the Singapore Land Tower (Figure 3). Multiple interactions between the Ocean Building and the Ocean Towers also occur before the ray arrives at the receiver location.

At location B, the measured signal power is at the lowest level along the drive route and the number of 2<sup>nd</sup> and 3<sup>rd</sup> order ray paths appears to be minimum. At location B the only contribution to the signal power at the receiver location appears to be from the diffraction from the rooftop of the Ocean building. This location is also the point closest to the transmitter along the drive route.

At location C, the predicted results that include up to 2<sup>nd</sup> order interactions only indicate a drop of nearly 50 dB in the received signal strength due to obscuration by an overpass located along the route. For the predicted results that include 3<sup>rd</sup> order interactions, the effect of the overpass is minimal. The measured signal power also indicates essentially no effect due to the overpass. The effects of the 3<sup>rd</sup> order interactions appear to be dominant directly under and immediately beyond the overpass. Multiple rays that originate at the transmitter location may be diffracted from the rooftop edge on top of the Ocean Building and then diffract and reflect from the north side of the John Hancock building. These rays are then reflected from the sides of both the Union Overseas Shopping Center and a restaurant and then finally are reflected from the side of the Hitachi Center

(see Figure 4) to the receiver location immediately beyond the overpass location.

Probably the most interesting observation in the measured and predicted data is shown at location D. Here, the measured and predicted signal powers are at their maximum value over the entire route. Location D is in front of the Singapore Land Tower on Battery Road. The received signal power is about 12 dB above the average signal power along the entire route. At this location, the transmit antenna on the Ocean Building is obstructed by several buildings. The received signal appears to come from several ray paths that first begin as reflections from the OUB Center and UOB Plaza and then are reflected from the Singapore Land Tower and Standard Chartered buildings to the receiver location. This area of Battery Road appears to behave like a parallel-plate waveguide so that the rays from several locations are guided into a relatively narrow street bounded by the Singapore Land Tower on one side and Standard Chartered Bank and May Bank on the other side (see Figure 5).

At the end of the route and furthest from the transmitter on Battery street (location E) is the location of the largest discrepancy between the 2<sup>nd</sup> and 3<sup>rd</sup> order predicted data. The measured signal power in the area around location E however, is nearly constant. The predicted data however, shows almost a 50 dB variation for the 1<sup>st</sup> and 2<sup>nd</sup> order interactions and nearly 27 dB of variation for the case of up to 3<sup>rd</sup> order interactions. The predicted data shows a 2<sup>nd</sup> order interaction that is the result of a specular reflection from the City House building and then diffraction between the edges of the Exchange Building and Golden Shoe Car Park (Figure 6) to the receiver location. The measured power increase is only about 1 dB at this location. Rays reflected from the Republic Plaza and the UOB Plaza channel into this area resulting in a peak in the received signal power. Like the results shown at location D, this area may behave like a parallel-plate waveguide where multiple reflections occur between UOB Plaza on one side and the Sinsov building on the other side across Battery Street.

#### 4 CONCLUSION

In this paper, a simplified model using UTD with ray tracing and consisting of 360 plates and 5 cylinders was used to predict high-frequency electromagnetic wave propagation in an urban environment. Taking into account single, double,

and third order UTD terms interacting between building walls and corners, the gross features of the electromagnetic response were accurately predicted. The three-dimensional model was developed using arbitrary building layouts modeled using simple structures constructed using plates to represent flat surfaces and cylinders for curved surfaces.

Several sets of UTD simulations were performed and the resulting predicted signal powers were compared with measurements along the drive route located in Raffles Place, the central business district of Singapore. Comparisons between the predictions and measurements suggest that:

1. When there is no line of sight (NLOS), diffraction cannot be neglected. The effects of diffraction from the edges of the rooftop appeared to be significant at the transmitter location. 1<sup>st</sup> and 2<sup>nd</sup> order interactions alone may not be sufficient for accurate predictions. Inclusion of higher order scattering is important for the accurate prediction of the scattering in NLOS situations. Inclusion of 3<sup>rd</sup> order interactions also result in 9 dB less variation than 2<sup>nd</sup> order interactions in the predicted signal power along the drive route.
2. For NLOS cases, the fields at the receiver location often result from scattering on structures local to the receiver location. These fields may also result from reflections from large structures or surfaces far away from the receiver location. This can result in propagation paths that may not be intuitively obvious. These higher order scattering terms (3<sup>rd</sup> order and above) may require a larger model to account for all possible ray paths.
3. Lack of sufficient structures in the propagation model and inaccuracies in antenna positions, route locations, may introduce errors into the predicted signal powers. Another source of potential error is scattering from cars, trucks, or other vehicles located near the receiver and not included in the model. It was also assumed that the dielectric constant and conductivity of the building exteriors throughout the model was constant. These simplifications introduce extra error.
4. UTD can also produce artifacts in the predicted fields. At some locations considering up to 2<sup>nd</sup> order interactions only result in artifacts not observed in the measured data. At those locations, the 3<sup>rd</sup> order scatter is dominant over the 1<sup>st</sup> and 2<sup>nd</sup> order scatter effects.
5. At two locations along the drive route, it was found that the peak in the received signal power might be the result of a parallel-plate waveguide effect caused by multiple reflections between adjacent buildings separated by a street or road.
6. Effects of radio wave propagation through building walls and structures are necessary in resolving differences between measured and predicted data under NLOS conditions. Use of penetrable building walls in the model reduces the RMS error in the prediction by 13 dB.

Future work may include incorporation of higher order (e.g. 4<sup>th</sup> order) interaction terms in the propagation study. This may be useful for the prediction of the signal power near Fullerton Square. The dielectric properties of the building exteriors are also very important and may have a large effect on the magnitudes of reflections from buildings. Future work includes additional modeling of propagation through buildings. Analysis of these effects will be helpful in resolving differences between measured and predicted signal power data. Also of interest are the cross-polarized fields scattered in non line of sight locations, for the study of polarization diversity antenna schemes.

#### ACKNOWLEDGMENTS

The author wishes to thank the following for their contributions:

1. MobileOne for providing the CW drive test measurement data.
2. Building and Construction Authority of Singapore for providing a detailed map of Raffles Place.
3. To my student, Cheong Si Neng for the Raffles Place model.
4. Ronald J. Marhefka at The Ohio State University Electroscience Laboratory for strong support and help in using the NECBSC code.

## REFERENCES

- [1] F. Ikegami, T. Takeuchi, S. Yoshida, "Theoretical prediction of mean field strength for urban mobile radio", *IEEE Trans. on Ant. and Prop.* Vol. 39, No. 3, pp. 299-302, March 1991.
- [2] J. P. Rossi, J.C. Bic, A. J. Levy, Y. Gabillet, M. Rosen, "A ray launching method for radio-mobile propagation in urban area", *IEEE Ant. and Prop. Symp.*, Vol. 3, pp. 1540-1543, June 1991.
- [3] N. Blaunstein, M. Levin, "Propagation Loss in the Urban Environment with Rectangular Grid-Plan Streets", *10<sup>th</sup> International Conference on Antennas and Propagation*, pp. 2.178-2.181, 14-17 April 1997.
- [4] N. Blaunstein, R. Giladi, and M. Levin, "Characteristics' Prediction in Urban and Suburban Environments", *IEEE Trans. Veh. Tech.*, Vol. 47, No. 1., pp. 225-234, Feb. 1998.
- [5] S. Y. Tan, H. S. Tan, "Propagation model for microcellular communications applied to path loss measurements in Ottawa city streets", *IEEE Trans. on Veh. Tech.*, Vol. 44, No.2, pp. 313- 317, May 1995.
- [6] J. Schuster and R. Luebbers, "Comparison of GTD and FDTD Predictions for UHF Radio Wave Propagation in a Simple Outdoor Urban Environment," *IEEE APS Int. Symp. Dig.*, Montreal, Canada, Vol. 3. pp. 2022-2025, July 1997.
- [7] R. J. Marhefka, J.W. Silvestro, "Near-zone basic scattering code, User's manual with space station applications" Technical Report 716199-13, March 1989.
- [8] M. F. Catedra, J. Perez, F. Saez de Adana, and O. Gutierrez, "Efficient ray-tracing techniques for three-dimensional analyses of propagation in mobile communications: application to picocell and microcell scenarios", *IEEE Antennas and Prop. Magazine*, Vol. 40, No. 2, pp. 15-28, April 1998.
- [9] S-C Kim, B. J. Guarino Jr., T. M. Willis III, V. Erceg, S. J. Fortune, R. A. Valenzuela, L. W. Thomas, J. Ling, and J. D. Moore, "Radio propagation measurements and prediction using three-dimensional ray tracing in urban environments at 908MHz and 1.9GHz", *IEEE Trans. on Veh. Tech.*, Vol. 48, No. 3, pp. 931- 946, May 1999.
- [10] O. Landron, M. J. Feuerstein, and T. S. Rappaport, "In Situ Microwave Reflection Coefficient Measurements for Smooth and Rough Exterior Wall Surfaces", in Proc. 43<sup>rd</sup> *IEEE Veh. Technol. Conf.*, pp. 77- 80, 1993.
- [11] A. M. D. Turmani, A. F. de Toledo, "Modeling of radio transmissions into and within multistory buildings at 900, 1800, and 2300 MHz", *IEE Proc. I*, 140, (6), pp. 462-470, 1993.



Grant A. Ellis was born in Portland, OR in 1960. He received the B.S. and M.S. degrees in electrical engineering from Washington State University, Pullman, WA, in 1983 and 1986, respectively, and the Ph.D. degree in electrical engineering from the University of Washington, Seattle, in 1995. From 1983 to 1985 he was a staff engineer with the Boeing Aerospace Company, and from 1987 to 1998 he was a principal engineer with the Boeing Defense and Space Group. He was an assistant professor of electrical engineering with the National University of Singapore from 1998 to 2001. He is presently a member of the research staff of HRL Laboratories in Malibu. His current research interests are in microwave circuit design including monolithic MIC design, active antenna design, and propagation analysis.

Dr. Ellis is a member of Tau Beta Pi, Eta Kappa Nu, ACES, and the IEEE.

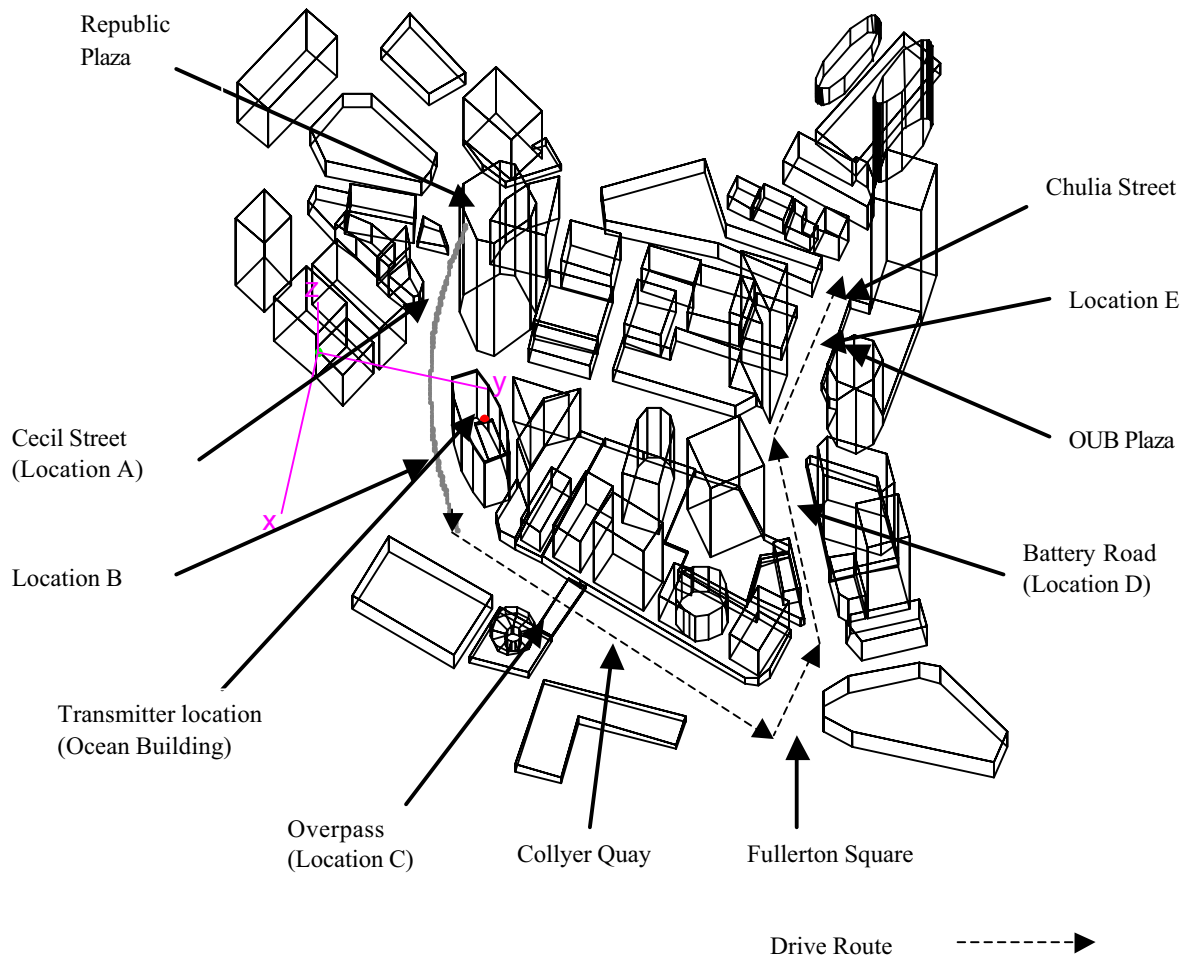


Figure 1. UTD model of Raffles Place and drive route.

Table 1. 1<sup>st</sup> and 2<sup>nd</sup> order interactions considered in case 1.

RP	Single Reflection from plates
RPRP	Double reflection from plates
DP	Single edge diffraction
VP	Single corner diffraction
RPDP	Plate Reflection – Edge Diffraction
RPVP	Plate Reflection – Corner Diffraction
DPRP	Edge Diffraction – Plate Reflection
VPRP	Corner Diffraction – Plate Reflection
DPDP	Edge Diffraction – Edge Diffraction
DN	Diffraction from End Cap Rim
RN	Reflection from End Cap
DC	Diffraction from Curved Surface
RC	Reflection from Curved Surface

Table 2. 3<sup>rd</sup> order interactions considered in case 2.

RPRPRP	Triple reflection from plates
RPRPDP	Double Plate Reflection – Edge Diffraction
RPRPVP	Double Plate Reflection – Corner Diffraction
RPDPRP	Plate Reflection – Edge Diffraction – Plate Reflection
RPVPRP	Plate Reflection – Corner Diffraction – Plate Reflection
DPRPRP	Edge Diffraction – Double Plate Reflection

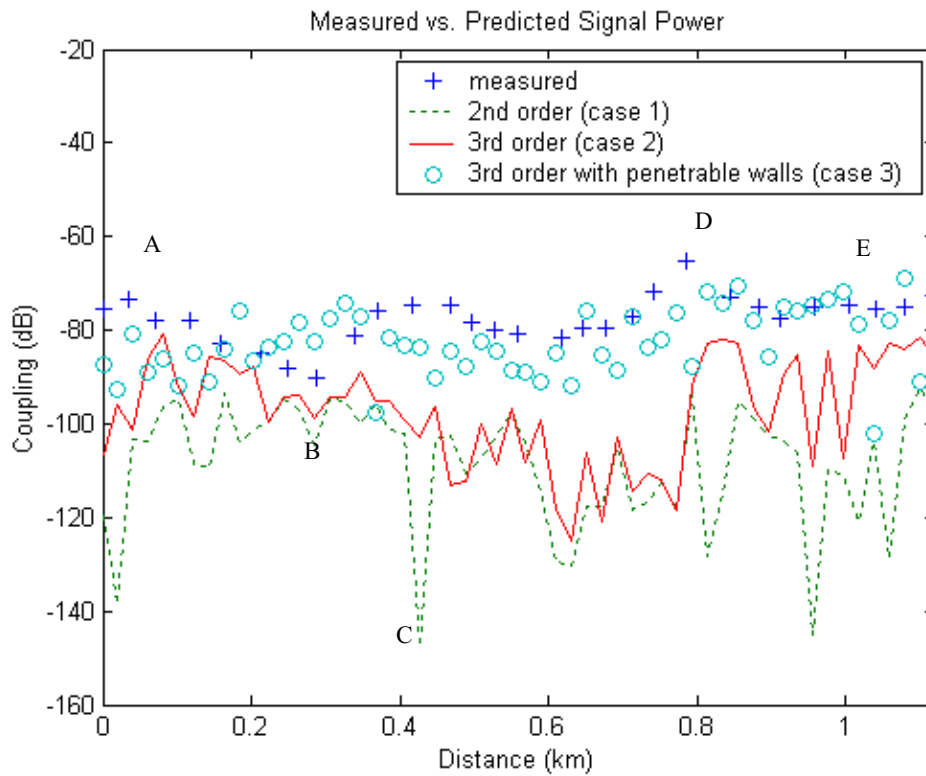


Figure 2. Measured and predicted signal power along drive route.

Table 3. RMS error and standard deviation between measured and predicted power along drive route.

Case	Order of interactions included in model	RMS Error	Standard Deviation
1	1 <sup>st</sup> , 2 <sup>nd</sup>	33.0 dB	13.2 dB
2	1 <sup>st</sup> , 2 <sup>nd</sup> , 3 <sup>rd</sup>	22.5 dB	13.1 dB
3	1 <sup>st</sup> , 2 <sup>nd</sup> , 3 <sup>rd</sup> with penetrable walls	9.2 dB	8.1 dB



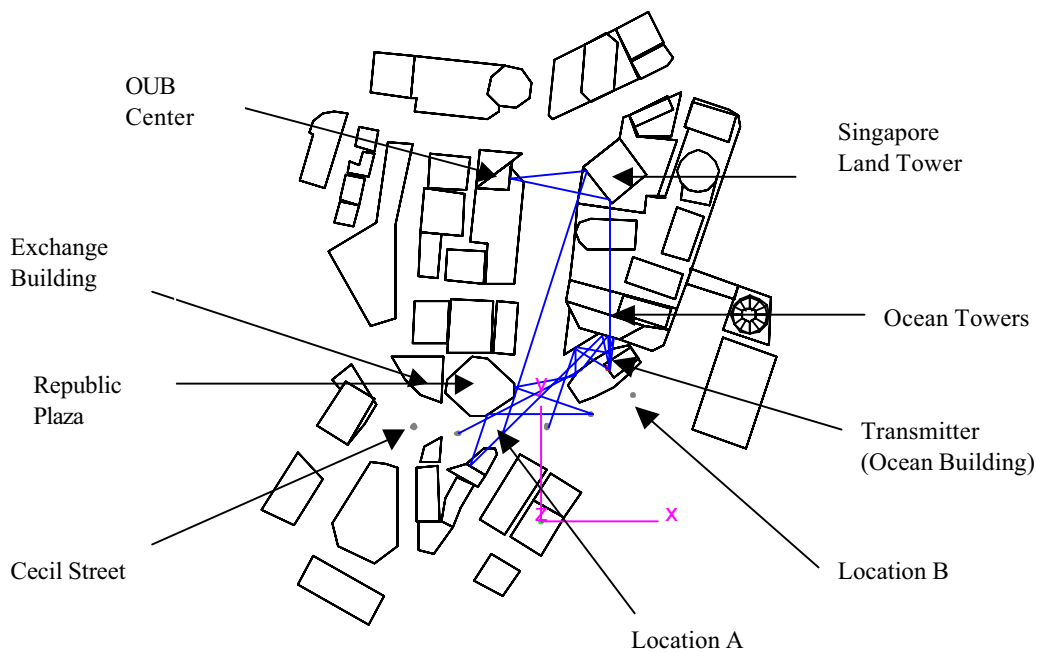


Figure 3. Major Ray Contributions at locations A and B along Cecil Street.

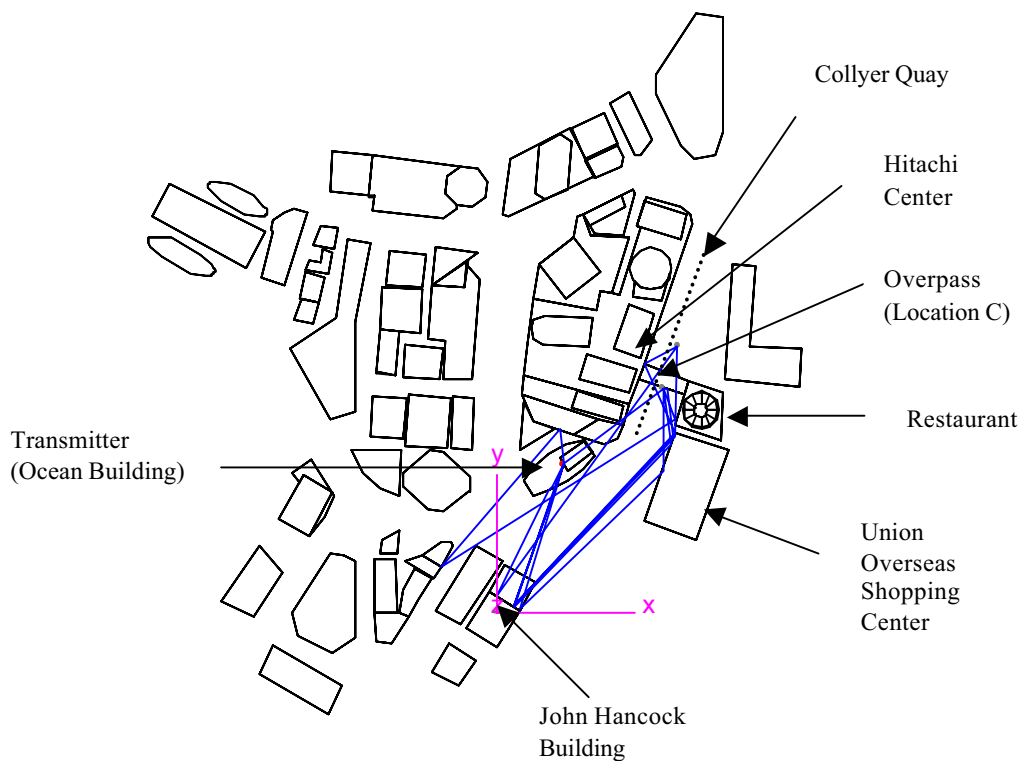


Figure 4. Major Ray contributions at Overpass (Location C).

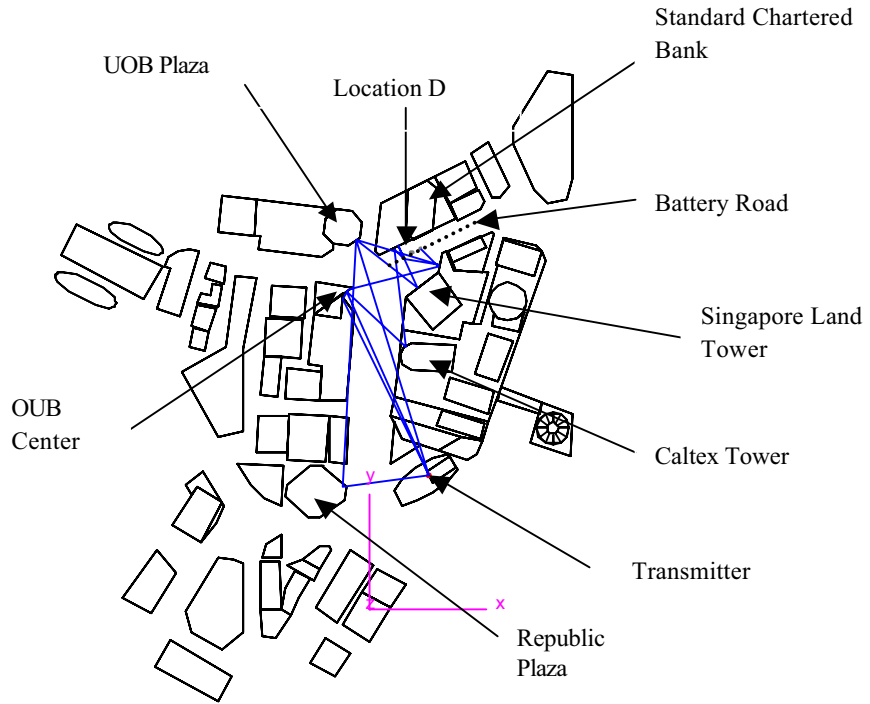


Figure 5. Major Ray Contributions at location D.

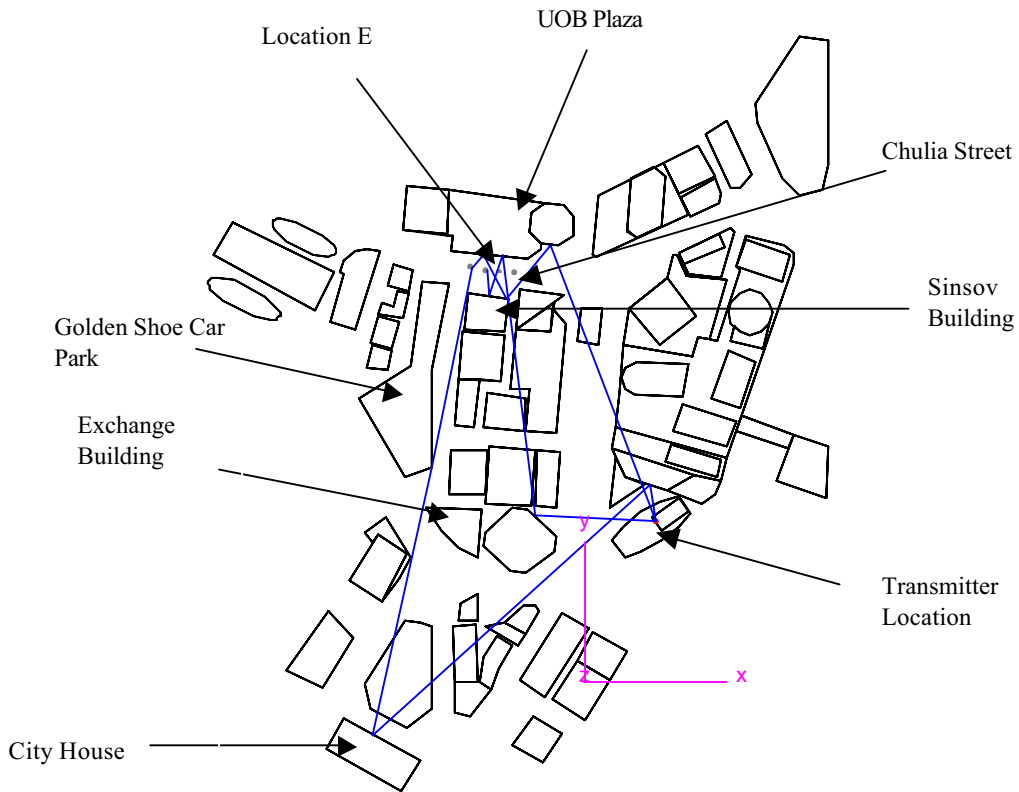


Figure 6. Major Ray contribution at Location E.

# AUTOMATIC CALCULATION OF BAND DIAGRAMS OF PHOTONIC CRYSTALS USING THE MULTIPLE MULTIPOLE METHOD

Jasmin Smajic, Christian Hafner, Daniel Erni  
Laboratory for Electromagnetic Fields and Microwave Electronics  
Swiss Federal Institute of Technology  
ETH-Zentrum, Gloriastrasse 35, CH-8092 Zürich, Switzerland  
E-mail: [jsmajic@ifh.ee.ethz.ch](mailto:jsmajic@ifh.ee.ethz.ch)

**ABSTRACT** – In the framework of photonic crystal's band structure calculations, we present a novel way – based on several advanced techniques for searching and tracing eigenvalues with the multiple multipole program – to compute these diagrams automatically, efficiently, and with a high accuracy. Finally, we validate the results for some well known test cases.

**Keywords** – band diagram; multiple multipole program; photonic crystal; eigenvalue analysis.

## I. INTRODUCTION

PHOTONIC Crystals (PhCs) were proposed in 1987 by E. Yablonovitch [1] at the University of California, as an optical counterpart to semiconductors, i.e., PhCs should provide a photonic bandgap in the same way that a semiconductor possesses an electronic bandgap. In fact, PhCs are rarely found in nature. Exceptions are opals and butterfly wings. However, thanks to nano-technology it has become possible to fabricate artificial PhCs in the last decade. These PhCs essentially consist of a periodic assembly of dielectric scatterers, i.e., there is a strong link to the well-known structures of grating theory. One of the important differences between PhCs and semiconductors is the size of the unit cell. For a semiconductor, one has a 3D grid consisting of identical atoms, i.e., the lattice constant in all three directions of the crystal is in the order of the diameter of an atom, whereas the cell size of a PhC is in the order of half an optical wavelength, i.e., much larger. From this fact, one expects that the Photonic Integrated Circuits (PICs) based on PhC concept must be much larger than the traditional semiconductor ICs. But – because of the macroscopic size of the PhC's unit cell – one has much more freedom in introducing and fabricating defects in a PhC than in a semiconductor. Note that a semiconductor becomes interesting from the technological point of view only when a few impurities or defects are introduced and the same holds for PhCs. Doping traditional semiconductors is a rather statistical way of introducing defect atoms in a semiconductor and therefore, the building blocks of semiconductor are relatively large blocks of material with a specific doping. These blocks obviously consist of many atoms. When designing a "doped" PhC, one can precisely position and fabricate all defects with a high degree

of freedom – at least it is expected that this can be done in the near future [2].

Although the variety of PhC structures that might be fabricated one day seems to be almost infinite and although many interesting structures were already proposed (various types of waveguides, sharp bends in waveguides without any reflection, couplers, resonators, etc.) or even fabricated on a prototype level, one currently cannot say what kind of PhC structures will be favored. At the moment, one can neither know the materials that are best suited for PhCs – it is well known that a large dielectric contrast is required for obtaining a bandgap, which somehow limits the materials that may be used, but there is no unique choice at all – nor what kind of geometry (2D crystals or 3D crystals [3-5], symmetry, shape of the scatterers) is most appropriate. Thus, there is a strong need for theoretical investigations and simulations of potential structures. The first step of such investigations consists in the computation of the band diagrams of perfect PhCs without any defects. The goal is to find structures that may easily be fabricated and exhibit a broad band gap, i.e., a frequency range where no electromagnetic waves are allowed to propagate within the crystal. In order to find the band gap, one must compute the band diagram of the lowest order modes of the PhC. This is essentially an eigenvalue problem that exhibits several special cases that may cause difficult numerical problems, especially when one is designing a procedure for the automatic, efficient, accurate, and reliable computation of the complete band diagrams for arbitrary structures.

Currently, the most frequently used approach is the Plane Wave Method (PWM) that mainly approximates the electromagnetic field by a superposition of plane waves [6-10]. It is well known, that this method has a problematic convergence [11-13, 10]. Other methods that were used for PhCs are the Finite Difference Time Domain (FDTD) [14,15], the transfer matrix method [16], the Finite Element Method (FEM) [17], and the Boundary Element Method (BEM) [18]. In the following, we apply the latest version of the Multiple Multipole Program (MMP) [19] implemented in the MaX-1 software [20].

In order to obtain efficient, reliable, and accurate results, we carefully analyze the numerical problems that may occur and introduce several new techniques. For reasons of simplicity we focus on the 2D case.

The remainder of the paper is organized as follows: A commonly used representation of PhCs in terms of their band diagram is elucidated in Section II. In Section III we briefly explain the core of our photonic crystal calculations, when MMP is considered. The proper framework of the eigenvalue search is reported in Section IV, whereas in Section V a successful automation of such search procedure is proposed. A validation of our band structure calculation by means of various test examples is given in Section VI. And finally, we conclude this contribution with a short summary in Section VII.

## II. DEFINITION OF THE BAND DIAGRAM

As an introductory example let us consider the simple case of a 2D PhC consisting of dielectric rods arranged in a square lattice and embedded in, e.g., air. For periodic structures it is possible to apply some fundamental theorems from solid state physics. The original lattice for this crystal is given on the left hand side of Fig. 1. For the dielectric constant we can write  $\varepsilon(\vec{r}) = \varepsilon(\vec{r} + \vec{R})$  where  $\vec{R}$  is one of the original lattice vectors. According to Bloch's theorem [6, 7] for the modal field inside the crystal we write:

$$\vec{E} = \vec{E}_{\vec{k}n}(\vec{r}) = \vec{u}_{\vec{k}n}(\vec{r}) \cdot e^{i\vec{k}\cdot\vec{r}} \quad (1)$$

$$\vec{u}_{\vec{k}n}(\vec{r}) = \vec{u}_{\vec{k}n}(\vec{r} + \vec{R}) \quad (2)$$

Note that (1) holds not only for the electric but also for the magnetic field. Bloch's theorem may be proven in classical electro-dynamics [6]. Important consequences of this theorem are [6, 7]:

1.  $e^{i\vec{k}\cdot\vec{R}} = 1$ , i.e.,  $\vec{k}\cdot\vec{R} = N \cdot 2\pi$ , where  $N$  is an integer – the wave vector space (reciprocal space) is discrete,
2.  $\vec{E}_{\vec{k},n}(\vec{r}) = \vec{E}_{\vec{k}+\vec{G},n}(\vec{r})$ , i.e., the reciprocal space is periodic.  $\vec{G}$  is one of the reciprocal lattice vectors.

This allows us to define the so-called reciprocal lattice space, spanned by the reciprocal lattice vectors. We first define the original lattice vectors as follows:

$$\vec{R} = \eta_1 \vec{e}_1 + \eta_2 \vec{e}_2 + \eta_3 \vec{e}_3 \quad (3)$$

where  $\vec{e}_1$ ,  $\vec{e}_2$ ,  $\vec{e}_3$  are three independent lattice vectors and  $\eta_1$ ,  $\eta_2$ ,  $\eta_3$  are integer numbers. Note that  $\vec{e}_3$  is missing in 2D crystals. Similarly, we write for the primitive reciprocal lattice vectors:

$$\vec{G} = \kappa_1 \vec{f}_1 + \kappa_2 \vec{f}_2 + \kappa_3 \vec{f}_3 \quad (4)$$

If we want to construct the reciprocal lattice, we can use [7]:

$$\vec{f}_1 = 2\pi \frac{\vec{e}_2 \times \vec{e}_3}{\vec{e}_1 \cdot (\vec{e}_2 \times \vec{e}_3)}, \quad \vec{f}_2 = 2\pi \frac{\vec{e}_3 \times \vec{e}_1}{\vec{e}_2 \cdot (\vec{e}_3 \times \vec{e}_1)}, \quad \vec{f}_3 = 2\pi \frac{\vec{e}_1 \times \vec{e}_2}{\vec{e}_3 \cdot (\vec{e}_1 \times \vec{e}_2)}$$

These equations are derived from the definition of the reciprocal lattice vector space. For 2D crystals (cylindrical geometry), the vector  $\vec{f}_3$  is omitted and the vector  $\vec{e}_3$  is the unit vector  $\vec{e}_z$  along the cylinder axis.

From the equations above, we can conclude that the discrete translational symmetry of a photonic crystal leads to the fact that modes with the wave vector  $\vec{k}$  and modes with the wave vector  $\vec{k} + \vec{G}$  are identical, i.e., we have periodicity also in the reciprocal space. A special representation of the primitive cell for this periodicity is called the first Brillouin zone (1<sup>st</sup> BZ). It can be defined as a zone around any lattice point in the reciprocal space with points that are closer to this lattice point than to any other lattice point.

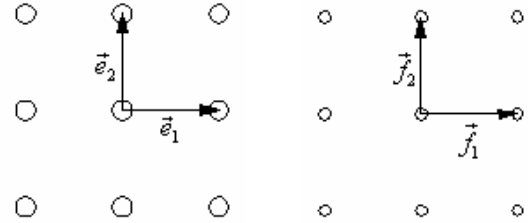


Fig. 1: The original (left) and reciprocal (right) lattice for a 2D photonic crystal (square lattice). Construction details for reciprocal lattice are given in the text.

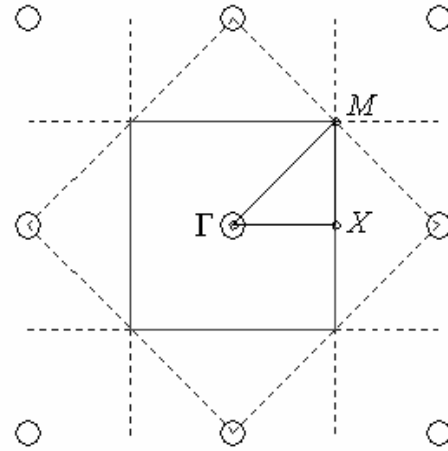


Fig. 2: Construction of the 1<sup>st</sup> Brillouin zone (solid square), its irreducible part (triangle  $\Gamma$ -X-M) and characteristic points for band structure computation ( $\Gamma$ , X, and M).

The Brillouin zone construction (using Bragg's planes – dashed lines) for the square lattice is shown in Fig. 2. Because of the high degree of symmetry, we need to analyze only a small part of the 1<sup>st</sup> BZ. This part is called the *irreducible BZ* (IBZ), [6, 7]. In the case of periodic structures,

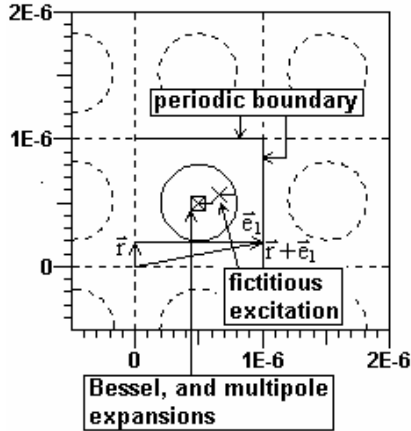


Fig. 3: The unit cell of the photonic crystal with dielectric rods arranged on a square lattice.

it is sufficient to perform the modal field analysis in the area of the IBZ. As illustrated in Fig. 2 the IBZ for a square lattice is a triangle with the corners  $\Gamma$ , X, and M. Since the maxima and minima of the eigenvalues (resonance frequencies) are supposed to be on the borders of the IBZ, it is sufficient to trace the eigenvalues along the sides of the IBZ in order to get the photonic bandgaps. Therefore, the standard band diagram consists of three sections:  $\Gamma$ -X, X-M, and M- $\Gamma$  (see Fig. 5). For other lattices, the procedure is essentially the same [21, 22]. Assume that an arbitrary point in the reciprocal space is considered. This point essentially defines a wave vector. For the periodicity of (3) we then obtain for the field in the original space:

$$\vec{F}(\vec{r} + \vec{R}) = \vec{F}(\vec{r}) \cdot e^{i\vec{k}\cdot\vec{R}} = \vec{F}(\vec{r}) \cdot e^{i(C_1 n_1 |\vec{k}_1| + C_2 n_2 |\vec{k}_2|)} \quad (5)$$

where  $F$  stands for the electric as well as for the magnetic field. In the MMP implementation of the periodic boundary problem  $C_1$ ,  $C_2$  are parameters that characterize the point in the reciprocal lattice space. As a consequence, it is sufficient to know the field in a unit cell (as an equivalent representation of the primitive cell) of the original space. Let us call this the original cell. Note that neither the shape nor the location of the original cell is unique, but for both the square and the hexagonal lattice we may simply use quadrangular original cells as shown in Fig. 3 and 4.

For the square lattice, the relation between the periodic constants ( $C_1$ ,  $C_2$ ) and the position in the IBZ is very straight forward, i.e., these are the Cartesian components ( $C_x$ ,  $C_y$ ) of the wave vector  $\vec{k}$ . For the hexagonal lattice, the situation is a bit more complicated [23-25].

### III. THE MMP SOLUTION OF PERIODIC PROBLEMS WITH FICTITIOUS BOUNDARIES

Any software for computing band diagrams must handle both eigenvalue problems and periodic structures. The MMP implementation of MaX-1 contains a simple concept for handling arbitrary periodic structures: First, the structure is

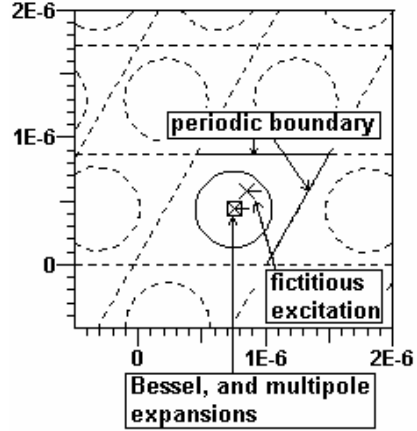


Fig. 4: The unit cell of the photonic crystal with dielectric rods arranged on a hexagonal lattice.

subdivided into cells by an appropriate grid of fictitious boundaries (dashed lines in Fig. 3 and Fig. 4). Assume that the field in one of the infinitely many cells is known, then, the field in all other cells is easily obtained from the periodicity conditions (5), i.e., the Floquet theorem [7].

The geometric shape of the original cell depends on the crystallographic structure (i.e. the crystal symmetry), but it is not unique for a given crystallographic structure at all, because the fictitious boundaries we have introduced, are quite ambiguous. For example, in Fig. 3 we used straight lines between the circular rods. We could replace these lines by curved, periodic lines and we could move these lines to any other position in space. Since we will impose so-called periodic boundary conditions along the fictitious boundaries of the original cell, we have to minimize the numerical problems when we select the fictitious boundaries in such a way that the electromagnetic field along them is as well behaved as possible. Therefore, straight lines in the middle between neighbor rods are most reasonable when the rods are circular or rectangular. When the geometric shape of the rods is more complicated, it may be advantageous to use curved lines.

Once, the original cell is isolated by introducing fictitious boundaries, we can derive boundary conditions for the field along them. In 2D PhCs, the original cell is bounded by two pairs of parallel lines. For example, when  $\vec{r}$  is a point on the left border of the original cell in Fig. 3,  $\vec{r} + \vec{e}_1$  is the corresponding point on the right border, where  $\vec{e}_1$  corresponds to one of the primitive lattice vectors. Because of the periodicity, we obtain from (5):

$$\vec{F}(\vec{r} + \vec{e}_1) = \vec{F}(\vec{r}) \cdot e^{i(C_1 |\vec{k}_1|)} \quad (5')$$

This condition holds for both the electric and the magnetic field in every point along the right boundary of the original cell. We call this the periodic boundary condition that is imposed on the right border of the original cell. Similarly, we can introduce a periodic boundary condition for the upper border.

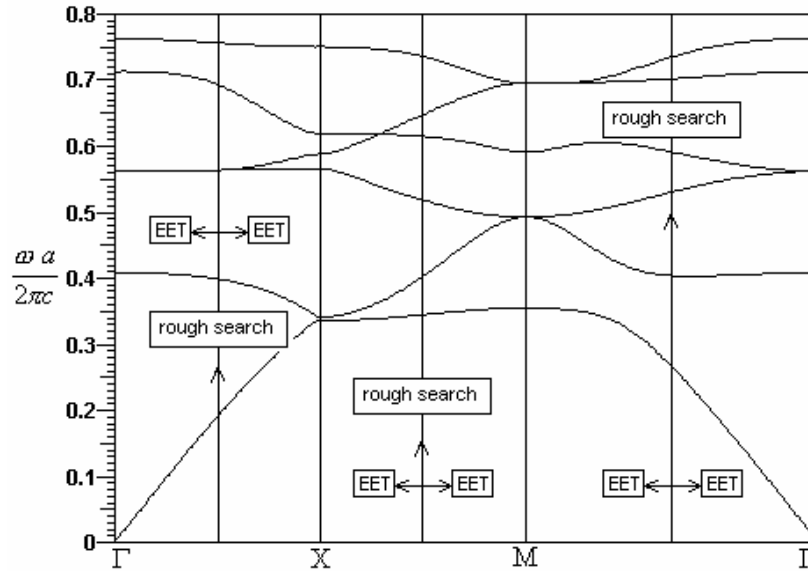


Fig. 5: The band diagram of the photonic crystal with dielectric rods on a square lattice (for H-polarization). The algorithms used within the eigenvalue search procedure are labeled correspondingly.

Having defined the original cell and its periodic boundary conditions, one has to set up the MMP model of the scattering body in the lattice point: We approximate the field in each domain by a superposition of multipole expansions and sometimes by additional, analytic solutions of Maxwell's equations (in the frequency domain). The amplitudes or parameters of the resulting series expansions are then computed with the generalized point matching technique, i.e., by minimizing a weighted error function defined along all natural and fictitious boundaries. For example, for the simple geometry in Fig. 4 we use the following expansions:

$$E_z = \sum_{n=0}^N A_n^E J_n(\kappa r) \cos(n\varphi) + B_n^E J_n(\kappa r) \sin(n\varphi) \quad (6)$$

$$H_z = \sum_{n=0}^N A_n^H J_n(\kappa r) \cos(n\varphi) + B_n^H J_n(\kappa r) \sin(n\varphi) \quad (7)$$

$$E_z = \sum_{n=0}^N C_n^E H_n^1(\kappa r) \cos(n\varphi) + D_n^E H_n^1(\kappa r) \sin(n\varphi) \quad (8)$$

$$H_z = \sum_{n=0}^N C_n^H H_n^1(\kappa r) \cos(n\varphi) + D_n^H H_n^1(\kappa r) \sin(n\varphi) \quad (9)$$

where  $J_n$  is Bessel function of order  $n$ ,  $H_n^1$  is Hankel function of first kind and order  $n$ ,  $\kappa$  is transverse propagation constant and  $(r, \varphi)$  are polar coordinates with respect to the origin at the position of the corresponding expansion. Expansion (6) (Bessel expansion) is used in the case of E-polarization and expansion (7) is used in the case of H-polarization. These Bessel expansions are used for the domain inside of the dielectric rod because these functions have no singularity at origin. Furthermore, these expansions are sufficient because the domain is simply connected. The background domain is not simply connected, because it contains a hole. Therefore,

we need at least two different expansions, namely a multipole expansion (8) or (9) and Bessel expansion (6) or (7). Note that the multipole expansion essentially accounts for the field scattered at the inner boundary, whereas the Bessel expansion accounts for the outer, fictitious boundaries. This means that the Bessel expansion simulates the field that comes from all rods outside the original cell. According to Vekua [24], our set of expansions is complete in the sense that the error of the field is below an arbitrarily small value  $\varepsilon$  provided that the highest orders are big enough and provided that the amplitudes ( $A, B, C, D$  in (6)-(9)) are computed correctly.

#### IV. THE MMP-MAS EIGENVALUE SOLVER

For obtaining the band diagram of a PhC, it is necessary to solve an eigenvalue problem, because there is no excitation like in scattering problems. This means that we only obtain non-trivial solutions (i.e. frequencies) for an arbitrary point of the IBZ (i.e., for a given set of complex values  $C_1, C_2$ ). Thus, we essentially have a periodic resonator problem to solve. The search of resonance frequencies in the MMP code MaX-1 is somehow different from many other numerical methods because MMP uses a full rectangular system matrix obtained from the generalized point matching technique. For such type of matrix it is very demanding to obtain accurate results while avoiding problems with the condition number [25]. Note that condition number problems are especially crucial when one is solving eigenvalue problems. If this is not properly done, one can obtain a "noisy" behavior near the eigenvalues and this can heavily disturb the numerical eigenvalue search procedures. However, the standard MMP eigenvalue search procedure first defines a real valued, positive eigenvalue search function

$$\eta(e) = \frac{\|E(e)\|^2}{A^2(e)} \quad (10)$$

where  $e$  is the eigenvalue (i.e. the resonance frequency),  $E$  is the weighted residual, and  $A$  is an amplitude that may be retrieved from any field component in a specific test point (or an integral over some field profile). For the band gap computation, it is most reasonable to define  $A^2$  as the total electromagnetic energy within the original cell. According to (10) the desired eigenvalues are characterized by the minima of the search function  $\eta$ . Analyzing the shape of  $\eta$  near the minima provides additional information on the accuracy of the solution.

Although more reliable results are obtained when the

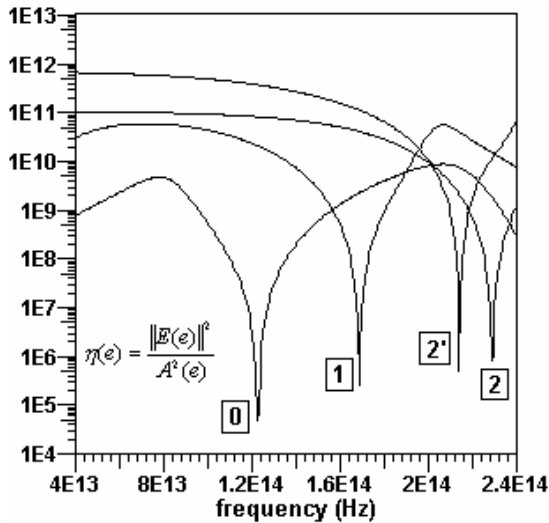


Fig. 6: The behavior of the eigenvalue search function (in the  $\Gamma$  point) of one single model with four different "last" expansions (the order of the last expansion is labelled in the figure)

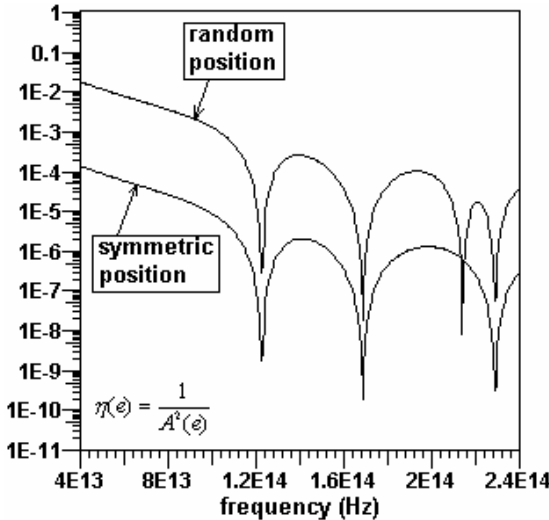


Fig. 7: The behavior of the eigenvalue search function (for a  $k$ -vector in the  $\Gamma$  point) using the fictitious excitation in a random and symmetric position respectively.

amplitude is defined by an appropriate integral, the definition in one or a few test points is sufficient for most cases. Since the numerical intergration may be time-consuming, one usually prefers the simpler test point method. However, it is important to note that the definition of the search function is not unique. By defining different search functions, one can gain even more intrinsic information providing a good error estimation and for validation purposes. As depicted in Fig. 6, even for a single model (fixed amplitude definition and fixed multipole expansion), one can address the different minima of the same eigenvalue search functions simply by rearranging the columns of the MMP matrix. In fact, in the Givens update algorithm [25], which was used for solving the MMP matrix equation, the last expansion somehow plays the role of an excitation. When it happens that the spatial symmetry of such excitation is not contained in the symmetry of the searched eigenmode, this mode will not be "excited", hence, the corresponding minimum of the eigen-value search function is suppressed. Although, it may be desirable to suppress some modes in applications where not all modes must be considered, this is usually inconvenient for the automatic computation of the complete band structure. We therefore look for an alternative technique.

Remember that we have introduced fictitious boundaries for handling the periodic problem. Similarly, we now can introduce a fictitious excitation that is defined in such a way that all modes are excited (Fig. 7). This concept mimics the measurement of resonance frequencies, where one always needs an excitation of the resonator and a test point (or port) where the signal is measured. By sweeping the frequency of the excitation, the peaks of the amplitude  $A$  in the test point can be readily assigned to the resonance frequencies of the different modes. This procedure was first introduced by the Method of Auxiliary Sources (MAS) [26] and a similar method was used by Sakoda [27]. Finally, the method was adapted to MMP by Moreno [28]. MAS uses eigenvalue

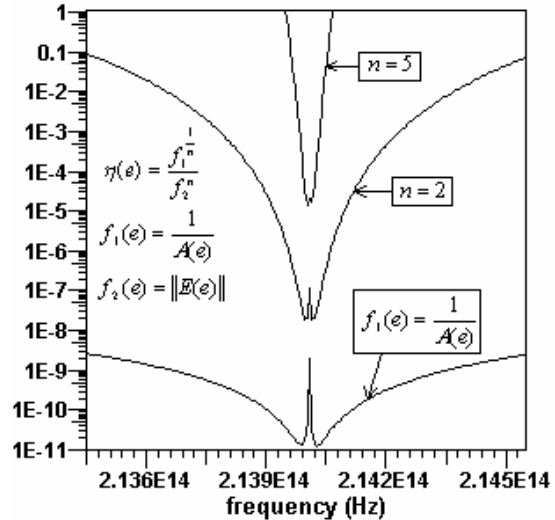


Fig. 8: The "twin minima" phenomenon, behavior of the eigenvalue search function within the eigenvalue search procedure using a randomly located fictitious excitation.

search functions  $\mu$  such as the energy density  $A^2$  at the test point are used. The eigenvalues are then obtained from the maxima of  $\mu$ . The analysis of  $\mu$  near the maxima has yielded a strange "double peak" phenomenon that disturbs the numerical search procedure. The standard MMP-MAS eigenvalue solver searches for minima of the eigenvalue search function  $\eta = 1/\mu = 1/A^2$ , i.e., one obtains "twin minima" instead of double peaks, as shown in Fig. 8. The "double peak" phenomenon and the "twin minima" are caused by a very sharp peak of the residual  $E$  at the correct eigenvalue position. Note that this peak is not obtained in the standard MMP approach without fictitious excitations. Of course, the residual peak may also be used for defining the eigenvalues. Since these peaks are extremely sharp, it is very likely that one of the eigenvalues is missed by the rough search routine that searches for all eigenvalues. In order to overcome these problems, one can define more complicated eigenvalue search functions  $\eta$  as proposed in Fig. 8. This allows one to suppress the double peak phenomenon. Unfortunately, one may encounter numerical underflow problems in some applications. Therefore, the current MaX-1 eigenvalue solvers

uses three different "competing" eigenvalue search functions: 1) A complicated one with user-definable exponent  $n$ , 2) the inverse of the amplitude, and 3) the proper residual. Using all of these three functions, the code is capable to detect the correct locations of the eigenvalues. An alternative to overcome the twin minima problems is the introduction of "fictitious losses" that smoothen the resulting search function  $\eta$ .

Since one often considers a broad frequency range, it is not reasonable to find the eigenvalues by plotting the eigenvalue search function over the entire range with a very high resolution. It is much more efficient to subdivide the search process into two steps: 1) Rough detection of all eigenvalues and 2) fine search, i.e., accurate computation of the eigenvalues. The first step seems to be trivial as soon as the problems mentioned above have been solved. The second step requires a fast minimum search procedure for real functions. The algorithm used in MaX-1 is mainly based on a parabolic interpolation because the search function near the minima is usually almost parabolic – provided that the double peak phenomenon has been removed.

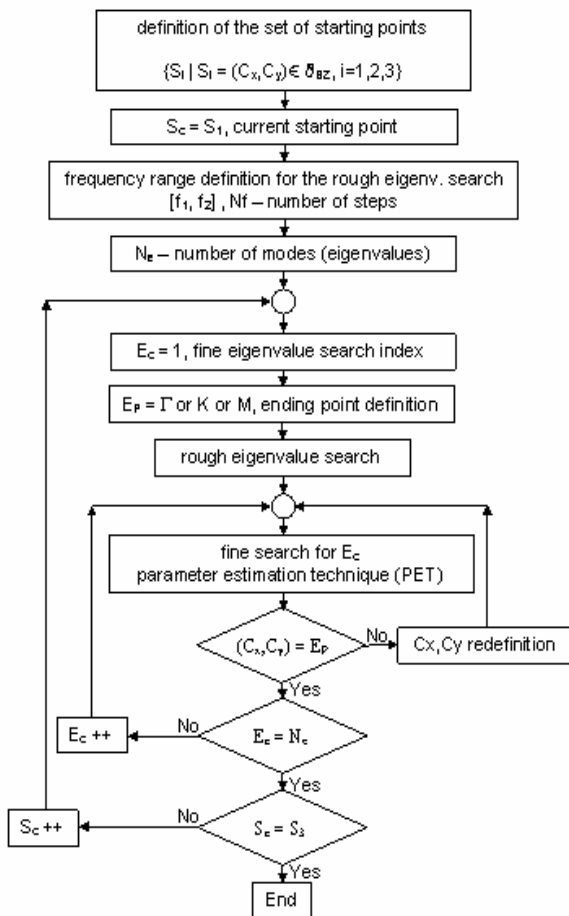


Fig. 9: The algorithm for the band structure computation using MMP.

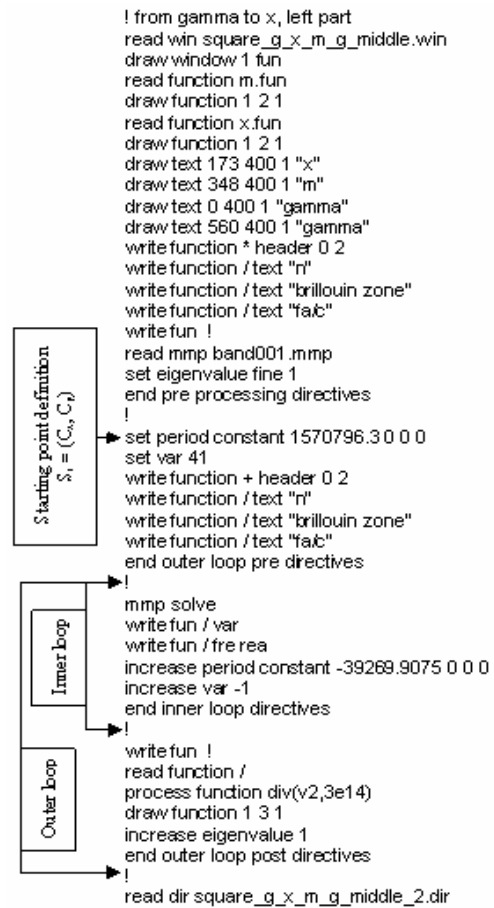


Fig. 10: The algorithm for band diagram computation written in the MaX-1 script language.



TABLE I  
CONVERGENCE CHARACTERISTICS, COMPUTATION FOR 1<sup>ST</sup> AND 6<sup>TH</sup> EIGENFREQUENCY AT X POINT OF IBZ

Number of unknowns	Eigenfrequency 1			Eigenfrequency 6		
	Frequency (Hz)	Error (%)	Field mismatch. (%)	Frequency (Hz)	Error (%)	Field mismatch. (%)
20	1.0223585e14	1.473	9.620748e-0	2.3465308e14	4.194	2.306028e+1
36	1.0095955e14	0.206	4.204639e-0	2.2567438e14	0.207	4.449937e+0
52	1.0078338e14	0.032	0.288115e-0	2.2512072e14	0.039	0.824365e-0
94	1.0074678e14	0.005	4.465747e-2	2.2519421e14	0.006	0.128581e-0
164	1.0075153e14	0.000	4.729721e-7	2.2520785e14	0.000	3.551224e-6

Having a closer look to typical band diagrams (Fig. 3), we see different situations which can cause problems for both the rough search and the fine search. Mainly at the  $\Gamma$  and the M point we usually observe degenerate modes. Furthermore, we have areas with almost degenerate modes and points where different lines seem to cross each other, where the modes are (accidentally) degenerated. When the rough search is performed to degenerate points, it usually cannot detect all modes involved. Even if the search procedure is started in a close vicinity to such degeneracies, it will be too time-consuming to iterate into all eigenmodes. In order to overcome these problems, it is reasonable to start a rough search in a domain where all eigenvalues could be easily tracked down (e.g. the interval between  $\Gamma$  and X in the band diagram of Fig. 5). Once this has been done, one can trace each eigenvalue by moving a small step either to the left or right side within the band diagram, and repeating this

procedure until the border of the diagram is reached. For each such step, only a fine search must be performed. Depending on 1) the desired accuracy, 2) the step size, and 3) special properties of the model, several iterations are required. The number of iterations could be drastically reduced when using the Eigenvalue Estimation Technique (EET) implemented in MaX-1 [19]. This technique uses the information of previous eigenvalue solutions for the extrapolation of the current eigenvalue's search interval. Typically, 4–12 iterations per step are sufficient for obtaining an eigenvalue with a high precision. For example, for tracing the first mode in Fig. 3, 280 search steps were performed and 5 iterations per step were required in the average.

V. AUTOMATIC EIGENVALUE SEARCH

Referring to e.g. Fig. 5 a standard band diagram consists of three different intervals corresponding to the three sides of

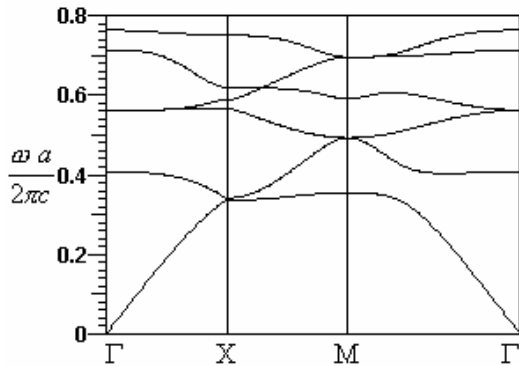


Fig. 11: The band diagram of the photonic crystal with dielectric rods and square lattice, H-polarization, the first 6 modes.

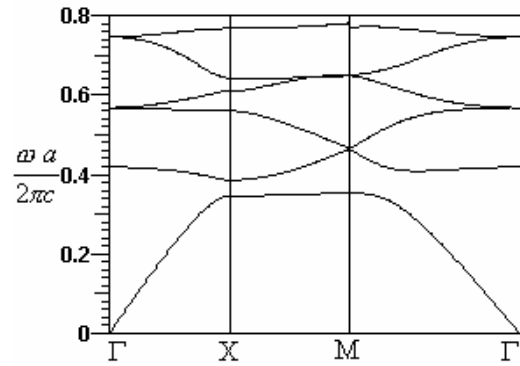


Fig. 13: The band diagram of the photonic crystal with dielectric rods and hexagonal lattice, H-polarization, the first 6 modes.

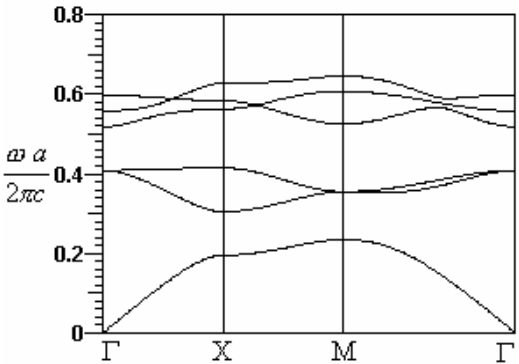


Fig. 12: The band diagram of the photonic crystal with dielectric rods and square lattice, E-polarization, the first 6 modes.

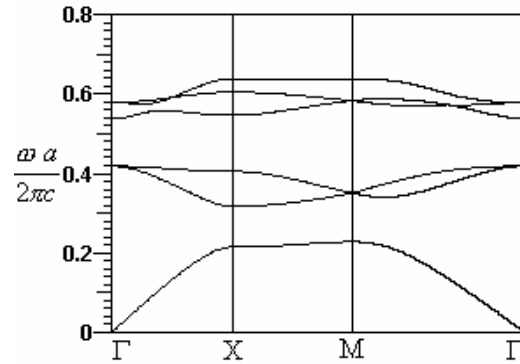


Fig. 14: The band diagram of the photonic crystal with dielectric rods and hexagonal lattice, E-polarization, the first 6 modes.

the IBZ. When the rough search is started somewhere in the middle of such an interval (e.g. in the area between  $\Gamma$  and X in the band diagram), it must be repeated three times. After each rough search the fine search must be repeated for each obtained eigenvalue and, finally, the fine search routine must run for each eigenvalue once towards the left and once towards the right side of the band diagram, as depicted in Fig. 5. MaX-1 contains a script language that allows one to define complicated procedures such as the search procedure mentioned above. The set of MaX-1 directives for the automatic generation of a band diagram from the point in the middle between  $\Gamma$  and X to the  $\Gamma$  point, is given in Fig. 10, and the complete algorithm for this procedure is given in Fig. 9. It is obvious that the algorithm is not simple and the overall procedure relies on fast computer resources.

## VI. NUMERICAL VERIFICATION

We have applied MMP to various PhC lattices. Internal tests show excellent convergence. Therefore high accuracy may easily be obtained. Table I shows the MMP estimate of the mismatching errors along the boundary for the model outlined in Fig. 3 with different maximum orders of the multipoles and Bessel expansions, i.e., with different numbers of unknowns. Note that the computation time typically is proportional to the cube of the number of unknowns because we use a brute-force full matrix solver (Givens update scheme). Despite of this, the computation time remains reasonably short because the matrices obviously are much smaller than the matrices used in other methods. For example Fig. 11 was obtained with 3 rough-search routines, 100 frequency steps each. The total number of 1656 plotted points required were then computed with 8280 MMP evaluations of  $\eta$ , i.e. approximately 5 iterations per point in the diagram were performed. The total calculation time was 40 minutes on a Pentium 4, 2GHz. Because of the excellent convergence, we also can estimate the accuracy of the eigenvalues by comparing them with a very accurate MMP model. As one can see from Table I, one only obtains one more digit when doubling the number of unknowns.

In order to validate this algorithm, several calculations were performed and results were compared with the results of MPB package developed at the MIT [29]. For the PhC with square lattice and dielectric rods (Fig. 3), a band diagram calculation was performed for different field polarizations and the results are given in Fig. 11 (H-polarization) and Fig. 12 (E-polarization). The results for the hexagonal lattice case (Fig. 4), are depicted in Fig. 13 (H-polarization) and Fig. 14 (E-polarization). These two types of PhC rely on the same lattice data: A dielectric rod with radius  $r=0.3a$  and a dielectric constant of  $\epsilon=11.56$ , the lattice is embedded in air and the lattice constant is  $a=10^{-6}(m)$ . From Figs. 11–14 we deduce a perfect agreement with the MPB results documented in [29].

## VII. CONCLUSION

We have presented an efficient method for band structure calculation for 2D dielectric PhCs. In this framework a fully

automatic algorithm was developed and evaluated along several examples. The eigenvalue searching procedure in the frequency domain has been performed using a fictitious excitation. Optimal eigenvalue search functions have been found while evaluating the total eigenvalue spectrum for  $k$ -values at three preferable points on the IBZ. The three resulting sets of eigenvalues are evolved into a full band diagram using a highly efficient Eigenvalue Estimation Technique (EET). The overall algorithm performs photonic band diagram calculations at a very high level of accuracy and at reasonable computational costs. This algorithm is easily extendable for applications involving localized defect mode analysis [30], various PhC defect waveguide types (supercell approach [31]) and photonic waveguide discontinuities [31], as well.

## ACKNOWLEDGMENT

This work was supported by the Swiss National Science Foundation in the framework of the project NFP-2000-065102.01/1 and the research initiative NCCR Quantum Photonics.

## REFERENCES

- [1] E. Yablanovich, "Inhibited spontaneous emission in solid-state physics and electronics", *Phys. Rev. Lett.*, **58**, pp. 2059-2062, 1987.
- [2] J. Mills, "Photonic crystals head toward the marketplace", Nov. 2002, <http://optics.org/articles/ole/7/11/1/1>.
- [3] K. Busch, S. John, "Liquid-crystal photonic-band-gap materials: the tunable electromagnetic vacuum", *Phys. Rev. Letters*, **83**, pp. 967-970, 1990.
- [4] A. Figotin, Y. A. Godin, "two-dimensional tunable photonic crystals", *Phys. Rev. B*, **57**, pp. 2841-2848, 1998.
- [5] R. L. Sutherland, V. P. Tondiglia, L. V. Natarajan, S. Chandra, "Switchable orthorhombic F photonic crystals formed by holographic polymerization-induced phase separation of liquid crystal", *Optics Express*, **10**, pp. 1074-1082, 2002.
- [6] K. Sakoda, "Optical Properties of Photonic Crystals", Springer, Berlin, 2001.
- [7] J. D. Joannopoulos, R. D. Meade, J. N. Winn, "Molding the Flow of Light", Princeton University Press, 1995.
- [8] K. M. Ho, C. T. Chan, and C. M. Soukoulis, "Existence of a Photonic Gap in Periodic Dielectric Structures", *Phys. Rev. Lett.*, **65**, pp. 3152-3155, 1990.
- [9] S. G. Johnson, and J. D. Joannopoulos, "Block-iterative frequency-domain methods for Maxwell's equations in a planewave basis", *Opt. Express*, **8**, pp. 173-190, 2001.
- [10] R. D. Meade, A. M. Rappe, K. D. Brommer, J. D. Joannopoulos, and O. L. Alerhand, "Accurate theoretical analysis of photonic band-gap materials", *Phys. Rev. B*, **48**, pp. 8434-8437, 1993.
- [11] H. S. Sözüer, J. W. Haus, and R. Inguva, "Photonic bands: Convergence problems with the plane-wave method", *Phys. Rev. B*, **45**, pp. 13962-13972, 1992.
- [12] D. Hermann, M. Frank, K. Busch and P. Wölffe, "Photonic band structure computations", *Opt. Express*, **8**, pp. 167-172, 2001.
- [13] K. Ohtaka, T. Ueta, and K. Amemiya, "Calculation of photonic bands using vector cylindrical waves and reflectivity of light for an array of dielectric rods", *Phys. Rev B*, **57**, pp. 2550-2568, 1998.
- [14] C. T. Chan, Q. L. Yu, and K. M. Ho, "Order-N spectral method for electromagnetic waves", *Phys. Rev B*, **51**, pp. 16 635-16 642, 1995.
- [15] M. Qui and S. He, "A non-orthogonal finite-difference time-domain method for computing the band structure of a two-dimensional photonic crystal with dielectric and metallic inclusions", *J. Appl. Phys.*, **87**, pp. 8268-8275, 2000.
- [16] J. B. Pendry and A. MacKinnon, "Calculation of Photon Dispersion Relations", *Phys. Rev. Lett.*, **69**, pp. 2772-2775, 1992.
- [17] W. Axmann and P. Kuchment, "An efficient finite element method for computing spectra of photonic and acoustic band-gap materials", *J. Comput. Phys.*, **150**, pp. 468-481, 1999.

- [18] P. A. Knipp, and T. L. Reinecke, "Boundary-element calculations of electromagnetic band-structure of photonic crystals", *Physica E*, **2**, pp. 920-924, 1998.
- [19] Ch. Hafner, "Post-modern Electromagnetics Using Intelligent Maxwell Solvers", John Wiley & Sons, 1999.
- [20] Ch. Hafner, "MaX-1: A visual electromagnetics platform", John Wiley & Sons, 1998.
- [21] P. R. Villeneuve and M. Piche, "Photonic band gaps in two-dimensional square and hexagonal lattices", *Phys. Rev. B*, **46**, pp. 4969-4972, 1992.
- [22] M. Plihal and A. A. Maradudin, "Photonic band structure of two-dimensional systems: the triangular lattice", *Phys. Rev. B*, **44**, pp. 8565-8571, 1991.
- [23] Ch. Hafner, J. Smajic, The Computational Optics Group Web Page (IFH, ETH Zurich), <http://alphard.ethz.ch/>.
- [24] I. N. Vekua, "New methods for solving elliptic equations", North-Holland, Amsterdam, 1967.
- [25] G. H. Golub and C. F. Van Loan, "Matrix Computations", John Hopkins University Press, Baltimore, 1996.
- [26] F. G. Bogdanov, D. D. Karkashadze, and R. S. Zaridze, in "Generalized Multipole Techniques for Electromagnetic and Light Scattering", edited by T. Wriedt, pp. 143-172, Elsevier, Amsterdam, 1999.
- [27] K. Sakoda, N. Kawai, T. Ito, A. Chutinan, S. Noda, T. Mitsuyui, and K. Hirao, "Photonic bands of metallic systems. I. Principle of calculation and accuracy", *Phys. Rev. B*, **64**, pp. 045116, 2001.
- [28] E. Moreno, D. Erni and Ch. Hafner, "Band structure computations of metallic photonic crystals with the multiple multipole method", *Phys. Rev. B*, **65**, pp. 155120: 1-10, 2002.
- [29] S. G. Johnson and J. D. Joannopoulos, The MIT Photonic-Bands Package home page, <http://ab-initio.mit.edu/mpb/>.
- [30] R. D. Meade, K. D. Brommer, A. M. Rappe and J. D. Joannopoulos, "Photonic band states in periodic dielectric materials", *Phys. Rev. B*, **44**, pp. 13 772 - 13 774, 1991.
- [31] E. Moreno, D. Erni and Ch. Hafner, "Modeling of discontinuities in photonic crystal waveguides with the multiple multipole method", *Phys. Rev. B*, **66**, pp. 036618, 2002.



**Jasmin Smajic** was born in Tuzla, Bosnia and Herzegovina, in 1971. He received a Dipl. El.-Ing. degree from Faculty of Electrical Engineering, Tuzla in 1996. Since 1996 he has been working at the Faculty of Electrical Engineering in Tuzla on numerical calculation of electromagnetic field, numerical mathematics and optimization. He got a M.Sc. degree in 1998 from the Faculty of Electrical Engineering and Computing in Zagreb, Croatia, for the analysis of magnetic field in non-linear material. He received a Ph.D. in 2001 from Faculty of Electrical Engineering and Computing in Zagreb, Croatia, for numerical calculation of time-varying field in non-linear material and electrical machine design optimization. Since 2002 he is a postdoctoral research fellow in the Computational Optics group of the Laboratory for Electromagnetic Fields and Microwave Electronics at the ETH Zurich. His current research interest includes numerical field calculation and design optimization of photonic crystal devices.



**Christian Hafner** was born in Zurich, Switzerland, in 1952. He received a Dipl. El.-Ing. Degree, Doctoral Degree, and Venia Legendi from Swiss Federal Institute of Technology (ETH), Zürich in 1975, 1980, and 1987 respectively. In 1999 he was given the title of Professor. Since 1976 he has been working at the ETH on the development of methods for computational electromagnetics and for optimization problems. He has developed the Multiple Multipole Program (MMP), the MaX-1 package, the Generalized Genetic Programming (GGP) code, and various optimization codes. He worked on various applications (electrostatics, EM scattering, antenna, waveguides and waveguide discontinuities, gratings, chiral media, etc.). His current focus is on photonic crystals, microstructured optical fibers, and Scanning Nearfield Optical Microscopes (SNOM). In 1990 he obtained the second prize of the Seymour Cray award for scientific computing and in 2001 he has been awarded the 2000 Outstanding Journal Paper Award by the Applied Computational Electromagnetics Society. He is member of the Electromagnetics Academy.



**Daniel Erni** was born in Lugano, Switzerland, in 1961. He received an El.-Ing. HTL degree from Interkantonales Technikum Rapperswil HTL in 1986, and a Dipl. El.-Ing. degree from Swiss Federal Institute of Technology (ETH), Zürich in 1990, both in electrical engineering. Since 1990 he has been working at the Laboratory for Electromagnetic Fields and Microwave Electronics (ETH) on nonlinear wave propagation, laser diode modeling (multi-section DFB and DBR lasers, VCSELs), computational electro-magnetics and on the design of non-periodic optical waveguide gratings e.g. by means of evolutionary algorithms.

He got a Ph.D. degree in 1996 for the investigation of non-periodic waveguide gratings and non-periodic coupled cavity laser concepts. His current research interests include highly multimode optical signal transmission in optical interconnects (i.e. in optical backplanes with extremely large waveguide cross sections) as well as alternative waveguiding concepts for dense integrated optical devices like e.g. photonic crystal devices, couplers and WDM filter structures. In 2001 he has been awarded the 2000 Outstanding Journal Paper Award by the Applied Computational Electromagnetics Society for a contribution on the application of evolutionary optimization algorithms in computational optics. Dr. Erni is the head of the Communication Photonics Group at ETH Zurich ([www.photonics.ee.ethz.ch](http://www.photonics.ee.ethz.ch)). He is also a member of the Swiss Physical Society (SPS), of the German Physical Society (DPG), of the Optical Society of America (OSA), and of the IEEE.

## Analysis of Conventional and Novel Delay Lines: A Numerical Study

Omar M. Ramahi

Mechanical Engineering Department, Electrical and Computer Engineering Department,  
and CALCE Electronic Products and Systems Center

2181 Glenn L. Martin Hall

A. James Clark School of Engineering

University of Maryland

College Park, MD 20742, U.S.A.

oramahi@calce.umd.edu

[www.enme.umd.edu/EMCPL/](http://www.enme.umd.edu/EMCPL/)

### Abstract

Delay lines are convenient circuit elements used to introduce delay between circuit board components to achieve required timing. Serpentine or meander lines are the most common of delay lines. These lines introduce delay but also introduce spurious dispersion that makes the signal appear as if it is arriving earlier than expected. The cause of such spurious speed-up or skew is analyzed qualitatively. Previous work found that owing to the periodicity inherent in the serpentine line structure, the crosstalk noise accumulates *synchronously*, thus creating a higher potential for triggering false logic. Numerical simulations are performed using the Finite-Difference Time-Domain (FDTD) method to corroborate the qualitative prediction with physical behavior. Based on the understanding of the coupling mechanism in periodic serpentine lines, a qualitative prediction can be made of the behavior of novel delay lines such as the spiral line. A new delay line, the *concentric Cs* delay lines, is introduced. The design of the new line is based on forcing the crosstalk noise to spread over time, or to accumulate *asynchronously*, thus enhancing the integrity of the received signal.

**Key Words:** Delay Lines, Serpentine Lines, Meander Lines, Spiral Lines, FDTD, Numerical Simulation, Crosstalk Noise.

### I. Introduction

It can be argued that timing problems are amongst the most serious plaguing high-speed digital circuit-board design. As the clock speed increases, the wavelength shrinks. For instance, for a clock speed of 1.5 GHz, the pulse harmonics containing sufficient energy reach beyond 10 GHz, making a typical motherboard or daughter cards electrically

large. As a consequence, a delay line used to introduce precise delay (based on the length of the line and board material) between circuit board elements can no longer be considered to have TEM or quasi-TEM propagation behavior, and to be electromagnetically isolated from neighboring lines that fall within its proximity. With the timing budget shrinking to the picosecond regime, any non-predictable behavior of delay lines can potentially cause a timing imbalance at the receiver end.

Two mechanisms are employed to achieve required signal delay between circuit components. The first is achieved through internal electronic circuitry. The second mechanism, which is the most common and least expensive, is achieved through meandering a transmission line as shown in Fig. 1. The meandered line, commonly referred to as the serpentine line, consists of a number of closely packed transmission line segments. The only objective from meandering the line is to achieve high density (of transmission line) per square inch of circuit board while obtaining signal delay that is directly proportional to the length of the line.

When serpentine lines are used in high-speed digital circuit applications, the time delay through a single serpentine line can be much longer than the rise time of the signal pulse. Under such conditions, serpentine lines have been found to introduce a dispersion that makes the signal *appear* as if it is arriving earlier than would be expected based on the exact electrical length of the line [1]. This spurious speed-up in the signal can be characterized as a type of dispersion. This dispersion is primarily caused by the topology of the line and is directly related to the crosstalk between the adjacent transmission line sections. More specifically, the dispersion is related to two fundamental geometrical parameters: the first

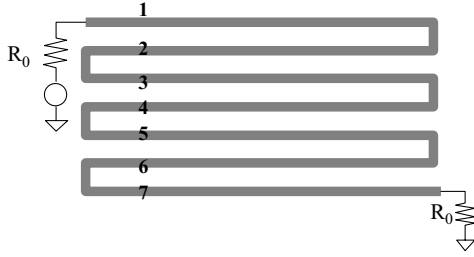


Fig. 1. A matched seven-section serpentine delay line. The Characteristic impedance of each identical section is  $R_0$ .

is the length of each serpentine section, and the second is the spacing between adjacent sections, which influences the capacitive and inductive coupling [1], [2].

Based on these findings, Wu and Chao introduced the flat spiral delay line to force the crosstalk noise to accumulate *asynchronously* [3]. The flat spiral line is distinguished from the classical spiral delay line, which requires three-dimensional topology and therefore cannot be printed on a single board layer. In this work, the flat spiral line will be referred to as the spiral line.

The spiral delay line is considered a significant improvement over the serpentine line. In [3], the motivation behind the spiral line was introduced and analysis was given based on the wave-tracing technique which did not take into account higher-order mode coupling and corner effects. Also in [3], quantitative analysis was also performed to include the effects of multiple and feedback couplings between lines. To incorporate high-order effects into the modeling of serpentine line, especially the coupling between the non-orthogonal lines, the three-dimensional Finite-Difference Time-Domain (FDTD) method was used to analyze serpentine and spiral lines [4]. In a subsequent work, the FDTD method was used to analyze the spiral line for Gaussian pulse excitation [5]. More recently, the Method of Moments (MoM) was used to present a full-wave model for the serpentine line including physical losses [6].

In this work, we use the same qualitative wave-tracing methodology that was adopted in [2] to analyze the spiral line. We show that the wave-tracing methodology can only give qualitative analysis of the line and that a full-wave model is needed to accommodate the effect of corners and

coupling between non-orthogonal segments. We use the FDTD method to analyze the spiral line and show that more inclusive performance can be predicted. Based on the qualitative insight gained from the analysis of the serpentine and spiral line, we introduce a new delay line that we refer to as the *concentric Cs* delay line. Qualitative analysis of the new lines is given followed by full-wave three-dimensional simulation.

The organization of this paper is as follows. In section 2, the mechanism of coupling between two transmission lines is introduced with application to serpentine lines. Sections 3 and 4 present a qualitative analysis followed by full-wave numerical simulation of practical real-world structures for the serpentine and spiral lines, respectively. Section 5 introduces the Concentric Cs delay lines. We note that the FDTD method will be used purely as a numerical simulation tool without giving details of the simulation parameters involved such as the cell size and time step, ...etc. The paper concludes with critical observations that can be used in the design of predictable-delay lines.

## II. Weak Coupling Crosstalk

### a. Analysis

A typical serpentine delay line is composed of transmission line sections closely packed as shown in Fig. 1. Let us isolate two adjacent sections as shown in Fig. 2. After examination, we notice that the two isolated sections resemble the simplest case of two parallel transmission lines [2]. After ignoring higher-order effects, the two-segment serpentine line shown in Fig.2 is equivalent to the two transmission lines matched at both ends and shown in Fig. 3. Once this observation is made, using conventional transmission line analysis, one can predict the crosstalk induced on the second line due to the launched signal on the first line.

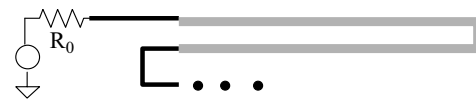


Fig. 2. Segment of a serpentine line.

Considering Fig. 3, the near-end crosstalk, shown as voltage  $V_2$ , is proportional to the mutual capacitance and mutual inductance characterizing the two lines. The coupling coefficient  $k_{NE}$  is given by

$$k_{NE} = \frac{1}{4} \left\{ \frac{|C_{12}|}{C_{22}} + \frac{L_{12}}{L_{22}} \right\} \quad (1)$$

where the crosstalk at the near end is given by

$$V_{NE}(t) = k_{NE} [V_A(t) - V_A(t - 2t_d)] \quad (2)$$

where  $C_{11}$  and  $L_{11}$  are the self capacitance and self inductance, respectively, of the lines, and  $C_{12}$  and  $L_{12}$  are the mutual capacitance and mutual inductance, respectively, of the coupled lines [1]. Let us assume that the rise time is smaller than the line delay,  $t_d$ . If a step function is launched on line 1, then the crosstalk at the near end of line 2 will be a pulse with a duration twice the line delay (i.e., equivalent to the round-trip time  $t_d$ ). The crosstalk at the far end has a much smaller duration and it equals zero when the capacitive and inductive coupling coefficients are equal (as in the case when the medium is homogeneous as in strip lines) [1]-[2]. Since the pulse on the active line propagates to the right, the voltage at the near end of the passive line is in effect due to a leftward propagating wave. Similarly, the voltage at the far end of the passive line is the accumulation of a rightward propagating wave (which is zero in the case of homogeneous medium).

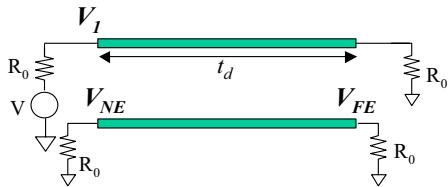


Fig. 3. Parallel transmission lines with matched terminations. A pulse transmitted on the upper line generates crosstalk on the lower line that propagates in a manner equivalent to the case of the serpentine line segment shown in Fig. 2.

If line 1, in Fig. 3, is excited by a pulse starting at  $t = t_0$  and of duration  $T$  assumed to be shorter than the length of the line  $t_d$ , then the near-end crosstalk will consist of two opposite polarity pulses separated by  $2t_d - T$ , and each of duration  $T$ . This can be shown using the principle of superposition. By decomposing the finite duration input pulse into two opposite polarity step functions separated by  $T$ , the near-end crosstalk will be the sum of two pulses. The first pulse will have positive polarity and is excited at time  $t_0$ . The second pulse will have negative polarity and will start at time  $t_0 + T$ . The sum of the two pulses yields a waveform consisting of two pulses, each of duration  $T$  and separated by a time interval of width  $2t_d - T$ .

To demonstrate these two scenarios, we use the FDTD method to simulate the behavior of two parallel strip lines (similar topology to Fig. 3) with cross section shown in Fig. 4.

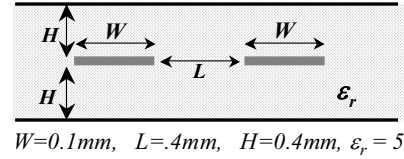


Fig. 4. Strip line cross section.

Figure 5 shows the near-end voltages on the active and passive lines when the excitation is a step function. The far-end voltage at the active line is also shown in Fig. 5. One can observe that the duration of the near-end crosstalk is  $T$ .

Figure 6(a) shows the near-end voltage on the active and passive lines when the excitation is a pulse of duration 250 picoseconds. We observe that the near-end passive line experiences two opposite polarity pulses, each of the same duration as the original pulse. This performance is in full agreement with our earlier prediction. For completion, we show the far-end voltage on the active and passive lines in Fig. 6(b). Notice that the bump appearing in Fig. 5 is due primarily to the numerical dispersion of the FDTD method and the physical dispersion caused by the propagation in the strip line configuration.

When forming a serpentine line by closely connecting identical transmission line sections, a similar crosstalk mechanism to that discussed above takes effect, except now one should also account for coupling between non-orthogonal lines and the coupling between orthogonal line segments. Let us consider the serpentine line composed of seven transmission line segments (shown in Fig. 1). Suppose  $V_{in}$  is a step voltage with a magnitude of one volt.

Once this voltage waveform is launched at the transmitter end, a voltage of magnitude  $1/2$  appears on line 1. The voltage at line 1 will induce leftward traveling waves at the near ends of lines 2, 4 and 6. These signals continue to travel on lines 3, 5 and 7 respectively. Notice that the launched signal does not excite any forward propagating waves on any of the lines as per the discussion given above. (Throughout this work, forward propagating cross talk refers to crosstalk propagating towards the receiver. Similarly,

“backward propagating crosstalk refers to crosstalk propagating towards the source.)

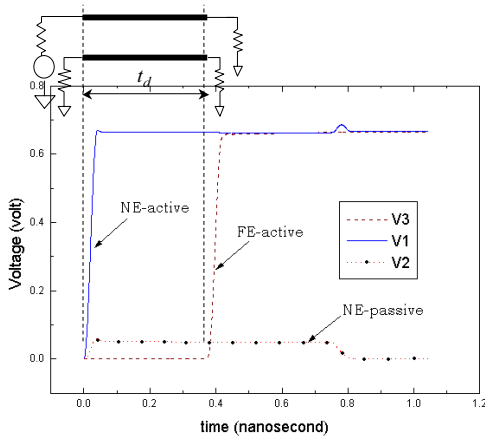


Fig. 5. Wave forms on the active and passive lines due to a step function excitation. V1 is the input pulse at the active line, V2 is the near-end voltage at the passive line, and V3 is the far-end voltage at the active line.

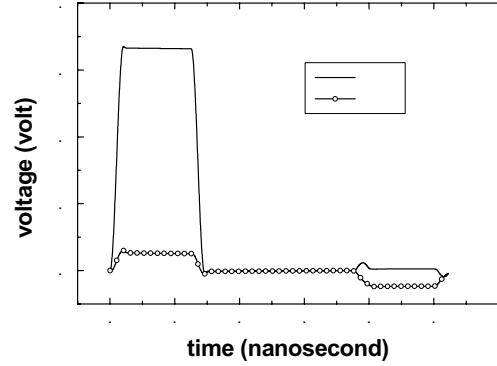
Assuming that multiple coupling is negligible (multiple coupling refers to the feedback crosstalk between lines), equation (1) can be used to find the magnitudes of the crosstalk induced on any line by the main signal as it propagates on any other line. The coupling between any two lines  $m$  and  $n$ , where  $m \neq n$ , can be written as

$$k_{|m-n|} = \frac{1}{4} \left\{ \frac{|C_{mn}|}{C_{mm}} + \frac{L_{mn}}{L_{mm}} \right\} \quad (3)$$

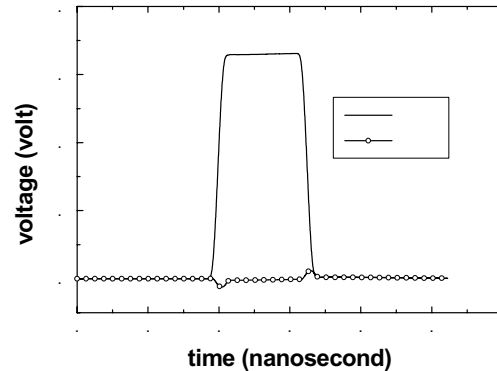
where  $C_{mm}$  and  $L_{mm}$  are the self capacitance and self inductance, respectively, of line  $m$ , and  $C_{mn}$  and  $L_{mn}$  are the mutual capacitance and mutual inductance, respectively, of the coupled lines  $m$  and  $n$ . Let us assume that the rise time is much smaller than the pulse width. Let us consider the leftward traveling wave excited at line 2, which has a magnitude of  $k_1/2$ , and duration  $2t_d$ . Furthermore, this wave arrives at the receiver end ahead of the main signal by  $2t_d$ . Similarly, backward traveling waves will appear on lines 4 and 6 having duration of  $2t_d$  and magnitudes  $k_3/2$  and  $k_5/2$  respectively. These signals will arrive ahead of the main signal by  $4t_d$  and  $6t_d$ , respectively.

When the main signal starts to propagate along line 2, it induces forward propagating crosstalk on lines 3, 5 and 7. The magnitudes of these crosstalk signals are  $k_1/2$ ,  $k_3/2$  and  $k_5/2$ , respectively. These

signals arrive ahead of the main signal by  $2t_d$ ,  $4t_d$  and  $6t_d$ , respectively. It is important to realize that as the main signal hops from one line to the next, the crosstalk induced is additive. In other words, the crosstalk noise accumulates *synchronously*. This process of coupling continues until the main signal arrives at the receiver. In fact, by adding the effect of all induced crosstalk, the waveform obtained at the receiver end becomes a laddering waveform, where each of the ladder levels is of duration  $2t_d$ .



(a)



(b)

Fig. 6. Wave forms on the active and passive sections of a two-line system obtained using the FDTD method. (a) Near-end voltage (NE-a = Near end at active line, NE-p = Near end at passive line). (b) Far-end voltage (FE-a = Far end at active line, FE-p = Far end at passive line).

Therefore, when the seven-section serpentine line (Fig. 1) is excited with a step function starting at  $t_0$ , we can expect the receiving end waveform to have a laddering waveform. When the excitation is a finite duration pulse, then the shape of the received signal will depend on whether  $T$  is shorter or longer than the round trip  $2t_d$ . When  $T$  is longer than  $2t_d$ , the qualitative behavior of the received signal is depicted

in Fig. 7(a), showing degradation of the pulse magnitude once the main signal is received. On the other hand, when  $T$  is shorter than  $2t_d$ , the received waveform consists of a train of pulses, each of duration  $T$  and separated by  $2t_d - T$ , as shown in Fig. 7(b).

The wave tracing analysis adopted here can be further generalized to serpentine lines composed of many sections. It can be shown that for a general serpentine delay line consisting of  $2N+1$  sections, a laddering waveform is generated and it arrives before the main signal. The laddering wave includes  $N$  ladders; each ladder is of width  $2t_d$  and level  $ik_{2(N-1)+1}$  for  $i=1$  to  $N$ .

In light of the above analysis, several observations can be made:

1. The laddering wave creates the impression that the pulse is arriving earlier than intended. In reality, however, the waveform arriving at the receiver is composed of two signals: the crosstalk laddering waveform (noise) and the unadulterated signal.
2. The crosstalk accumulates *synchronously* at the receiving end. The synchronous accumulation is due to the *periodicity* of the serpentine line structure.
3. The highest level of the laddering waveform can reach several times the level of crosstalk induced between two adjacent lines. In fact, the cumulative magnitude can be higher than the level of the main signal.
4. The magnitude of each ladder is proportional to the capacitive and inductive coupling between the lines.
5. The spreading of the laddering wave, i.e., the width of each ladder, is directly proportional to the length of the serpentine line segments.
6. When the pulse duration is greater than  $2t_d$ , where  $t_d$  is the delay through one section, the cumulative effect is less pronounced, producing ladders of short duration. The net effect is that the pulse arrives at the receiving end as a dispersed wave with an apparent rise time longer than that of the original signal. In such case, the serpentine line can be interpreted as a low-pass filter.
7. When the pulse duration is smaller than  $2t_d$ , where  $t_d$  is the delay through one section, the received waveform consists of a train of pulses, each of duration  $T$  and separated by  $2t_d - T$ .

#### b. Numerical Experiments

Several assumptions were made in the wave tracing analysis presented above. These were:

1. Negligible non-adjacent line coupling.
2. The backward propagating crosstalk was assumed to be zero. In the general case of non-homogeneous media, there is some backward induced crosstalk.
3. The small transmission line segments that connect the longer sections (orthogonal sections) have been assumed to have zero delay (zero physical length).
4. Negligible multi-modal propagation.

Considering the above simplifications, the qualitative model discussed earlier serves only to give an understanding of the primary crosstalk contributors. For a more accurate prediction of the performance of the serpentine line, the three-dimensional FDTD method will be used since it fully integrates the constraints listed above.

The first design tested is that of the seven-section serpentine line discussed earlier (see Fig. 1). A cross section of two adjacent lines of this geometry is shown in Fig. 4. The total electrical length of the line is 114.6 mm (4.51 in). The length of each section is 16.6 mm (0.65 in). Figure 8 shows the signal at the receiver end. Comparison is made to the control line. (In all the experiments discussed in this paper, the control line is a straight line with electrical length equivalent to that of the delay line under examination. The length of a delay line is considered to be the length of a line that runs through the center of the line, including bends.)

Observing Fig. 8, we notice that the wave tracing analysis predicted the ladders that precede the main signal only. While such prediction is quite important, it did not account for the unexpected high signal level received after the arrival of the main signal (overshoot). Although the high level occurs beyond the logic-switching instant, nevertheless, it can have an adverse effect when the signal switches to zero as false logic could be triggered.



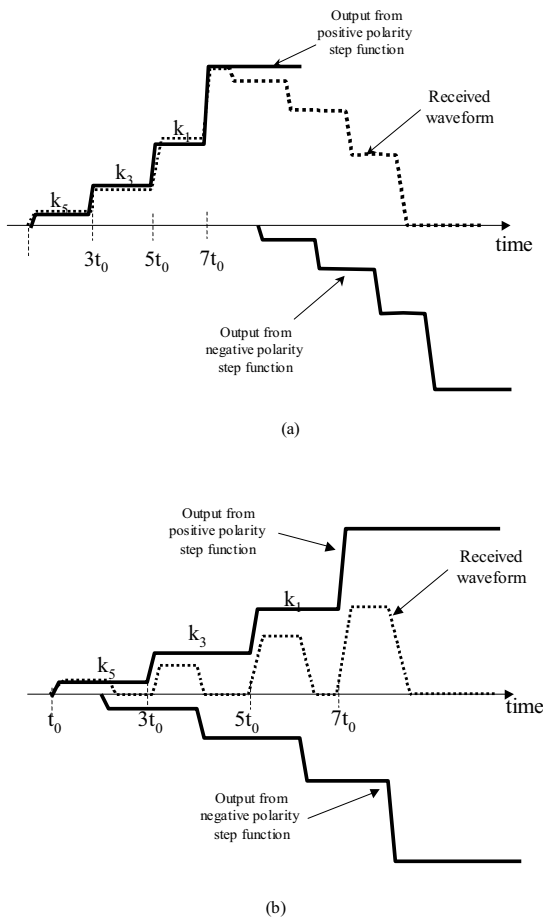


Fig. 7. Wave form at the receiving end of a serpentine line due to a pulse with a duration of  $T$ . (a)  $T > 2td$ . (b)  $T < 2td$ .

For the second test, we consider a more realistic serpentine line, where the total electrical length of the line is 405.4 mm (15.96 in). Two variations of this line are considered, as shown in Figs. 9 and 10, and will be referred to as Case A and Case B, respectively. The difference between the two topologies considered is that one has shorter sections than the other. Notice that in both cases, the lines have equivalent length, have identical line separation between adjacent segments and both topologies occupy equal board area. The excitation waveform is a pulse having a finite duration of 1.4 nanoseconds and rise time of 100 picoseconds.

Figure 11 shows the response of these two lines in comparison to the reference line. The serpentine line designated as Case B has longer sections and, consequently, its receiver signal had ladders that are

longer than Case A. However, this difference is of minor importance since the low-to-high switching occurs at approximately the same time.

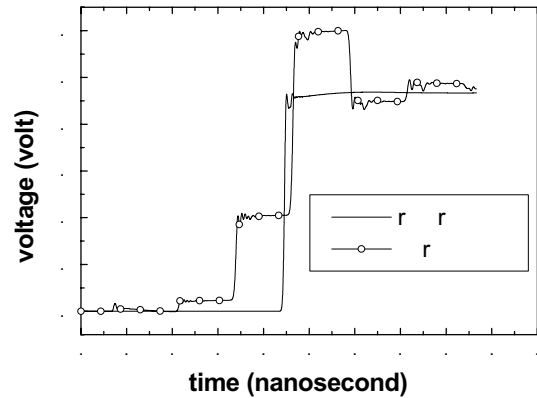


Fig. 8. Received wave form for the seven-section serpentine line.

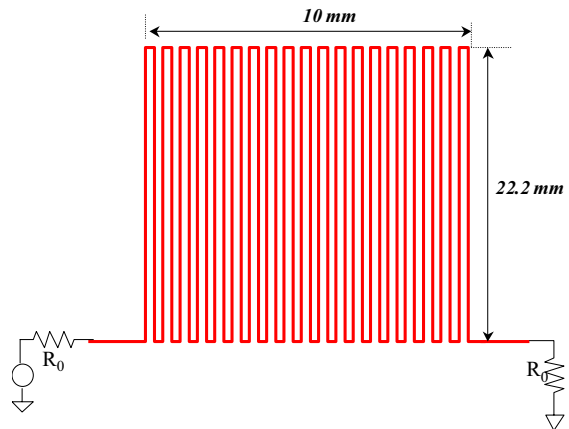


Fig. 9. 19-section serpentine line.

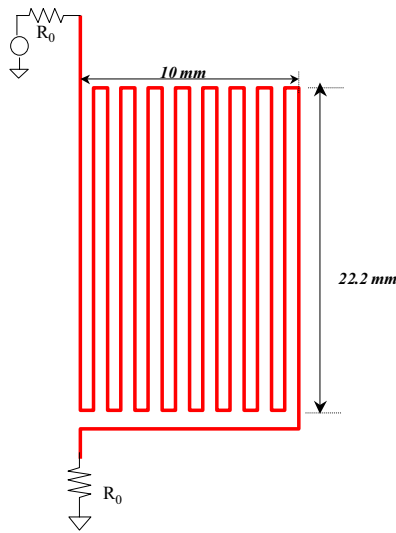


Fig. 10. 17-section serpentine line.

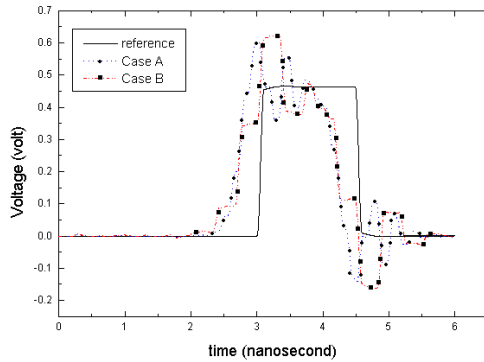


Fig. 11. Response of the 15.96 in long serpentine lines in comparison to the reference line.

### III. The Spiral Delay Line

In the serpentine line, the crosstalk was found to accumulate synchronously. This accumulation can be significant enough to trigger false logic. Ideally, this crosstalk needs to be eliminated; however, since the crosstalk is inversely proportional to the separation between the lines, the only way to eliminate or reduce the crosstalk would be to increase the separation between the lines and/or to increase the coupling between the line and the reference plane. Increasing the separation of the segments unfortunately requires larger circuit board area, which can be either expensive, or impossible in light of the density requirements. Therefore, given that for

the transmission line density (or etch density) to remain unchanged, the separation between the lines must not be changed. An alternate design, which forces the crosstalk to accumulate *asynchronously*, was proposed in [3] and is shown in Fig. 12. This alternate design, the flat spiral delay line, minimizes the periodicity in the transmission line routing as much as practicable.

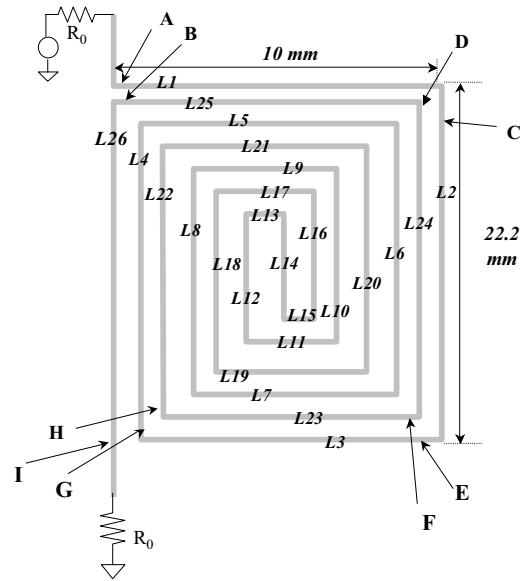


Fig. 12. Spiral delay line.

The most prominent feature of the spiral delay line is the spreading, over time, of the crosstalk noise. To demonstrate how the coupling mechanism works in the spiral line, we will initially assume that coupling between non-adjacent lines is negligible. Let us consider the line shown in Fig. 12, and let us assume that the signal arrives at point A at time  $t=0$ . Once the signal arrives at A, forward propagating crosstalk is induced at point B. This crosstalk arrives before the main signal by the time delay needed to propagate through the entire length of the line minus the segment L26. In other words, the induced forward propagating crosstalk at B arrives only after the time needed to travel the segment L26. (Henceforth, the time delay through segment LN will be denoted by  $t_{LN}$ ). So the first crosstalk induced at B by the arrival of the signal at A arrives at  $t=t_{L26}$ . When the main signal arrives at point C, forward propagating crosstalk is induced at D, arriving at the receiver at approximately  $t=t_{L1}+t_{L25}+t_{L26}$ .

Similarly, when the main signal arrives at E, it induces at point F a forward crosstalk which arrives

at the receiver at  $t = t_{L1} + t_{L2} + t_{L26} + t_{L25} + t_{L24}$ . Next, the signal arrives at G, inducing forward propagating crosstalk at H, which arrives in  $t = t_{L1} + t_{L2} + t_{L3} + t_{L26} + t_{L25} + t_{L24} + t_{L23}$ . However, the signal arriving at H will also induce forward propagating crosstalk at I. The crosstalk induced at I arrives at the receiver at  $t = t_{L1} + t_{L2} + t_{L3}$ . As the signal propagates further towards the receiver, it continues to induce crosstalk in the adjacent lines.

The above wave-tracing analysis ignores coupling between non-adjacent lines. However, even if this coupling is included, it is easy to see that the crosstalk noise will be distributive and will not accumulate synchronously. When the voltage excitation is a pulse of finite duration, the opposite polarity crosstalk induced by the trailing edge of the excitation pulse will help in reducing the final cumulative crosstalk.

To demonstrate performance of the flat spiral delay line, we construct a line with electrical length, line separation, and total board area, all equal to the serpentine lines shown in Figs. 9 and 10. The cross-section parameters are given in Fig. 4, and the rise time and pulse duration are as before (pulse width of 1.4 nanoseconds and rise time of 100 picoseconds). The dimensions of this spiral line are shown in Fig. 12.

Figure 13 shows the signal at the receiving end of the spiral line in comparison with the control line. The outstanding performance of the spiral line is clearly visible. We observe that the crosstalk noise was spread over time ahead of the main signal resulting in a high fidelity signal. In fact, for the case considered, we notice that the maximum crosstalk stays at or below 10% of the signal level, thus considerably reducing the potential for triggering false logic. We note here that slight shift between the signal due to the control line and the unadulterated signal due to the spiral line is due to a slight difference in line lengths.

The singular feature of the spiral line is its ability to spread the noise over a larger duration. A key observation is that the signal arriving at the receiving end is composed of the unadulterated pulse in addition to the asynchronous noise. This implies that the spiral line can lead to an almost perfect isolation of the accumulative noise from the unadulterated pulse.

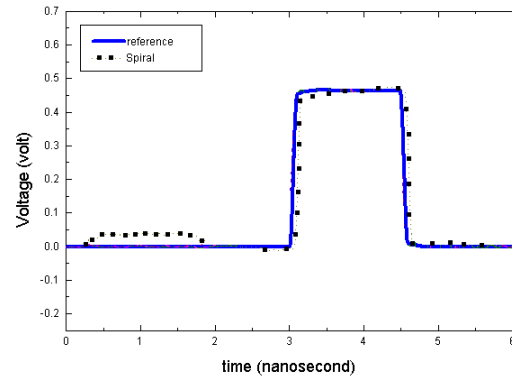


Fig. 13. Response of the 15.96 in long spiral line in comparison to the reference line.

#### IV. The Concentric Cs Delay Line

From the analysis and simulation of the spiral line, the concept of *asynchronous* coupling is emerging as a powerful mechanism to reduce the apparent dispersion of a delay line. This section introduces a novel design that exploits this mechanism of asynchronous coupling. The new delay line, shown in Fig. 14, will be referred to as the *concentric Cs* delay line. (The name concentric Cs was chosen since this new transmission line resembles different lines shaped as the letter C and centered at one location.) The design of the new line was motivated by the theme of reducing the periodicity in the topology of the structure in order to minimize the accumulative or synchronous coupling.

Using wave-tracing analysis, one can qualitatively predict the performance of the Cs line. Similar to the spiral line, the Cs line distributes the coupling over time. Consider a pulse entering the line at the beginning of section L1 (see Fig. 14). This pulse will induce a crosstalk that will precede the primary (or unadulterated) signal by a time period corresponding to the propagation over segments L1, L2, L3, L4, L5 and L6. Notice that in contrast to the spiral line, this (first-appearing) crosstalk will precede the unadulterated signal by a relatively short period, however, the topology of the Cs line prevents synchronous accumulation. One can qualitatively describe the periodicity in the Cs line structure as lying in between that of the serpentine line and the spiral line. The relative advantage of the mid-level periodicity in the structure becomes more apparent when observing the full-wave behavior as shown below.

To demonstrate the behavior of the Cs line, we design a line, equivalent in electrical length, line spacing and total board area, to the spiral and serpentine lines studied earlier. The dimensions of this design are shown in Fig. 14. Figure 15 presents the result of the FDTD simulation, under previous excitation conditions, showing the signal at the receiver end.

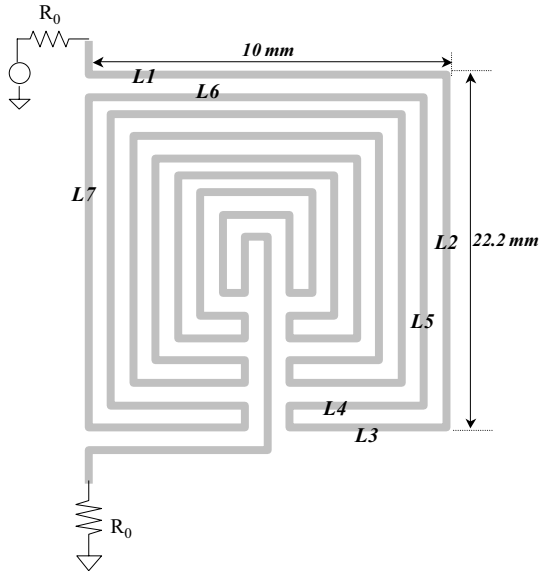


Fig. 14. The concentric Cs delay line.

Comparison is made to the spiral, serpentine and reference lines. Clearly visible from Fig. 15 is the concentration, or accumulation of the noise in the close proximity of the unadulterated signal. We further observe that, for the particular topology and line dimensions considered, that the receiver signal remains at or below 35% of the peak amplitude of the transmitted pulse.

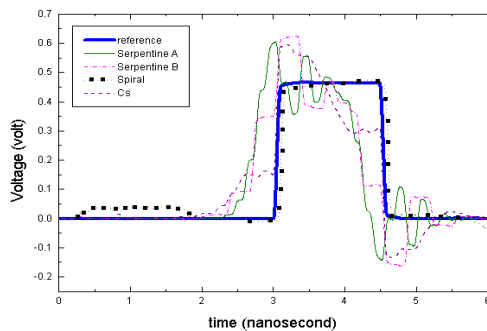


Fig. 15. Response of the concentric Cs line in comparison to the serpentine and spiral lines of equal length.

In comparison to the spiral line, the Cs line keeps the noise closer to the main signal, whereas the spiral line distributes the noise over longer time duration. From this perspective, the spiral line is superior to the Cs line. However, if one were to consider an excitation composed of a train of pulses, as would be the case in practical scenarios, it might be more advantageous to force the crosstalk noise to accumulate closer to the pulse that generates it and not interfere with other pulses.

## V. Summary

This paper presented a qualitative analysis of serpentine and flat spiral delay lines based on the simply, yet powerful, ray tracing technique. The three-dimensional FDTD method was used to predict the full-wave performance of these delay lines, thus accounting for higher-order modes, multiple and feedback coupling and the effect of orthogonal segments. Despite the strength and completeness of the FDTD method, the ray tracing method facilitated an understanding of the coupling mechanism in complex-shaped delay lines and lead to the introduction of novel delay line such as the flat spiral line. A new line, the concentric Cs delay line was introduced based on the concept of reducing the periodicity in the structural topology, thus forcing the crosstalk noise to accumulate asynchronously. Numerical simulation using the three-dimensional full-wave FDTD method showed that the new designs result in receiver waveform that is less susceptible to triggering false logic than in the case of the serpentine line.

## References

- [1] H. B. Bakoglu, *Circuits, Interconnections, and Packaging for VLSI*, Addison Wesley, Reading, MA, 1990.
- [2] R. B. Wu and F.L. Chao, "Laddering wave in serpentine delay-line," *IEEE Trans. Components Packaging Manufacturing Tech. Part-B Advanced Packaging*, Vol. 18, No. 4, pp. 644-650, Nov. 1995.
- [3] R. B. Wu and F.L. Chao, "Flat spiral delay line design with minimum crosstalk penalty," *IEEE Trans. Components Packaging Manufacturing Tech. Part-B Advanced Packaging*, Vol. 19, No. 2, pp. 397-402, May 1996.
- [4] O. M. Ramahi, "FDTD analysis of conventional and novel delay lines," Presented at the 16<sup>th</sup> Annual Review of Progress in Applied Computational Electromagnetics meeting, Monterey, CA, March 20-25, 2000.
- [5] N. Orlanovic, R. Raghuram and N. Matsui, "Characterization of microstrip meanders in PCB

interconnects,” Electronic Components and Technology Conference, Conference Proc., May 21-24, 2000.

- [6] B. J. Rubin and B. Singh, “Study of meander line delay in circuit boards,” *IEEE Trans. Microwave Theory Tech.*, Vol. 48, No. 9, pp. 1452-1460, Sept. 2000.



**Omar M. Ramahi**

received the BS degrees in Mathematics, and Electrical and Computer Engineering (highest honors) from Oregon State University, Corvallis, OR in 1984. He received his M.S. and Ph.D. in Electrical and Computer Engineering in 1986 and 1990,

respectively from the University of Illinois at Urbana-Champaign. From 1990-1993, Dr. Ramahi held a visiting fellowship position at the University of Illinois at Urbana-Champaign. From 1993 to 2000, he worked at Digital Equipment Corporation and then Compaq (presently, Hewlett Packard), where he was member of the Alpha Servers Product Development Group. In August of 2000, he joined the faculty of the A. James Clark School of Engineering at the University of Maryland at College Park, as an Assistant Professor in Mechanical Engineering, Assistant Affiliate Professor of Electrical and Computer Engineering, and a Faculty Member of CALCE Electronic Products and Systems Center.

Dr. Ramahi served as a consultant to several companies. He was instrumental in developing computational techniques to solve a wide range of electromagnetic radiation problems in the fields of antennas, high-speed devices and circuits and EMI/EMC. His interests include high-speed devices, packaging, and interconnects, experimental and computational EMI/EMC studies, biomedical applications of electromagnetics, novel optimization techniques, RF MEMS, interdisciplinary studies involving interaction of novel materials and electromagnetic energy, and high-impedance electromagnetic bandgap surfaces. He has authored and co-authored over 120 journal and conference papers and presentations, and has given numerous short courses to the industry. He is a co-author of the book *EMI/EMC Computational Modeling Handbook* (Kluwer Academic, 2<sup>nd</sup> Ed., 2001). Dr. Ramahi is a member of Eta Kappa Nu, Tau Beta Pi, Senior Member of IEEE and a member of the Electromagnetics Academy.

# An Empirical Approach for Design of Wideband, Probe-Fed, U-Slot Microstrip Patch Antennas on Single-layer, Infinite, Grounded Substrates

V. Natarajan and D. Chatterjee

**Abstract**—Wideband microstrip antennas with relatively simple topologies continue to attract attention for design of compact, high-performance communication systems. The coaxially-fed, rectangular patch U-slot has recently been investigated numerically and experimentally, and shown to yield 10 dB return-loss bandwidths in excess of 20%. However there are no analytical models, nor any systematic design procedures currently available that can aid realizing these configurations. To that end, based on extensive CAD simulation results for a wide range of commercially available microwave substrates ( $\epsilon_r = 2.94$  to 10.2), an *empirical design methodology* is derived and illustrated by examples. It is shown that the present empirical design technique, with its attendant limitations, generate wideband U-Slot designs that are optimized using CAD tools such as IE3D within a few iterations, resulting in substantially reduced overall process cycles.

## I. INTRODUCTION

The theory and design of a wide variety of probe-fed, microstrip patch antennas for various applications has been well documented [1]. For portable phone systems there is a need for low-profile (embedded) antennas with a 10 dB return-loss bandwidth  $\geq 10\%$  in addition to other desirable electrical characteristics [2, p. 312]. (The return loss, for this paper, is taken as  $-20 \log_{10} |\Gamma|$  in dB, where  $\Gamma$  is the reflection coefficient.) As found in [1, ch. 9], studies on wideband microstrip antenna designs emphasize techniques such as multi-layer substrates, parasitic elements and aperture-coupled excitations. However such approaches obviate the realization of low-profile, compact antenna topologies, or may complicate the fabrication process due to the need for sophisticated feed element design(s) [3].

Interestingly the U-slot antenna, first reported in [4], was a new form in ultrawideband microstrip antenna design since it could generate  $\approx 40\%$  bandwidth by maintaining very simple feed and patch designs on single-layer foam substrates. For wideband applications it thus appears that the U-slot design is a pioneering concept as it is indeed a very formidable alternative to the existing

wideband patch topologies [1],[3]. The subject of this paper is to further explore some advancements in design of wideband, probe-fed, U-slot patches on single-layer substrates.

Most results for this novel design are available for air ( $\epsilon_r = 1$ ) or foam ( $\epsilon_r \approx 1$ ) substrates [4]-[7]. One finds appropriate results for  $\epsilon_r = 2.33$  in [8], inclusive of finite ground-plane and substrate truncation effects. Currently there are no analytical models, nor empirical design relations available to initiate an U-slot design from some nominal specifications. In [6] an attempt has been made to use a  $[Y]_{3 \times 3}$  matrix representation for the U-slot, but the analytical expressions for the diagonal elements  $Y_{11,22,33}$  are unavailable. (It appears from [6] that their determination was done using iterative experimental techniques). Explicit formulas for the two resonant frequencies of the U-slot, with validation results for foam substrate are available in [9],[10] that are good only as important checks in a simulation.

Reduced U-slot patch size topologies have been reported in [11]-[14] with an average bandwidth of  $\sim 30\%$ . Furthermore, 10 dB return loss bandwidths of 44% and 50% have been reported in [15] and [16], respectively. Dual-band designs have been reported in [17] for substrates with permittivity  $\epsilon_r \sim 4.4$ , and in [18] wideband patch designs on multi-layer substrates have been reported. Results for U-Slot performance on microwave substrates have been summarized in [19], but without any design information. Recently, a different design procedure for U-Slot on single-layer microwave substrates has been reported in [20]. However, there are significant differences between [20], and the proposed approach in this paper. These differences will be identified later in this paper.

The information gleaned from [21] suggests avoiding use of moment-method [22],[23] based CAD tools like IE3D [24] for initiating single-element patch designs, due to prohibitively high computational cost. Thus efficient design processes, despite their heuristic/empirical nature, can still help the overall simulation cycle be cost-effective. Normally such empirical procedures reduce substantial savings in computational resources by requiring fewer iterations in the final CAD optimization of the antenna topology [21]. Since no formal, systematic pro-

Manuscript received February 18, 2003; revised June 4, 2003  
Division of Computer Science and Electrical Engineering, 570-F Flarsheim Hall, University of Missouri Kansas City (UMKC), 5100 Rockhill Road, KC, MO 64110, USA; e-mail: chatd@umkc.edu

cedures are currently available for the design of U-Slot, the purpose of this investigation is to develop guidelines and present empirical formulas to aid in realizing such goals.

The empirical formulas developed in this paper apply to probe-fed designs on single-layer grounded substrates that are (ideally) infinite in extent. In addition, empirical design formulas, obtained via moment-method based parametric simulations, apply to U-slots patch designs with definite geometrical symmetry as elaborated later in this paper. The contents of the paper are outlined next.

To that end, following [25]-[27], validation results for IE3D against appropriate measured data for microwave substrates ( $\epsilon_r = 2.33$ ) from [8], are included. The IE3D code validation results are followed by a careful analysis of the various U-Slot designs studied earlier [8],[28], resulting in various dimensional invariance relationships that are crucial for U-Slot design on microwave (and foam/air) substrates. Selected results demonstrating the validity of the empirical formulas are included from [29],[30]. Finally the major observations are summarized, and a list of relevant references is included.

## II. PROBLEM DESCRIPTION

In Fig. 1 the geometry of a probe-fed, U-Slot patch on a single-layer substrate is shown with all the dimensions indicated therein. This topology is a simple modification to a probe-fed rectangular patch antenna, the latter being generally a narrowband radiating element [1].

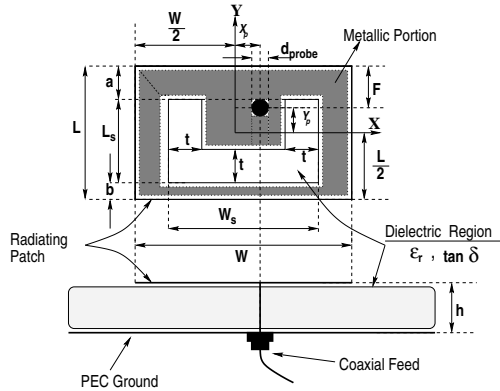


Fig. 1. Physical topology of a coaxially-fed, single-layer, rectangular patch U-Slot microstrip antenna

In absence of any analytical, *i.e.*, cavity or transmission line models [1, chs. 4,5], one can still investigate the effects on a performance characteristic (such as impedance, gain, *etc.*) due to variations in substrate/patch geometry via careful measurements or rigorous, full-wave CAD simulations [21]. Development of rapidly iterative design procedures could involve heuristic/empirical approaches, subject to further refinements via CAD optimizations [21].

For the investigation reported here, the main aim is to examine how parameters such as substrate thickness, overall patch dimensions, slot width, probe location and radius, as shown in Fig. 1, affect the wideband performance. The generic nature of the impedance character-

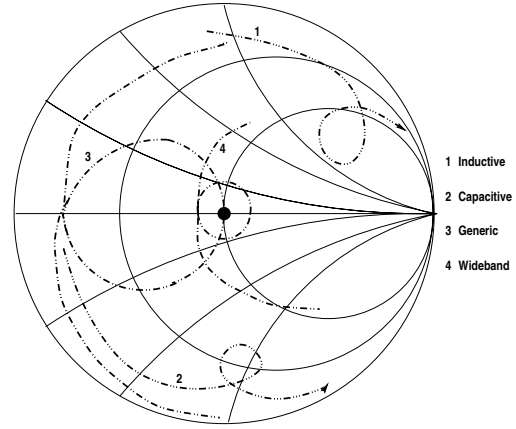


Fig. 2. Typical impedance loci characteristics. The performance of any wideband design (or modifications) is desired such that the loop of the impedance loci 1, 2 & 3 encircle the center ( $VSWR = 1$ ) of the Smith Chart as in locus 4.

istics is shown via a Smith Chart in Fig. 2. The desired characteristic is depicted in # 4. The wideband behavior of the antenna will be superior if the size of the loop for the impedance locus # 4 shrinks to the  $VSWR = 1$  point on the Smith Chart. (In addition, most of the frequencies of interest has to lie on that loop.) For practical applications, the size and location of the loop in an impedance loci should be such that the  $VSWR \leq 2$ , corresponding to a return loss of 10 dB.

Generally, the impedance loci will be far removed from the desired behavior shown in # 4, *i.e.*, it will be more like the loci # 1, 2 or 3. The wideband problem then reduces to the study of how the changes in various dimensions in Fig. 1 could transform loci # 1, 2 & 3 such that a loop could be obtained in the impedance loci meeting the criterion  $VSWR \leq 2$ .

It is possible to analyze the impedance behavior using analytical (cavity model) expressions, to a very good degree of accuracy [1, chs. 4 and 5]. Such would facilitate rapid parametric simulations, prior to any computationally intensive, full-wave analysis. Since there exists no such analytical model for U-Slots, having recourse to an alternate route for rapid parametric studies appears critical before any CAD-based optimization. To that end, it is necessary to examine the capability of the IE3D code for numerical modeling of U-Slot geometries. The results for the IE3D code validation are shown next.

## III. VALIDATION RESULTS FOR THE IE3D CODE [24]

As mentioned in [25]-[27], a CAD tool needs to be validated for an ensemble of appropriate test cases that are closest to the topology being studied. Furthermore,

since code validation is an open-ended process, a judicious selection of the test cases forms an important part of such investigation. To that end, it was decided to examine the capabilities of the IE3D code against the measured radiation pattern data (in  $\phi = 0^\circ, 90^\circ$  planes) for U-Slots fabricated on substrate  $\epsilon_r = 2.33$  as given in [8, Fig. 5] corresponding to a frequency of 3.56 GHz. To the best of the knowledge of the present investigators, reference [8] is the only source for which measured and computed data are available for U-Slots on finite ground planes for microwave substrates. (Most of the data, as mentioned earlier, is for foam (or air) substrates for U-Slot topologies.)

The dimensions of the antenna B as in [8, Table I] are:  $W = 3.6$  cms,  $L = 2.6$  cms,  $W_s = 1.4$  cms,  $L_s = 1.8$  cms,  $b = 0.4$  cms,  $t = 0.2$  cms,  $X_p = 0.0$  cms,  $Y_p = 0.0$  cms, and  $F = 1.3$  cms, referring to Fig. 1 herein. The radius of the probe could not be found in [8]; after several trials, it was found that  $d_{\text{probe}} = 0.127$  cms in Fig. 1 provided the best agreement with the data in [8]. The

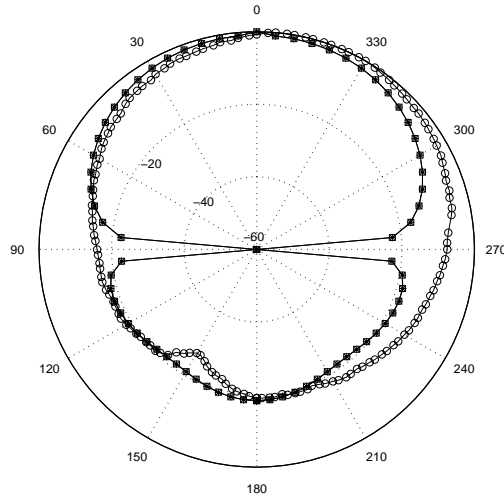


Fig. 3. Measured  $\circ - \circ - \circ$  data [8, Fig. 5]; computed  $\square - \square - \square$  (IE3D 8.0) and  $* - * - *$  (IE3D 9.0), for total fields in  $\phi = 0^\circ$  plane

IE3D results in Figs. 3 and 4 are for a  $12 \times 10$  cms rectangular ground plane. The agreement between measured [8] and simulated results are reasonably acceptable at all angular regions except near  $\theta \rightarrow 90^\circ, 270^\circ$ . The reason(s) for the discrepancies are explained below.

The actual topology analyzed in [8, Fig. 1] was a U-Slot located on truncated, rectangular substrate on a finite rectangular ground plane. In the IE3D simulations, the radiating patch was located on an infinite substrate backed by a finite rectangular ground plane of the same dimensions. This model cannot account for the surface wave diffraction by the truncated dielectric substrate. Since surface waves are dominant near the air-substrate interface, (*i.e.*  $\theta \rightarrow 90^\circ, 270^\circ$ ), the radiation behavior is not accurately predicted near this region as seen in Figs. 3 and 4. This present limitation in the

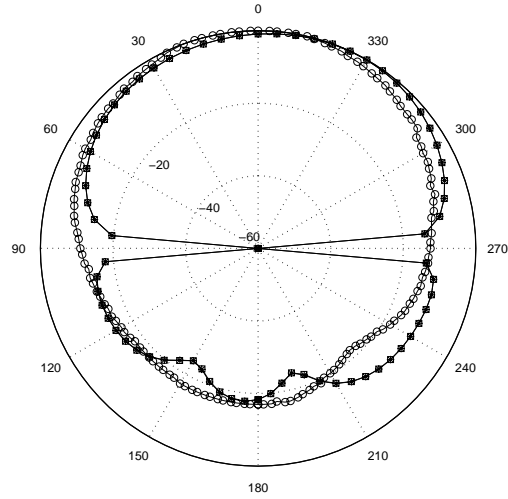


Fig. 4. Measured  $\circ - \circ - \circ$  data [8, Fig. 5]; computed  $\square - \square - \square$  (IE3D 8.0) and  $* - * - *$  (IE3D 9.0), total fields in  $\phi = 90^\circ$  plane.

IE3D code [24] is due to lack of implementation of the appropriate microstrip Green's function that can account for diffractions due to dielectric and ground-plane truncations. In [8], since the FDTD technique was used to calculate the radiation pattern, such edge diffractions are considered *in situ*. Thus, computed patterns in [8] do not show any fictitious discontinuities near  $\theta \rightarrow 90^\circ, 270^\circ$ , unlike the IE3D results presented here.

The foregoing results demonstrate the limitations of the IE3D code when applied to modeling of antennas on grounded, truncated substrates. However the 2:1 VSWR bandwidth of antenna B, computed via IE3D, was around 24% - in good agreement with measurements [8, Table II]. Also, the IE3D code had been used to replicate the results for microstrip antennas on infinite, grounded substrates with the test cases chosen from various topologies in [1]. In all these cases the agreements were very good with published data. Since the scope of this present investigation is limited to infinite, grounded substrates the type of discrepancies in Figs. 3 and 4 are not likely to affect the results.

#### IV. DIMENSIONAL INVARIANCE IN U-SLOT DESIGN

The key to the development of the empirical design procedure is the establishment of the dimensional invariance of the U-Slot studied in [8] and [28]. These results are summarized below in table I from [29],[30]. In table I one finds that the only parameter which changes with substrate  $\epsilon_r$  is  $\frac{W}{h}$ , and all other dimensional ratios remain *almost invariant*. Consequently, to design a U-Slot on an infinite, grounded microwave substrate the determination of  $\frac{W}{h}$  for a specific substrate ( $\epsilon_r$  and  $h$ ) and resonant/design frequency,  $f_r$ , is the key step. One can then use the information in table I to derive the topology of the patch as shown in Fig. 1. From columns 3, 4 and 7 in table I one can easily deduce that  $\frac{W}{L} \approx 1.38$ . Inter-



TABLE I  
DIMENSIONAL INVARIANCE IN U-SLOT DESIGNS.

$\epsilon_r$	$\frac{W}{h}$	$\frac{L}{L_a}$	$\frac{W_a}{L_a}$	$\frac{L_a}{b}$	$\frac{t}{W_a}$	$\frac{W}{W_a}$
1.0	8.168	1.515	0.835	4.237	0.13	3.203
2.33	4.49	1.445	0.777	4.5	0.144	2.573
4.0	3.87	1.443	0.776	4.51	0.144	2.573
9.8	2.87	1.442	0.777	4.48	0.144	2.574
2.33	5.624	1.444	0.777	4.5	0.143	2.571

The data have been obtained from [28] and [8], for the first four and last row, respectively. For all the cases cited here, the minimum and maximum bandwidths were 15% and 42%, respectively. The data for  $\epsilon_r = 2.33$  in the second and fifth rows refer to U-Slot topologies from [28] and [8], corresponding to 900 MHz and 3.26 GHz, respectively.

estingly, this fact appears to have been confirmed for the U-Slot data presented in [19, table 1b].

At this stage it is important to distinguish between the approach in [20] and this paper. It is noted that [20], like this paper, doesn't contain any full-wave mathematical analysis for U-Slot. One of the main differences, in context of table I, is the determination of U-Slot dimensions [20, sec. III]. The underlying assumption in [20, sec. III] is the existence of four different resonant frequencies of the impedance loop (as shown in locus # 4 in Fig. 2) for the U-Slot. For high  $\epsilon_r$  substrates such multiple resonances may not occur, but an impedance loop could still form, as shown in Fig.2, away from the zero reactance ( $jX = 0$ ) line on the Smith Chart. Apparently, this restricts the technique in [20, sec. III] primarily to low  $\epsilon_r$  substrates. In contrast, the dimensional invariances (table I) apply to low, medium and high permittivity substrates.

Since it is important how the various dimensions in Fig. 1 could affect the bandwidth, a detailed study was undertaken to examine such effects, for which salient features are shown in the following section.

V. PARAMETRIC MODELING STUDIES VIA IE3D CODE [24]

The primary objective of the parametric simulations is to examine the nature of the input impedance variations as shown in Fig. 2 in section II. Assuming that the initial topology of the U-Slot has been designed using the information in section IV, it is still possible that the desired bandwidth may not have been achieved. This implies that the initial design needs further optimization, which in view of Fig. 2 implies that the impedance loop should be shrunk to encircle the vicinity of the center of the Smith Chart. The parameters that exercise significant control on the impedance loop size and location are critical to the optimization process. Results for low and high permittivity substrates are available in [29], and only selected results for  $\epsilon_r = 4.5$  are shown here from Figs. 5 to 9. The data are included in the individual figures captions, and hence are not repeated here to avoid tedium. In Fig. 5,  $Y_p = -0.2$  and 0.4 cms refer to probe locations below and above the origin of the coordinate

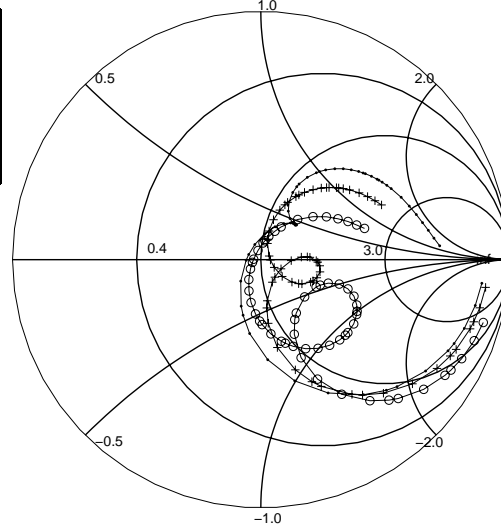


Fig. 5. Effect of probe location on the impedance behavior of U-Slot:  $\epsilon_r = 4.5$ ,  $\tan \delta = 0.002$ ,  $W = 4.89$ ,  $L = 3.538$ ,  $h = 1.27$ ,  $L_s = 2.45$ ,  $W_s = 1.9$ ,  $t = 0.274$ ,  $a = 0.777$ ,  $b = 0.311$ , (i.e.,  $\frac{a}{b} = 2.5$ ),  $d_{probe} = 0.127$  and  $X_p = 0.0$  - all in cms;  $\cdot \cdot \cdot \cdot$  ( $Y_p = 0.4$  cms),  $+ + + +$  ( $Y_p = 0.2$  cms), and  $o - o - o$  ( $Y_p = -0.2$  cms), referring to the dimensions shown in Fig. 1.

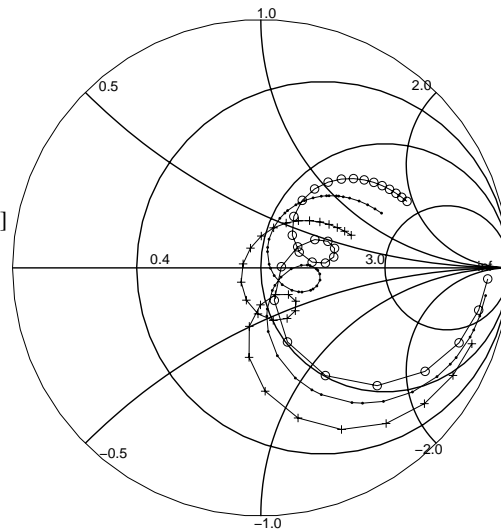


Fig. 6. Effect of probe radius on the impedance behavior of U-Slot:  $\epsilon_r = 4.5$ ,  $\tan \delta = 0.002$ ,  $W = 4.89$ ,  $L = 3.538$ ,  $h = 1.27$ ,  $L_s = 2.45$ ,  $W_s = 1.9$ ,  $t = 0.274$ ,  $a = 0.777$ ,  $b = 0.311$ , (i.e.,  $\frac{a}{b} = 2.5$ ),  $X_p = Y_p = 0.0$  - all in cms;  $o - o - o$  ( $d_{probe} = 0.08636$  cms),  $\cdot \cdot \cdot \cdot$  ( $d_{probe} = 0.127$  cms), and  $+ + + +$  ( $d_{probe} = 0.2$  cms), referring to the dimensions shown in Fig. 1.

system, respectively, with  $X_p = 0$ , as shown in Fig. 1. The result indicates the trend that as the probe is moved away from the edge of the slot, the impedance loop becomes more inductive and its size decreases. Similar trends were observed for other substrate cases in [29].

Fig. 6 shows the effects of the probe radius ( $= \frac{1}{2}d_{probe}$ ) on the input impedance. In contrast to the result in Fig. 5, variations in probe radius doesn't shrink or expand the size of the loop. The comparison further indicates that the dominant effect of the probe on the U-Slot input impedance is determined by its location, and not radius. Control of the probe radius could thus be viewed as resulting in a 'fine-tuning' mechanism in order to obtain the desired wideband behavior.

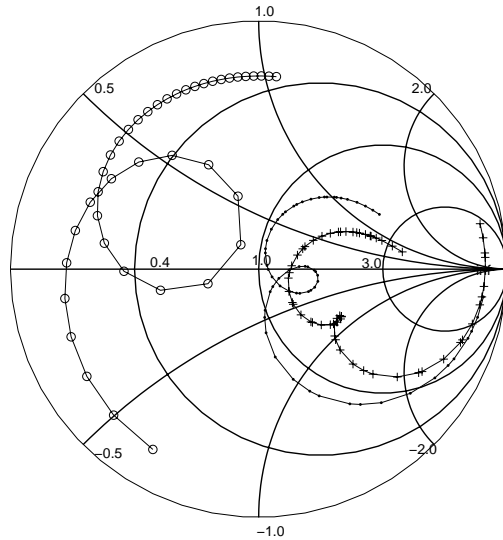


Fig. 7. Effects of substrate thickness on the impedance behavior of U-Slot:  $\epsilon_r = 4.5, \tan \delta = 0.002, W = 4.89, L = 3.538, L_s = 2.45, W_s = 1.9, t = 0.274, a = 0.777, b = 0.311, (i.e., \frac{a}{b} = 2.5), d_{probe} = 0.127, X_p = Y_p = 0.0$  - all in cms;  $\circ - \circ - \circ$  ( $h = 0.6$  cms),  $\cdot - \cdot - \cdot$  ( $h = 1.27$  cms), and  $+ - + - +$  ( $h = 1.5$  cms), referring to the dimensions shown in Fig. 1.

In Fig. 7 the trends in impedance behavior with increase in substrate thickness,  $h$ , are shown. As the thickness increases from 0.6 cms to 1.5 cms, the impedance loop decreases in size and becomes more capacitive in character. For  $h = 1.27$  cms, a loop in the impedance behavior is formed closest to the center of the Smith Chart - indicative of wideband behavior.

Variation in the U-slot width,  $t$ , results in impedance changes (Fig. 8) similar to the one observed for probe-location variations in Fig. 5. As the U-slot width increases from 0.2 cms to 0.35 cms, the impedance loop changes from being inductive to capacitive, and for a slot-width  $t = 0.274$  cms the loop is located close to the center of the Smith Chart.

Increase in the  $\frac{a}{b}$  ratio from 0.5 to 4.5 doesn't cause any *significant* change in the location of the impedance loop, but results in shrinking of its size. This can be

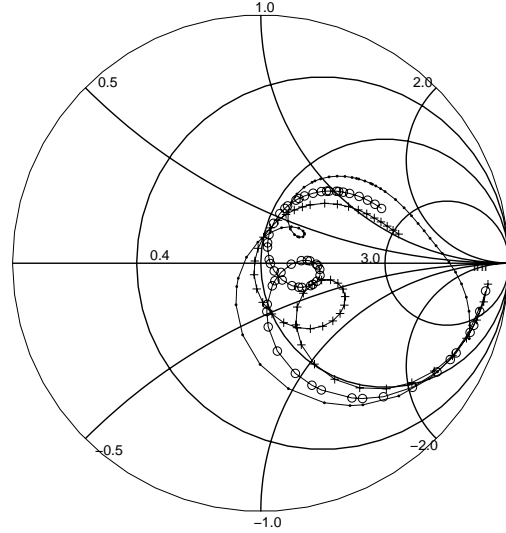


Fig. 8. Effects of slot width,  $t$ , on the impedance behavior of U-Slot:  $\epsilon_r = 4.5, \tan \delta = 0.002, W = 4.89, L = 3.538, L_s = 2.45, W_s = 1.9, a = 0.777, b = 0.311, (i.e., \frac{a}{b} = 2.5), d_{probe} = 0.127, X_p = Y_p = 0.0$  - all in cms;  $\cdot - \cdot - \cdot$  ( $t = 0.2$  cms),  $\circ - \circ - \circ$  ( $t = 0.274$  cms),  $+ - + - +$  ( $t = 0.35$  cms) referring to the dimensions shown in Fig. 1.

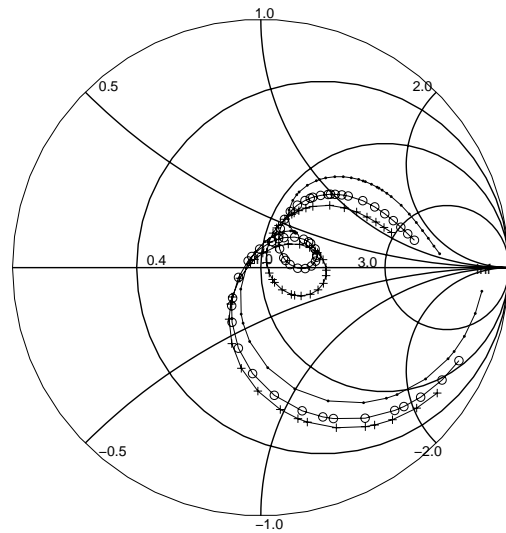


Fig. 9. Effects of  $\frac{a}{b}$  ratio on the impedance behavior of U-Slot:  $\epsilon_r = 4.5, \tan \delta = 0.002, W = 4.89, L = 3.538, L_s = 2.45, W_s = 1.9, t = 0.274, d_{probe} = 0.127, X_p = Y_p = 0.0$  - all in cms;  $\cdot - \cdot - \cdot$  ( $\frac{a}{b} = 4.5$ ),  $\circ - \circ - \circ$  ( $\frac{a}{b} = 1.0$ ),  $+ - + - +$  ( $\frac{a}{b} = 0.5$ ), referring to the dimensions shown in Fig. 1.

inferred from Fig. 9.

The information gleaned from the most important parametric simulation results, as shown in Figs. 5 to 9, suggests the following optimization guidelines for wideband U-Slot design:

- change the slot width,  $\tau$ , probe location  $Y_p$ , and substrate thickness  $h$ , such that the impedance loop encircles the region in the close vicinity of the center of the Smith Chart;
- following step (a), if the size of the loop is undesirably large or small, increase or decrease the  $\frac{a}{b}$  ratio to reduce the loop size without affecting the location of the loop to achieve larger bandwidth
- one may, optionally, change the probe radius to move the impedance loop such that it encircles, or is close to the Smith center ( $VSWR = 1$ )

The preceding simulation results were obtained for configurations where the U-slot is symmetric about the  $x$  axis and the probe is located such that  $X_p = 0$ , as shown in Fig. 1. Again, it is important to distinguish between [20] in context of the parametric simulations in the present investigation. This will be followed by the last part, *i.e.*, development of the empirical design equations, in section VI.

The parametric simulations in [20, sec. II] focussed mainly on the variation in resonant frequencies. (The U-Slot geometry studied in [4] was for air  $\epsilon_r = 1$  which was scaled to  $\epsilon_r = 2.2$  in [20]). The technique in [20, sec. III] is based on the availability of limited data. Furthermore, as stated in [20, sec. V], the effects of substrate and (probe) feed were not investigated in detail. The information gleaned from the overall comparisons between [20] and the present paper suggests that the results included here have broader scope of applicability compared to [20].

## VI. DEVELOPMENT OF EMPIRICAL DESIGN FORMULAS

In view of the observations on dimensional invariance, as presented in table I, the important factor that *initiates* the U-slot design is a knowledge of the  $\frac{W}{h}$  ratio from an a-priori knowledge of some nominal specifications.

Consequently, it was decided to examine the relationships between resonant frequency,  $f_r$ , substrate parameters  $\epsilon_r$  and  $h$ , and, the larger dimension,  $W$ , of the U-Slot. To that end, following the data in table I, it was decided to vary  $\frac{W}{h}$  between 2 and 7, in increments of 0.5. A typical substrate was chosen and from the pre-selected  $\frac{W}{h}$  values, the U-Slot dimensions were found with the aid of table I. Following this procedure, various U-Slots were designed for a wide class of practical substrates available from Rogers Corp. (We must emphasize that at this stage the resonant frequency,  $f_r$ , is unknown and was determined as described below.)

These U-Slot topologies were then characterized by the full-wave CAD tool IE3D [24]. The resonant frequency  $f_r$ , defined by zero reactance on the Smith Chart, and the corresponding fractional 2:1 VSWR bandwidths

for each case were noted. (If there were several resonant frequencies in the 2:1 VSWR range, an average estimate of  $f_r$  was taken [29].) Each discrete pair of  $\frac{W}{h}$  and  $f_r$  values, corresponding to an individual design, were plotted. The MATLAB software (version 6.1, release 12.1) was used to obtain a quadratic relation ('best fit') for these  $\frac{W}{h}$  vs.  $f_r$  plots. For a any specific  $\epsilon_r$ , and various  $h$ , several such equations were obtained, as shown in table II. In this process, it was observed that a  $\geq 20\%$  fractional bandwidth for the 2:1 VSWR range was obtained for those designs obeying  $3.5 \leq \frac{W}{h} \leq 5.5$ . The same phenomenon also corresponded to the range  $0.13 \leq \frac{h\sqrt{\epsilon_r}}{\lambda} \leq 0.18$  for the U-Slot topologies designed and simulated on  $\epsilon_r = 2.94, 4.5$ , and  $10.2$ . (Here  $\lambda$  corresponded to the resonant frequency  $f_r$ , determined from the Smith Chart.) The details can be found in [29],[30] and are omitted here for brevity.

TABLE II  
EMPIRICAL (QUADRATIC) EQUATIONS FOR DESIGN OF U-SLOT

h (cms)	$\epsilon_r = 2.94$	$\epsilon_r = 4.5$	$\epsilon_r = 10.2$
0.635	$\frac{W}{h} = 0.1 f_r^2 - 1.8 f_r + 10$	$\frac{W}{h} = 0.088 f_r^2 - 1.5 f_r + 8.5$	$\frac{W}{h} = 0.063 f_r^2 - 1.7 f_r + 9.1$
1.0	$\frac{W}{h} = 0.2 f_r^2 - 2.4 f_r + 9.2$	$\frac{W}{h} = 0.19 f_r^2 - 2.1 f_r + 7.8$	$\frac{W}{h} = -0.78 f_r^2 - 0.3 f_r + 8.8$
1.216	$\frac{W}{h} = 0.62 f_r^2 - 4.8 f_r + 12$	$\frac{W}{h} = 0.085 f_r^2 - 1.7 f_r + 6.8$	$\frac{W}{h} = -0.21 f_r^2 - 2.2 f_r + 8.1$
1.80	$\frac{W}{h} = 1.8 f_r^2 - 8.6 f_r + 13$	$\frac{W}{h} = 0.89 f_r^2 - 4.8 f_r + 8.5$	$\frac{W}{h} = -0.89 f_r^2 + 0.11 f_r + 4.5$

Here  $f_r$  is the *design* resonant frequency in GHz, and  $h$  and  $\epsilon_r$  are the substrate thickness and permittivities, respectively.

The next section illustrates the complete empirical design procedure with simulation results for a topology ( $\epsilon_r = 3.27$ ) for which the empirical equations are not available in table II.

## VII. EMPIRICAL DESIGN TECHNIQUE FOR U-SLOT

In this section, a systematic empirical design procedure for design of U-Slot patch antennas on microwave substrates is presented from [29]. It is shown, from the results in secs. IV, V and VI, that U-Slot patch antennas can be realized which are further optimized using IE3D CAD software [24]. VSWR and boresight ( $\phi = 0^\circ, \theta = 0^\circ$ ) Gain results for the *unoptimized* and *optimized* U-Slot topologies are included to demonstrate the efficacy of the empirical design procedure.

The limitation of this design procedure, as mentioned before, is that the U-Slot, as shown in Fig. 1, is located symmetrically w.r.t coordinate axes with the probe is on the  $y$  axis. (For rapid automated calculations, the design procedure can easily be adapted within a computer design/simulation code.) It is *assumed* that the U-slot antenna should have a 10 dB return loss bandwidth of  $\geq 20\%$ , after final optimization. Another limitation is

that the dimension  $a = b$  in this design approach, and the slot width,  $t$ , remains uniform.

- (1) From the nominal a-priori specifications for resonant frequency  $f_r$ , select a commercially available substrate with  $\epsilon_r$ , thickness  $h$  to satisfy the criterion  $0.13 \leq \frac{h\sqrt{\epsilon_r}}{\lambda} \leq 0.18$ . In the experience of the present authors the upper and lower limiting values should be used for low- and high-permittivity substrates, respectively. For intermediate permittivity substrates ( $\epsilon_r \approx 4.5$ ) the criterion  $\frac{h\sqrt{\epsilon_r}}{\lambda} \approx 0.15$  can be used.
- (2) Employ the empirical equations from table II to calculate the  $\frac{W}{h}$  ratio, and from step (1), one can subsequently determine the overall width  $W$ . (One may check for the additional criterion  $3.5 \leq \frac{W}{h} \leq 5.5$ , upon calculation of the  $\frac{W}{h}$  ratio.)
- (3) From table I, one uses  $\frac{W_s}{W} \approx 2.57$  to determine  $W_s$ .
- (4) From table I, since  $\frac{W_s}{L_s} \approx 0.777$ , calculate  $L_s$  with the knowledge of  $W_s$  from step (3).
- (5) From the relation  $\frac{t}{W_s} \approx 0.144$  in table I, calculate the slot width  $t$ , with the knowledge of  $W_s$  from (3). (This assumes a slot of *uniform* width.)
- (6) Similarly, from table I, via the relation  $\frac{L_s}{b} \approx 4.5$ , calculate  $b$  with a knowledge of  $L_s$  from (4).
- (7) Assume  $a = b$  in Fig. 1, and calculate  $L = L_s + a + b = L_s + 2a = L_s + 2b$ .
- (8) Locate the coaxial probe exactly at the center, i.e.,  $X_p = 0$  and  $Y_p = 0$ , (or equivalently  $F = \frac{L}{2}$ ).
- (9) Simulate the U-Slot geometry, as obtained via steps 1 to 8, using IE3D (or any other microstrip CAD package [27]), and check for the 2:1 VSWR performance.
- (10) By examining the nature of the impedance variation on a Smith Chart, from step (9), adjust the parameters (as mentioned in sec. V) for further improvement of wideband performance of U-Slot.

In order to illustrate the application of the preceding design steps, several topologies were modeled - for which the results are available in [29],[30]. The results contained in [29] (and [30]) mainly demonstrate the applicability of the empirical design procedure for those substrates for which the empirical relations are contained in table II. In this paper separate results are presented for a typical case  $\epsilon_r = 3.27$  (TMM3), for which no information is available in tables I and II. Since the permittivity of (TMM3) lies in the range  $2.94 \leq \epsilon_r = 3.27 \leq 4.5$ , so either of the equations in table II can be used. These would result in two different dimensions for the U-Slot, as  $\frac{W}{h}$  would be different for the two cases. The results from IE3D [24] simulation for the two U-Slot topologies are presented here to illustrate any such differences.

For the TMM3 ( $\epsilon_r = 3.27$ ) substrate, an operating frequency  $f_r = 2.3$  GHz was chosen. From the condition  $\frac{h\sqrt{\epsilon_r}}{\lambda} \approx 0.15$ , it was found that  $h = 1.08$  cms. Referring to table II the equations for  $\epsilon_r = 2.94$  and  $4.5$ , corresponding to a substrate thickness  $h = 1.0$  cms,

were chosen. It was found that  $\frac{W}{h} = 4.738$  ( $\epsilon_r = 2.94$ ) and  $3.975$  ( $\epsilon_r = 4.5$ ) via the two appropriate empirical relations from table II. The remainder of the dimensions were easily found following steps (1) to (8).

At this stage, the (initial) unoptimized design, obtained by following steps (1) to (8) *only*, was characterized by the IE3D code. The VSWR vs. frequency results were then examined, and the probe location was changed from its initial/unoptimized value ( $X_p = 0$  and  $Y_p = 0$ ) by moving the probe along the y axis to  $Y_p = 0.1$  cms, in view of the results in Fig. 5. (Various other optimization options in section V could have been pursued as well.) The VSWR and boresight gain vs. frequency for the unoptimized and optimized U-Slot topologies are compared to demonstrate the quality of the initial (unoptimized) design obtained via steps (1) to (8).

The final dimensions of the two U-Slot patches ( $\epsilon_r = 3.27$ ) obtained from the two empirical equations in table II are given below. (These geometries include the *optimized* probe locations obtained for enhanced bandwidths.)

- (i) via the empirical equation for  $\epsilon_r = 2.94$  in table II:  $W = 4.738$ ,  $L = 3.424$ ,  $W_s = 1.841$ ,  $L_s = 2.37$ ,  $h = 1.0$ ,  $t = 0.265$ ,  $a=b = 0.527$ ,  $X_p = 0$ ,  $Y_p = 0.1$  and  $d_{probe} = 0.127$  cms; substrate  $\epsilon_r = 3.27$
- (ii) via the empirical equation for  $\epsilon_r = 4.5$  in table II:  $W = 3.975$ ,  $L = 2.872$ ,  $W_s = 1.545$ ,  $L_s = 1.988$ ,  $h = 1.0$ ,  $t = 0.223$ ,  $a=b = 0.442$ ,  $X_p = 0$ ,  $Y_p = 0.1$  and  $d_{probe} = 0.127$  cms; substrate  $\epsilon_r = 3.27$

For the two topologies, the VSWR, Gain variations vs. frequency and the radiation patterns in the cardinal planes ( $\phi = 0^\circ$  and  $90^\circ$ ) were obtained via IE3D code [24], and are shown in Figs. 10 to 17. The data in Figs. 10 to 13 compare the performances of the unoptimized and optimized designs. The results are briefly discussed, next.

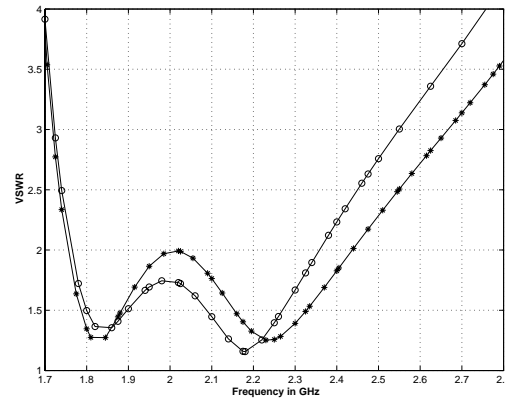


Fig. 10. Illustrating differences in VSWR for unoptimized (\* - \* - \*)  $X_p = Y_p = 0.0$  cms, and optimized (o - o - o:  $X_p = 0.0$  and  $Y_p = 0.1$  cms) U-Slot geometry as described in (i).

The results in Figs. 10 and 11 suggest that the unoptimized U-Slot design for  $\epsilon_r = 3.27$ , obtained via

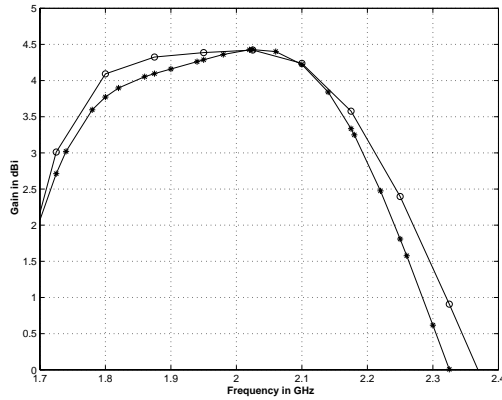


Fig. 11. Illustrating differences in boresight Gain ( $\phi = 0^\circ, \theta = 0^\circ$ ) for unoptimized (\* - \* - \*:  $X_p = Y_p = 0.0$  cms), and optimized ( $\circ - \circ - \circ$ :  $X_p = 0.0$  and  $Y_p = 0.1$  cms) U-Slot geometry as described in (i).

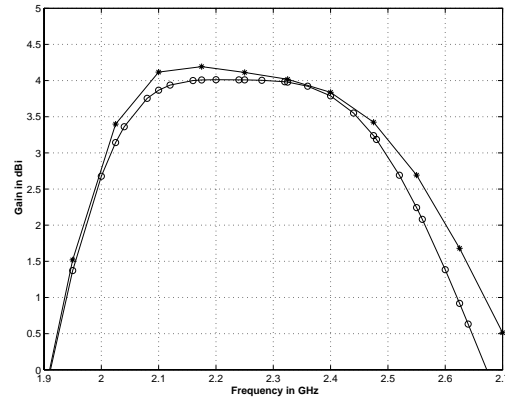


Fig. 13. Illustrating differences in boresight Gain ( $\phi = 0^\circ, \theta = 0^\circ$ ) for unoptimized (\* - \* - \*:  $X_p = Y_p = 0.0$  cms), and optimized ( $\circ - \circ - \circ$ :  $X_p = 0.0$  and  $Y_p = 0.1$  cms) U-Slot geometry as described in (ii).

the  $\epsilon_r = 2.94$  equation, performs well within expectations. The 2:1 VSWR bandwidths for the unoptimized and optimized topologies are  $\approx 33\%$  and  $30\%$ , respectively. One also notices that for the unoptimized case the overall VSWR performance is somewhat inferior compared to the optimized U-Slot topology. This conclusion can be reached by examining the VSWR behavior in the vicinity of 2 GHz for the two cases. By moving the probe, however, the overall VSWR behavior is improved at the expense of some reduction in bandwidth. The gain behavior in Fig. 11 does not show marked changes.

would not show perceptible changes in gain behavior if their wideband performance is enhanced by changing the probe location. Similar influence of probe location was observed for other designs, and are contained in [29],[30].

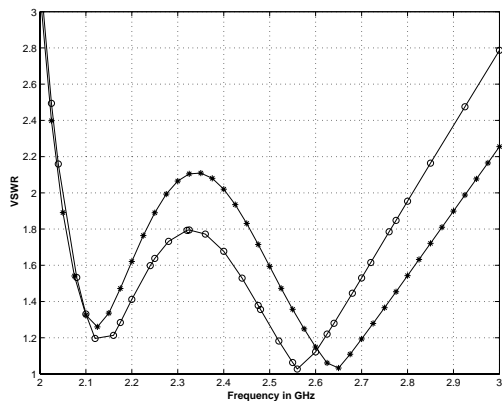


Fig. 12. Illustrating differences in VSWR for unoptimized (\* - \* - \*:  $X_p = Y_p = 0.0$  cms), and optimized ( $\circ - \circ - \circ$ :  $X_p = 0.0$  and  $Y_p = 0.1$  cms) U-Slot geometry as described in (ii).

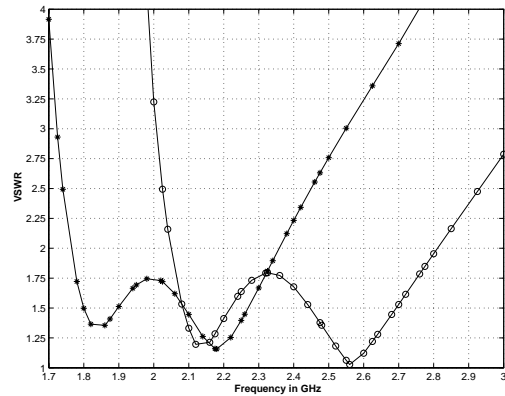


Fig. 14. VSWR characteristics for U-Slot on substrate  $\epsilon_r = 3.27, \tan \delta = 0.002$  and  $h = 1.0$  cm; \* - \* - \* and  $\circ - \circ - \circ$  refer to designs derived from empirical equations for  $\epsilon_r = 2.94$  and  $4.5$ , respectively, from Table II. The data refers to optimized designs only.

Results in Figs. 12 and 13 exhibit similar characteristics when compared to Figs. 10 and 11. Comparing the VSWR variations in Figs. 10 and 12, one notices that unoptimized (initial) design is a good estimate that could be optimized using few iterations on the probe location. Interestingly, the boresight gain variations in Figs. 11 and 13 are rather insensitive to probe locations. This observation suggests that initial (unoptimized) U-Slot designs,

Results in Figs. 14 to 17 refer to *optimized* topologies as defined earlier in (i) and (ii). The VSWR results in Fig. 14 indicate that both designs offer  $\approx 30\%$  bandwidths corresponding to a return loss of 10 dB. However the frequency ranges over which such wideband behavior occurs is different for the two designs. For both designs,  $VSWR \leq 2$  at the original design frequency of 2.3 GHz.

The gain characteristics shown in Fig. 15 reveal that the two U-Slot designs exhibit overall similarities, except that the topology derived from the empirical equation for  $\epsilon_r = 4.5$  shows improved 'gain-flatness'. However at 2.3 GHz the gain values are 0.6 and 4 dB, respectively, for

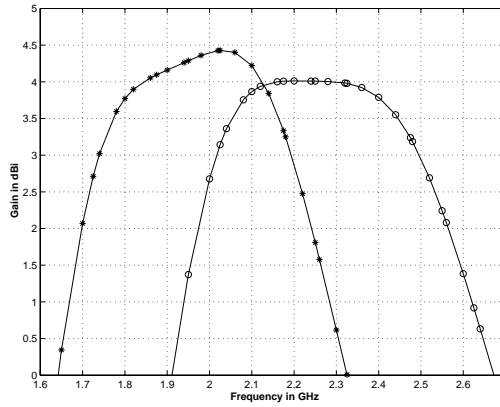


Fig. 15. Boresight ( $\theta = 0^\circ, \phi = 0^\circ$ ) gain characteristics for U-Slot on substrate  $\epsilon_r = 3.27, \tan \delta = 0.002$  and  $h = 1.0$  cm; \* - \* - \* and  $\circ - \circ - \circ$  refer to designs derived from empirical equations for  $\epsilon_r = 2.94$  and  $4.5$ , respectively, from Table II. The data refers to optimized designs only.

U-Slot geometry defined in (i) and (ii).

Examining the VSWR and gain characteristics for the two optimized designs (i) ( $\epsilon_r = 2.94$ ), and (ii) ( $\epsilon_r = 4.5$ ), one can explain the differences by realizing that these are essentially two *different* U-Slot geometries on the same substrate material ( $\epsilon_r = 3.27$  and  $h = 1.0$  cms). When these two were simulated via the IE3D code the results were, quite predictably, different and is seen in Figs. 14 and 15.

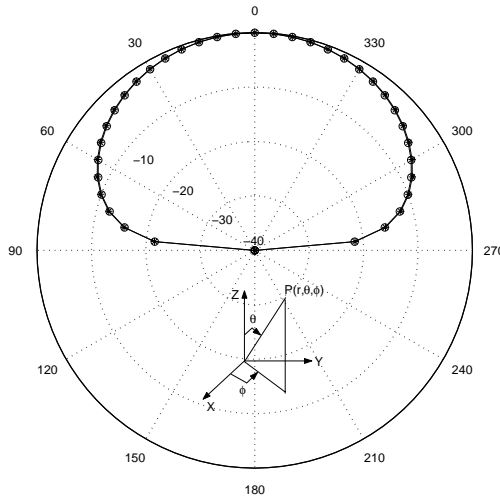


Fig. 16. Radiation pattern vs. polar angle  $\theta$  in  $\phi = 0^\circ$  plane for U-Slot on substrate  $\epsilon_r = 3.27, \tan \delta = 0.002$  and  $h = 1.0$  cm.  $\diamond - \diamond - \diamond$  (2.0 GHz) and  $\square - \square - \square$  (2.3 GHz) refer to designs derived from empirical equations for  $\epsilon_r = 2.94$  and  $4.5$ , respectively, from Table II. The data refers to optimized designs only.

The principal plane radiation patterns in Figs. 16 and 17. The patterns are shown for 2.0 and 2.3 GHz, for respective maximum boresight gains as in Fig. 15. The results show almost no difference for the two U-Slot de-

signs.

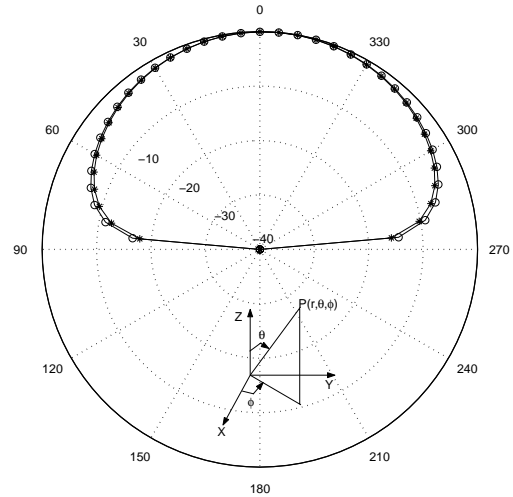


Fig. 17. Radiation pattern vs. polar angle  $\theta$  in  $\phi = 90^\circ$  plane for U-Slot on substrate  $\epsilon_r = 3.27, \tan \delta = 0.002$  and  $h = 1.0$  cm;  $\diamond - \diamond - \diamond$  (2.0 GHz) and  $\square - \square - \square$  (2.3 GHz) refer to designs derived from empirical equations for  $\epsilon_r = 2.94$  and  $4.5$ , respectively, from Table II. The data refers to optimized designs only.

One may thus conclude, judging qualitatively the results in Figs. 10 to 17, that the empirical formulas in table II are reasonably reliable, and have a wider scope of applicability as compared to [20]. Follow-up investigations, comparing the present design method and [20, sec. III] are planned for future work.

VIII. DISCUSSION AND FUTURE WORK

The empirical design technique developed here for U-slot patches in section VII is by no means exhaustive. The most important part in the design are embodied in steps 1 to 8 in sec. VII, that yield a basic design. Steps 9 and 10 are essentially equivalent to the optimization functions available in the IE3D code [24]. The utility of steps 9 and 10, from a practical point of view, stem from the fact that not all microstrip antenna CAD tools contain this optimization facility [27] like the IE3D code [24]. In those special situations steps 9 and 10 can play a critical role in the final design. It is however important to assess how the optimizers, currently available in IE3D, compare with an U-slot design obtained via the parametric simulation studies (steps 9 & 10 in sec. VII). This work is currently in progress, and the final (optimized) results shall also be compared against the Ansoft ENSEMBLE microstrip CAD software for the various optimization options available in IE3D [24]. In addition, in view of the recent work reported in [20], additional investigations are necessary to compare the two different U-Slot design approaches, *i.e.*, in section VII and [20, sec. III]. This comparison needs to be carried out with special emphasis on high permittivity substrates  $\epsilon_r \geq 6.0$ .

As mentioned earlier, this empirical design technique is limited because of symmetries associated with U-slot topologies. While the dimensional invariance and empirical formulas initiate a design, the complete process doesn't provide any analytical insight into the electromagnetic behavior of the antenna. Recent investigations [19],[20] on U-Slot design and performance modeling, suggest the need for analytical development. To eliminate this present limitation, efforts to develop an analytical formulation - based on the generalized cavity [1, pp. 97-102] and multipoint network [1, pp. 103-108] models - are under consideration. The main objective of such a future effort would be to develop/derive semi-rigorous formulas that are far less empirical in nature than that presented here. Such effort would also be aimed at providing information on the nature of currents flowing on the patch surface, and slot resonance(s). There is some information on slot resonance in [9] and [10], but they appear valid for low-permittivity substrates.

#### IX. CONCLUSION

Earlier investigations have shown that introducing an U-shaped slot on the radiating surface of a probe-fed, rectangular microstrip patch antenna, on a single layer substrate, resulted in ultra-wideband topologies with better than 10 dB return loss performance. Since most of the published results on U-slot were for foam or air substrates, and no systematic design procedure was available, a technique has been proposed in this paper for the design of such a class of wideband microstrip antennas on low to high permittivity microwave substrates. By examining the earlier data for U-slots, the key feature of dimensional invariance was established, and empirical equations have been derived based on data obtained from extensive (IE3D) simulations. Subsequently, a systematic design procedure, for rapid parametric simulation and design of U-slot patch antennas, has been proposed incorporating the two above-mentioned features. Using this proposed technique, VSWR and boresight ( $\phi = 0^\circ$  and  $\theta = 0^\circ$ ) gain comparisons were performed for the unoptimized and optimized U-Slot topologies. The results suggest that initial designs for U-slots that can be optimized within a few iterations via parametric simulations or state-of-art microstrip antenna analysis CAD tools, such as IE3D or ENSEMBLE.

#### ACKNOWLEDGEMENT

This work was largely supported in parts through several research contracts from Honeywell Federal Manufacturing and Technologies, KC, MO, and, the University Missouri Research Board (UMRB). In addition, the authors wish to thank Richard D. Swanson, Senior Staff Engineer, Honeywell Federal Manufacturing and Technologies, KC, MO, for his continued active interest in this work, and to Dr. Jian-X. Zheng of Zeland Corp., Fremont, CA, for many useful hints and clarifications regarding the IE3D software. Finally, the authors thank

Ms. Julie Burchett with Rogers Corp., Chandler, AZ, for supplying TMM and Ultralam substrate samples.

#### REFERENCES

- [1] R. Garg, P. Bhartia, I. Bahl and A. Ittipiboon, *Microstrip Antenna Design Handbook*. Norwood, MA, USA: Artech House, Inc., 2001.
- [2] K. Fujimoto and J. R. James, *Mobile Antenna Systems Handbook* (2<sup>nd</sup> ed.). *ibid.*,
- [3] K.-L. Wong, *Compact and Broadband Microstrip Antennas*. NY, USA: John-Wiley & Sons, Inc., 2002.
- [4] T. Huynh and K.-F. Lee, "Single-Layer Single Patch Wideband Microstrip Antenna," *Electronics Letters*, vol. 31, no. 16, pp. 1310-1312, August, 1995.
- [5] K.-F. Lee, K.-M. Luk, K.-F. Tong, S.-M. Shum, T. Huynh & R. Q. Lee, "Experimental and Simulation Studies of the Coaxially Fed U-Slot Rectangular Patch Antenna," *IEEE Proc. Microw. Antennas Propag.*, part H, vol. 144, no. 5, pp. 354-358, October 1997.
- [6] Y. L. Chow, Z.-N. Chen, K.-F. Lee & K.-M. Luk, "A Design Theory on Broadband Patch Antennas with Slot," *1998 IEEE AP Symposium Digest*, vol. 2, pp. 1124-1127, Atlanta, GA, June 21-26, 1998.
- [7] M. Clenet and L. Shafai, "Multiple Resonances and Polarisation of U-Slot Patch Antenna," *Electronics Letters*, vol. 35, no. 2, pp. 101-103, January 21, 1999.
- [8] K.-F. Tong, K.-M. Luk, K.-F. Lee and R. Q. Lee, "A Broad-Band U-Slot Rectangular Patch Antenna on a Microwave Substrate," *IEEE Trans. Antennas Propagat.*, vol. 48, no. 6, pp. 954-960, June 2000.
- [9] R. Bhalla and L. Shafai, "Resonance Behavior of Single U-Slot and Dual U-Slot Antenna," *2001 IEEE AP-S Symposium Digest*, vol. 2, pp. 700-703, Boston, June 2001.
- [10] R. Bhalla and L. Shafai, "Resonance Behavior of Single U-slot Microstrip Patch Antenna," *Microwave and Optical Technology Letters*, v. 32, no. 5, pp. 333-335, March 5, 2002.
- [11] A. K. Shackelford, K.-F. Lee, K.-M. Luk and R. C. Chair, "U-Slot Patch Antenna with Shorting Pin," *Electronics Letters*, vol. 37, no. 12, pp. 729-730, June 7, 2001.
- [12] A. Shackelford, K.-F. Lee, D. Chatterjee, Y.-X. Guo, K.-M. Luk and R. C. Chair, "Small Size Wide-Bandwidth Microstrip Patch Antenna," *2001 IEEE AP-S Symposium Digest*, vol. 1, pp. 86-89, Boston, June 2001.
- [13] Y.-X. Guo, A. Shackelford, K.-F. Lee and K.-M. Luk, "Broadband Quarter-Wavelength Patch Antennas with a U-shaped Slot," *Microwave and Optical Technology Letters*, v. 28, no. 5, pp. 328-330, March 5, 2001.
- [14] K.-F. Tong, K.-M. Luk and K.-F. Lee, "Wideband  $\Pi$ -shaped Aperture-Coupled U-Slot Patch Antenna," *Microwave and Optical Technology Letters*, v. 28, no. 1, pp. 70-72, January 5, 2001.
- [15] Y. X. Guo, K. M. Luk, K.-F. Lee and Y. L. Chow, "Double U-Slot Rectangular Patch Antenna," *Electronics Letters*, vol. 34, no. 19, pp. 1805-1806, Sept. 17, 1998.
- [16] M. Clenet, C. B. Ravipati and L. Shafai, "Bandwidth Enhancement of U-Slot Microstrip Antenna Using a Rectangular Stacked Patch," *Microwave and Optical Technology Letters*, v. 21, no. 6, pp. 393-395, June 20, 1999.
- [17] Y.-X. Guo, K.-M. Luk, K.-F. Lee and R. Chair, "A Quarter-Wave U-Slot Patch Antenna with Two Unequal Arms for Wideband and Dual-Frequency Operation," *IEEE Trans. Antennas Propagat.*, vol. 50, no. 8, pp. 1082-1087, August 2002.
- [18] B.-L. Ooi, S. Qin and M.-S. Leong, "Novel Design of Broad-Band Stacked Patch Antenna," *IEEE Trans. Antennas Propagat.*, vol. 50, no. 10, pp. 1391-1395, October 2002.
- [19] A. K. Shackelford, K.-F. Lee and K. M. Luk, "Design of Small-Size Wide-Bandwidth Microstrip-Patch Antennas," *IEEE Antennas and Propagation Magazine*, vol. 45, no. 1, pp. 75-83, February 2003. (See also *IEEE Antennas and Propagation Magazine*, vol. 45, no. 2, p. 58, April 2003 for corrections.)
- [20] S. Weigand, G. H. Huff, K. H. Pan and J. T. Bernhard, "Analysis and Design of Broad-Band Single-Layer Rectangular U-Slot Microstrip Patch Antennas," *IEEE Trans. Antennas Propagat.*, vol. 51, no. 3, pp. 457-468, March 2003.
- [21] R. A. Sainati, *CAD of Microstrip Antennas for Wireless Applications*. Norwood, MA, USA: Artech House, Inc., 1996.

- [22] Jian-X. Zheng, "A 3-D Electromagnetic Simulator for High-Frequency Applications," *IEEE Trans. on Components, Packaging and Manufacturing Technology Part-B*, vol. 18, no. 1, pp. 112-118, February 1995.
- [23] ———, "Three Dimensional Electromagnetic Simulation of Electronic Circuits of General Shape," *International Journal of Microwave and Millimeter-Wave Computer-Aided Engineering*, vol. 4, no. 4, pp. 384-395, 1994.
- [24] Zeland Software, Inc., *IE3D User's Manual*. Release(s) 7.0, 8.0 & 9.0. Fremont, CA, USA.
- [25] E. K. Miller, "Characterization, Comparison and Validation of Electromagnetic Modeling Software," *ACES Journal*, vol. 3, no. 2, pp. 8-24, 1989.
- [26] ———, "Development of EM Modeling Software Performance Standards," 1988 *IEEE AP-S Symposium Digest*, vol. 3, pp. 1340-1343, June 6-10, 1988.
- [27] D. M. Pozar, S. Duffy, S. Targonski and N. Herscovici, "A Comparison of Commercial Software Packages for Microstrip Antenna Analysis," 2000 *IEEE AP-S Symposium Digest*, vol. 1, pp. 152-155, Salt Lake City, UT, July 16-21, 2000.
- [28] K.-F. Lee, "Design and Simulation of Miniature Wideband U-slot and L-Probe Microstrip Patch Antennas,"; Part I of "Simulation, Design and Development of Miniature, Broadband, Low-Profile Antennas for Cellular and PCS Communications"; technical report ECE-UMKC00-HNYWL-TR01, prepared under contract for Honeywell Federal Manufacturing and Technologies, KC, MO, ECE Division, SICE, UMKC, September 2000.
- [29] V. Natarajan and D. Chatterjee, "An Empirical Design Technique for U-Slot Microstrip Patch Antennas on Microwave Substrates; Part-I: Infinite Ground Plane Analysis," technical report ECE-UMKC02-HNYWL-TR01, *ibid.*, September 2002.
- [30] Venkataraman Natarajan, "Some Design and Modeling Aspects of a Class of Wideband Microstrip Antennas Using Commercially Available CAD Softwares," M.S. Thesis, EE Department, University of Missouri, Columbia, MO, December 2002.



Student award in April 2001. He has been an IEEE Student Member since August 1998.

**Venkataraman Natarajan** was born in Chennai, India on July 2, 1978. He received his M.S. and B.S. degrees in Electrical Engineering from the University of Missouri-Columbia, USA, and University of Madras, Chennai, India, in 2002 and 2000, respectively. From August 2000 he has been working as a Graduate Research Assistant at the Computational Electromagnetics Laboratory at the University of Missouri-Kansas City. He was awarded the Outstanding Graduate



the Department of Electrical Engineering and Computer Science, University of Kansas, Lawrence, USA in 1998. From 1983-1986 he worked with the Antenna Group at Hindustan Aeronautics Limited (HAL), Hyderabad, India, on monopulse feeds for applications to the Fire Control Radar. Since August 1999 he is an Assistant Professor with the Electrical and Computer Engineering, University of Missouri Kansas City (UMKC). His research interests are in analytical and numerical techniques in electromagnetics, with an emphasis on high-frequency (asymptotic) applications, performance modeling of adaptive (smart) and phased array antennas, and electromagnetic effects in biological systems. Dr. Chatterjee is a member of the IEEE Antennas and Propagation Society, and reviewer for the *IEEE Transactions on Antennas and Propagation*, *IEEE Antennas and Wireless Propagation Letters* and *Radio Science*.

**Deb Chatterjee** received B.E.Tel.E (Bachelor's) degree in Electronics and Telecommunication Engineering from Jadavpur University, Calcutta, India, in 1981, M.Tech (Master's) degree in Electronics and Electrical Communication Engineering from IIT Kharagpur, India, in 1983, M.A.Sc (Master of Applied Science) degree in Electrical and Computer Engineering from Concordia University, Montreal, Canada, in 1992, and, the Ph.D. degree in Electrical Engineering from



## UTILIZING PARTICLE SWARM OPTIMIZATION IN THE FIELD COMPUTATION OF NON-LINEAR MAGNETIC MEDIA

A.A. Adly<sup>1</sup> and S.K. Abd-El-Hafiz<sup>2</sup>

<sup>1</sup>Cairo University, Electrical Power and Machines Department, Giza, 12211, Egypt

<sup>2</sup>Cairo University, Department of Engineering Mathematics, Giza, 12211, Egypt

### Abstract

It is well known that the computation of magnetic fields in nonlinear magnetic media may be carried out using various techniques. In the case of problems involving complex geometries or magnetic media, numerical approaches become especially more appealing. The purpose of this paper is to present an automated particle swarm optimization approach using which field computations may be carried out, via energy minimization, in devices involving nonlinear magnetic media. The approach has been implemented and simulations were carried out for different device configurations. It is found that the computations obtained using the proposed approach are in good qualitative and quantitative agreement with those obtained using the finite-element approach. Details of the proposed approach, simulations and comparisons with finite element results are given in the paper.

### I. INTRODUCTION

It is known that magnetic field computation in nonlinear magnetic media may be carried out using various techniques (refer, for instance, to [1,2]). Obviously, for cases involving complex geometries and/or magnetic media, numerical and artificial intelligence approaches become especially more appealing (see, for example, [3,4]).

Irrespective of the adopted approach, geometrical domain subdivision is usually performed and local magnetic quantities are considered. One way to obtain an electromagnetic field solution is through the minimization of the problem's energy functional, which may take complicated non-quadratic forms. The purpose of this paper is to present an automated particle swarm optimization (PSO) approach [5,6] using which 2-D field computations may be carried out in devices involving nonlinear magnetic media. More specifically, the magnetic energy functional is first formulated in terms of the unknown magnetic vector potentials corresponding to the discretization scheme.

A swarm of particles, each designated by a position vector that represents the unknown potentials, is initially randomly generated. These position vectors may be regarded as potential solutions to the energy minimization problem. The swarm is repeatedly moved

(i.e., modified) by the optimization algorithm and, upon convergence, the unknown magnetic vector potentials are found. Consequently, the field distribution is computed everywhere.

Among the advantages of the proposed approach are its simplicity, ability to handle complex magnetic media and computational efficiency. The proposed approach has been implemented and computations were carried out for different electromagnetic device configurations. These computations showed good qualitative and quantitative agreement with results obtained using the finite-element (FE) approach. Details of the approach, computations and comparisons with results obtained using the FE approach are given in the following sections.

### II. PROBLEM FORMULATION

In general, 2-D electromagnetic field problems may be reduced into 1-D problems using the following well-known magnetic vector potential  $A\bar{u}_z$  formulation:

$$\bar{B} = \mu\bar{H} = (\nabla \times A\bar{u}_z), \quad (1)$$

where  $\mu$  is the permeability,  $\bar{u}_z$  is a unit vector orthogonal to the problem plane,  $\bar{H}$  is the magnetic field vector and  $\bar{B}$  is the magnetic flux density vector.

For nonlinear media, the magnetostatic energy functional  $E$  may be expressed in the form:

$$E = \int_{\Omega} \left\{ \int_0^{|\bar{B}|} \gamma b \, db - JA \right\} d\Omega, \quad (2)$$

where  $\Omega$  represents the problem domain area,  $\gamma$  is the reciprocal of the magnetic permeability (i.e.,  $\gamma = \mu^{-1}$ ), and  $J$  is the current density along  $\bar{u}_z$ .

Neglecting hysteresis effects, the  $B$ - $H$  relation of most non-linear magnetic materials, especially those used in electromagnetic power devices, may be reasonably approximated by:

$$\bar{B} \approx C \sqrt[2]{|\bar{H}|} \bar{e}_H \text{ and } \bar{H} \approx \left( \frac{|\bar{B}|}{C} \right)^n \bar{e}_B, \quad (3)$$

where,  $n$  is an odd number,  $C$  is a constant while  $\bar{e}_H$  and  $\bar{e}_B$  are unit vectors along the field and flux density directions, respectively.

By subdividing the problem domain into finite magnetic and nonmagnetic regions, and from expressions (1)-(3), the magnetostatic energy formulation becomes:

$$E \approx \sum_{r=1}^{P_m} \left\{ \int_0^{|\nabla \times A_r|} \left( \frac{b^{n+1}}{C^n} \right) db - J_r A_r^{av} \right\} \Delta \Omega_r + \sum_{r=1}^{P_{nm}} \left\{ \frac{|\nabla \times A_r|^2}{2\mu_o} - J_r A_r^{av} \right\} \Delta \Omega_r \quad (4)$$

where,  $A_r^{av}$  is the average value of the magnetic vector potential within the  $r^{th}$  subdivision,  $\Delta \Omega_r$  is the area of the  $r^{th}$  subdivision,  $\mu_o$  is the permeability of free space, while  $P_m$  and  $P_{nm}$  represent the number of magnetic and non-magnetic domain subdivisions.

In the case when triangular domain subdivisions are adopted, the value of the vector potential within the  $r^{th}$  subdivision may obviously be expressed by:

$$A_r(x, y) = \alpha_{r0}(A_{r1}, A_{r2}, A_{r3}) + \alpha_{rx}(A_{r1}, A_{r2}, A_{r3})x + \alpha_{ry}(A_{r1}, A_{r2}, A_{r3})y, \quad (5)$$

where  $\alpha_{r0}$ ,  $\alpha_{rx}$  and  $\alpha_{ry}$  are constants within the  $r^{th}$  triangular subdivision and may be formulated in terms of the vector potential values at its three vertices (i.e.,  $A_{r1}, A_{r2}, A_{r3}$ ).

Hence, from (1) and (5), corresponding flux density components can be written in the form:

$$\left\{ \begin{array}{l} B_{rx} = +\alpha_{ry}(A_{r1}, A_{r2}, A_{r3}) \\ B_{ry} = -\alpha_{rx}(A_{r1}, A_{r2}, A_{r3}) \\ |\bar{B}_r| = \sqrt{\alpha_{rx}^2(A_{r1}, A_{r2}, A_{r3}) + \alpha_{ry}^2(A_{r1}, A_{r2}, A_{r3})} \end{array} \right\}. \quad (6)$$

Substituting (6) into (4), we obtain:

$$E \approx \sum_{r=1}^{P_m} \left\{ \frac{(\alpha_{rx}^2(A_{r1}, A_{r2}, A_{r3}) + \alpha_{ry}^2(A_{r1}, A_{r2}, A_{r3}))^{(n+2)/2}}{(n+2)C^n} - J_r \frac{(A_{r1} + A_{r2} + A_{r3})}{3} \right\} \Delta \Omega_r + \sum_{r=1}^{P_{nm}} \left\{ \frac{(\alpha_{rx}^2(A_{r1}, A_{r2}, A_{r3}) + \alpha_{ry}^2(A_{r1}, A_{r2}, A_{r3}))}{2\mu_o} - J_r \frac{(A_{r1} + A_{r2} + A_{r3})}{3} \right\} \Delta \Omega_r. \quad (7)$$

It turns out that obtaining a solution of a magnetostatic field problem involving non-linear magnetic media should always correspond to a minimization of expression (7). In this work, obtaining the solution is achieved through the utilization of the PSO approach to directly search for the appropriate vector potential values as explained in the following section.

### III. ENERGY MINIMIZATION USING PARTICLE SWARM OPTIMIZATION

Particle Swarm Optimization (PSO) is an evolutionary computation technique, which simulates the social behavior of insect swarms or bird flocks. Different from traditional search algorithms, such an evolutionary computation technique works on a population of potential solutions of the search space. Through cooperation and competition among the potential solutions, this technique is suitable for finding global optima in complex optimization problems [5].

The idea of our PSO implementation is that the whole swarm proceeds in the direction of the swarm member with the best fitness in a more or less stochastic way. A swarm consists of several particles  $M$ , where each particle keeps track of its own attributes. The most important attribute of each particle is its current position as given by an  $N$ -dimensional vector  $A^k = (A_1^k, A_2^k, \dots, A_N^k)$ , corresponding to a potential solution of the function to be minimized.

Along with the position, each particle has a current velocity,  $v^k = (v_1^k, v_2^k, \dots, v_N^k)$ , keeping track of the speed and direction in which the particle is currently traveling. Each particle also has a current fitness value, which is obtained by evaluating the objective function at the particle's current position. Additionally, each particle remembers its own personal best position,  $p^k = (p_1^k, p_2^k, \dots, p_N^k)$ . At the swarm level, the best overall position among all particles,  $p^g$ , is also recorded. The index of the best particle is represented by the symbol  $g$ . Upon termination of the algorithm;  $p^g$  will serve as the solution.

During each epoch, every particle is accelerated towards its own personal best as well as in the direction of the global best position. This is achieved according to the following two expressions [6].

$$v_i^k = w \times v_i^k + c_1 \times rand1() \times (p_i^k - A_i^k) + c_2 \times rand2() \times (p_i^g - A_i^k), \quad (8)$$

$$A_i^k = A_i^k + v_i^k, \quad (9)$$

where  $k = 1, \dots, M$ ,  $i = 1, \dots, N$ ,  $c_1$  and  $c_2$  are two

positive constants,  $rand1()$  and  $rand2()$  are two random functions in the range  $[0, 1]$ , while  $w$  is the inertia weight. Expression (8) is used to calculate the particle's new velocity according to its previous velocity and the distances of its current position from its own best experience (position) and the group's best experience. If the velocity is higher than a certain limit,  $v_{max}$ , this limit will be used as the new velocity for this particle in this dimension. Thus, keeping the particles within the search space. Then, the particle flies toward a new position according to expression (9).

A number of factors affect the performance of the PSO. First, the number of particles in the swarm,  $M$ , affects the runtime significantly. A balance between variety (more particles) and speed (fewer particles) must be considered. Another factor is the maximum velocity parameter,  $v_{max}$ , which controls the maximum global exploration ability PSO can have. A very large value for this parameter can result in oscillation. On the other hand, a small value can cause the particle to become trapped in local minima. The inertia weight,  $w$ , is employed to control the impact of the previous history of velocities on the current velocity. Thus, it influences the trade-off between global and local exploration abilities of the particles. A larger inertia weight facilitates global exploration and the search of new areas. A smaller inertia weight tends to facilitate local exploration to fine-tune the current search area. Suitable selection of the inertia weight can provide a balance between global and local exploration abilities [6].

For the implementation used in this paper, the number of particles,  $M$ , has been set equal to 35. The maximum velocity,  $v_{max}$ , is set to a constant value, which is equal to half the size of the search domain. The inertia weight is used to attenuate the magnitude of the velocity updates over time. This attenuation is a linear function of the current epoch number. Thus,  $w$  linearly decays from about 0.52 to 0.48. The constants  $c_1$  and  $c_2$  are set to the default value of 2.

#### IV. NUMERICAL IMPLEMENTATION AND SIMULATION RESULTS

The proposed approach has been implemented and computations were carried out for three different electromagnetic device configurations. Throughout the simulations, comparisons were made with computational results obtained using the Quickfield FE package (Version 4.3) and the core nonlinear  $B-H$  relation was assumed as shown in Fig. 1. As can be seen from the same figure, this relation was reasonably approximated using expression (3) by choosing  $n = 3$  and  $C = \frac{1.24}{\sqrt[3]{400}}$ .

First, simulations were carried out, using the proposed PSO approach, for an electromagnet having length, width, depth and air-gap length of 1.0m, 1.0m, 0.25m and 0.1m, respectively. Magnetic field and current density distributions were investigated subject to coil excitations corresponding to current densities of  $1.5 \times 10^6 \text{ A/m}^2$  and  $0.75 \times 10^6 \text{ A/m}^2$ . These excitations were chosen to drive the core in the initially linear and nonlinear magnetization ranges. Beside giving an idea about the relative dimensions of the coil in comparison with the core, Figs. 2-5 demonstrate the simulation results. In these figures a vector is plotted at the center of every triangular sub-domain. In other words, the figures give also information about the discretization scheme.

In order to check the accuracy of the proposed approach, computations were compared to FE identical simulations. This comparison revealed good qualitative and quantitative agreement. For instance, maximum flux density obtained using the FE approach for the high and low excitation levels were found to be 1.13 T and 0.59 T, respectively. Furthermore, Figs. 6-7 demonstrate the extent to which results obtained using the proposed approach match FE computations.

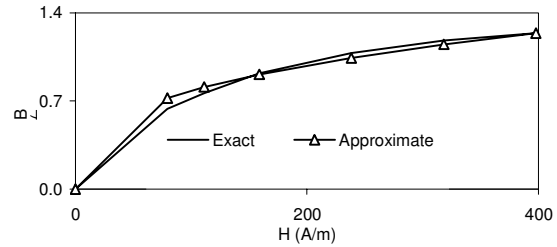


Fig.1. Assumed exact  $B-H$  properties and its approximation using expression (3).

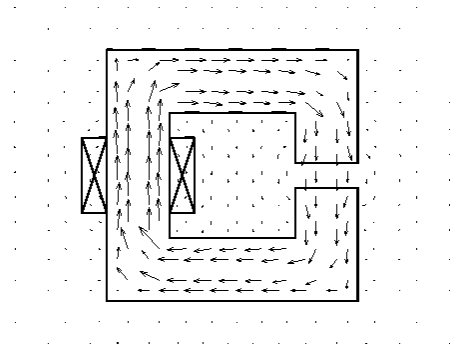


Fig.2. Flux density distribution obtained using the proposed PSO approach for the electromagnet subject to an excitation of  $1.5 \times 10^6 \text{ A/m}^2$  ( $B_{max} = 1.08 \text{ T}$ ).

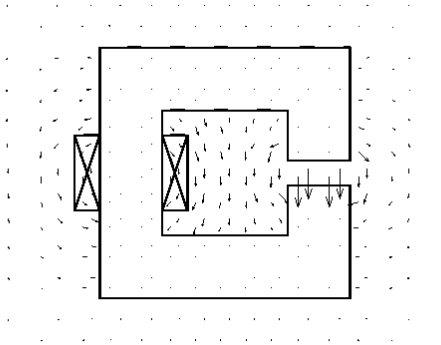


Fig.3. Magnetic field distribution obtained using the proposed PSO approach for the electromagnet subject to an excitation of  $1.5 \times 10^6 \text{ A/m}^2$ .

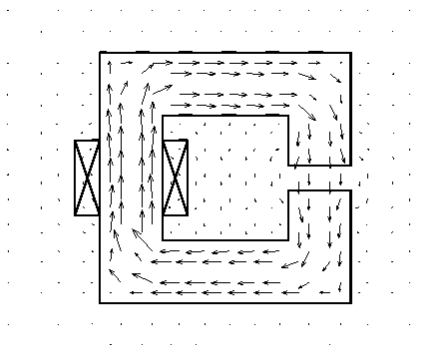


Fig.4. Flux density distribution obtained using the proposed PSO approach for the electromagnet subject to an excitation of  $0.75 \times 10^6 \text{ A/m}^2$  ( $B_{\text{max}} = 0.55 \text{ T}$ ).

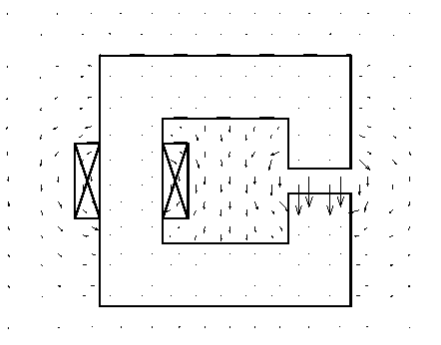


Fig.5. Magnetic field distribution obtained using the proposed PSO approach for the electromagnet subject to an excitation of  $0.75 \times 10^6 \text{ A/m}^2$ .

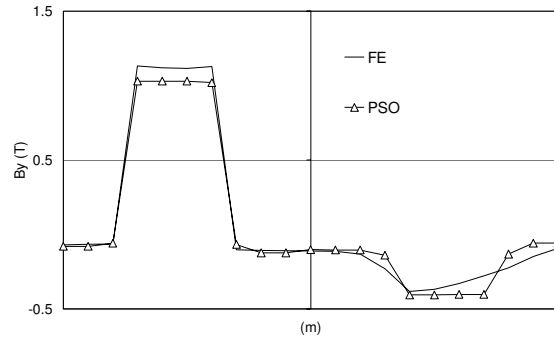


Fig.6. Comparison between PSO and FE computations for the particular horizontal contour line located at the center of the electromagnet window.

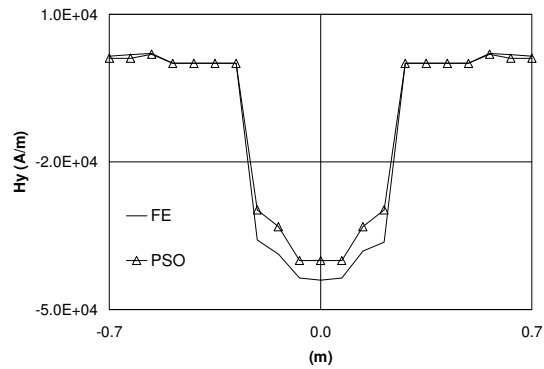


Fig.7. Comparison between PSO and FE computations for the particular vertical contour line located at the center of the electromagnet window.

Second, simulations were carried out for an electromagnetic actuator having window dimensions, depth, core opening, and plunger dimensions of  $0.8\text{m} \times 0.9\text{m}$ ,  $0.2\text{m}$ ,  $0.50\text{m}$  and  $1.0\text{m} \times 0.4\text{m}$ , respectively. Once more, magnetic field and current density distributions were investigated for; case#1 when the plunger is in contact with the core and, case#2 when it is  $0.1\text{m}$  apart. Excitation was kept constant corresponding to a current density of  $3 \times 10^5 \text{ A/m}^2$ . Due to the symmetry of this configuration, results of these distributions are only given in the right half of the solution domain as demonstrated by Figs. 8-11. Again, these figures give some information about the adopted discretization scheme as well as the relative coil to core dimensions. Figs. 12-13, on the other hand, reveal the good agreement between results obtained using the proposed PSO approach and those obtained through the FE technique. It should also be mentioned that, using the FE technique, the maximum flux density values were found to be  $1.16\text{T}$  for case#1 and  $0.311$  for case#2.

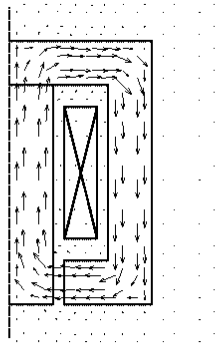


Fig.8. Flux density distribution obtained using the proposed PSO approach for the electromagnetic actuator when the plunger is in contact with the core ( $B_{max} = 1.12\text{T}$ ).

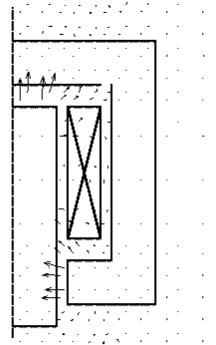


Fig.11. Magnetic field distribution obtained using the proposed PSO approach for the electromagnetic actuator when the plunger is 0.1m apart from the core.

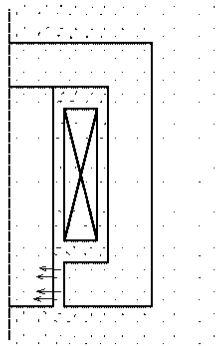


Fig.9. Magnetic field distribution obtained using the proposed PSO approach for the electromagnetic actuator when the plunger is in contact with the core.

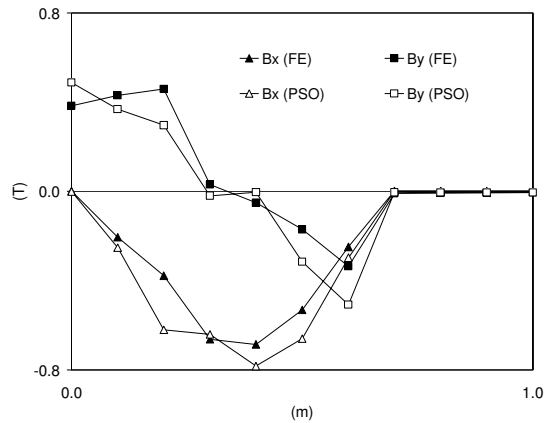


Fig.12. Comparison between PSO and FE computations for the particular horizontal contour line located at the center of the lower core yoke.

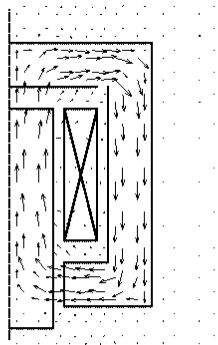


Fig.10. Flux density distribution obtained using the proposed PSO approach for the electromagnetic actuator when the plunger is 0.1m apart from the core ( $B_{max} = 0.296\text{T}$ ).

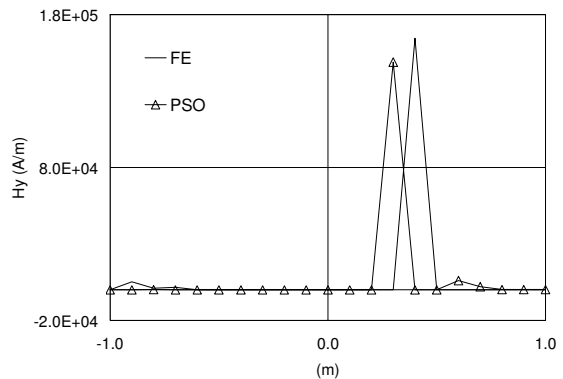


Fig.13. Comparison between PSO and FE computations for the particular vertical contour line located at the center line of the actuator.

Finally, simulations were carried out for a switched reluctance motor (SRM) whose data is given in Table I. Particular attention was given to the flux density and field distributions at the beginning and end of a stepping phase. Such distributions, driven by a pair of coil excitation corresponding to a current density of  $3 \times 10^5 \text{ A/m}^2$ , are given in Figs. 14-17. Obviously, these figures give some information about the adopted discretization scheme. In these figures, only steady state analysis was considered and no motion effects were incorporated. In addition, the flux was assumed to be confined inside the motor (i.e., no flux is assumed to cross the outer stator and inner rotor diameters. Additional comparisons with results obtained using the FE technique are given in Figs. 18 and 19. It is also worth mentioning that the maximum flux density values computed using the FE technique at the beginning and end of the stepping phase were found to be 0.08 T and 1.08 T, respectively.

TABLE I  
Data of the simulated Switched Reluctance Motor

Number of Stator Poles	8
Number of Rotor Poles	6
Stator Pole Arc	15°
Rotor Pole Arc	15°
Stator Core Outer Diameter	0.100 m
Stator Core Inner Diameter	0.750 m
Diameter at Stator Pole	0.450 m
Diameter at Rotor Pole	0.445 m
Rotor Core Outer Diameter	0.250 m
Rotor Core Inner Diameter	0.150 m

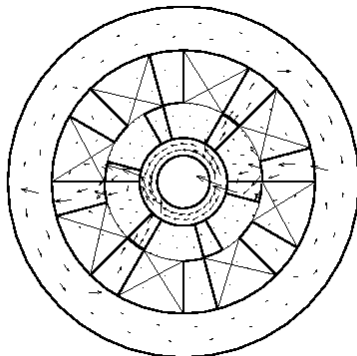


Fig.14. Flux density distribution obtained using the proposed PSO approach for the SRM at the beginning of a stepping phase ( $B_{\max} = 0.07 \text{ T}$ ).

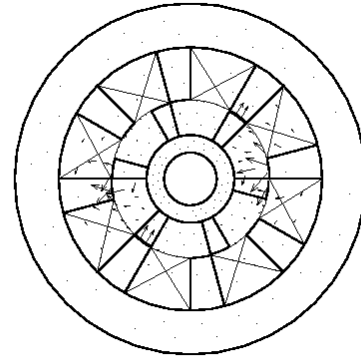


Fig.15. Magnetic field distribution obtained using the proposed PSO approach for the SRM at the beginning of a stepping phase.

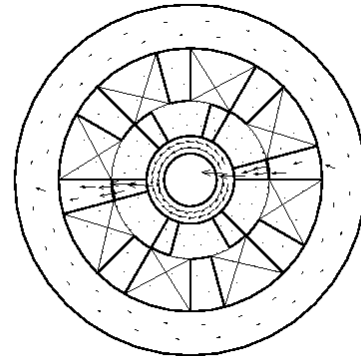


Fig.16. Flux density distribution obtained using the proposed PSO approach for the SRM at the end of a stepping phase ( $B_{\max} = 1.13 \text{ T}$ ).

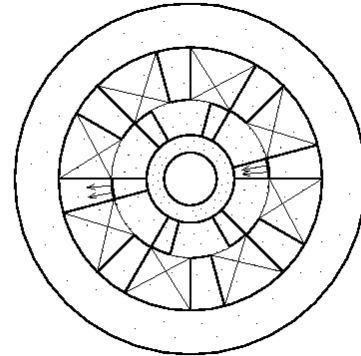


Fig.17. Magnetic field distribution obtained using the proposed PSO approach for the SRM at the end of a stepping phase.

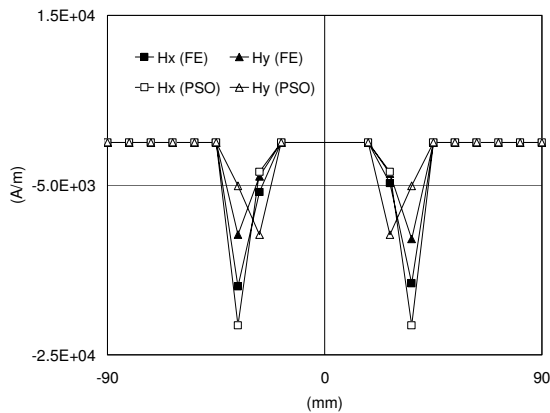


Fig.18. Comparison between PSO and FE computations for the contour line passing through the centers of the two energized stator poles at the beginning of the stepping phase.

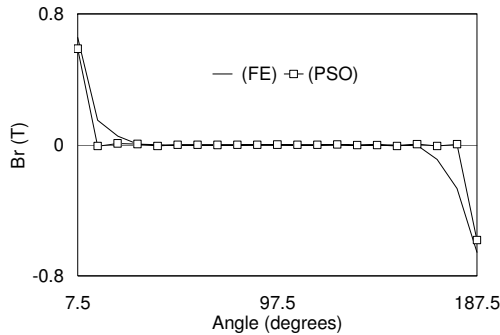


Fig.19. Comparison between PSO and FE computations for the contour arc located in the center of the air-gap and subtending one energized stator pole to the other at the end of the stepping phase.

#### IV. DISCUSSION AND CONCLUSIONS

In light of the proposed PSO approach as well as the experience gained while performing the presented simulations, the following few remarks should be stressed:

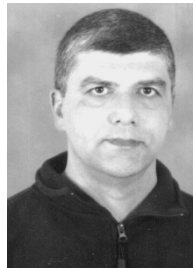
- Depending on the problem nature and number of unknowns, suitable values for the number of particles  $M$  and inertia weight  $w$  should be first investigated. In our case it took some time to decide upon using the reported  $M$  and  $w$  values. Once this sort of tuning is achieved, the proposed approach gives reasonable results in computational time comparable to that of the FE technique.
- It can be observed from the presented results that good agreement with FE computations can be achieved using the proposed approach. It should be pointed out, however, that some of the discrepancies between results of both techniques

- stem from the non-identical discretization schemes.
- An important feature of the proposed search approach is its simplicity and ability to handle adjacent discretizations of dramatically different dimensions without the risk of running into numerical difficulties related to matrix inversion. This further highlights the computational memory-wise efficiency of the approach.

More efforts are planned to further investigate the proposed approach in different time harmonic problems. It should also be stressed that PSO has been previously used in device dimension optimization (see, for example, [7]). Coupling this capability to the proposed field analysis approach might pave the way towards the ability to simultaneously optimize the dimensions and compute fields in devices involving nonlinear media.

#### REFERENCES

- J.K. Sykulski, *Computational Magnetics*, Chapman & Hall, London, 1995.
- A.A. Adly and S.K. Abd-El-Hafiz, "Automated two-dimensional field computation in nonlinear magnetic media using Hopfield neural networks," *IEEE Trans. Magn.*, Vol. 38, pp. 2364-2366, 2002.
- M.V.K. Chari and S.J. Salon, *Numerical Methods in Electromagnetism*, Academic Press, San Diego CA, 2000.
- A.A. Adly and S.K. Abd-El-Hafiz, "Utilizing Hopfield neural networks in analysis of reluctance motors," *IEEE Trans. Magn.*, vol. 36, pp. 3147-3149, 2000.
- J. Kennedy and R. Eberhart, "Particle Swarm Optimization," *Proceedings of the IEEE International Conference on Neural Networks*, Perth, Australia, pp. 1942-1948, 1995.
- Y. Shi and R. Eberhart, "A Modified Particle Swarm Optimizer," *Proceedings of the IEEE International Conference on Evolutionary Computation*, Anchorage, Alaska, pp. 69-73, 1998.
- G. Ciuprina, D. Ioan and I. Munteanu, "Use of Intelligent-Particle Swarm Optimization in Electromagnetics," *IEEE Trans. Magn.*, vol. 38, pp. 1037-1040, 2002.



**Amr A. Adly** received the BS and MS degrees in Electrical Engineering from Cairo University, Egypt, in 1984 and 1987, respectively, and the PhD degree in Electrical Engineering from the University of Maryland, College Park, Maryland, USA, in 1992. In

1993 he joined LDJ Electronics, Troy, Michigan, USA, as a Senior Engineer/Scientist. In 1994, he was appointed as an Assistant Professor at the Electrical Power and Machines Department, Faculty of Engineering, Cairo University, Giza, Egypt. Since 1999, he has been working as an Associate Professor in the same department. His research interests include electromagnetics, modeling and simulation of complex magnetic materials, electrical machines, superconductivity, magnetic recording, magnetic measurement instrumentation, and magneto-hydrodynamics. In 1994, he received the Egyptian State Prize for achievements in Engineering Sciences. He has authored more than 60 journal and refereed conference papers. Dr. Adly is a senior member of the IEEE Magnetics Society and a member of the ACES Society.



**Salwa K. Abd-El-Hafiz** received the BS degree in Electrical Engineering from Cairo University, Egypt, in 1986 and the MS and PhD degrees in Computer Science from the University of Maryland, College Park, Maryland, USA, in 1990

and 1994, respectively. In 1994, she was appointed as an Assistant Professor at the Engineering Mathematics Department, Faculty of Engineering, Cairo University, Giza, Egypt. Since 1999, she has been working as an Associate Professor in the same department. Her research interests include software analysis and specification, software measurements, software reverse engineering, neural networks, evolutionary computation techniques, knowledge-based systems and numerical analysis. In 2001, she received the Egyptian State Prize for achievements in Engineering Sciences. Dr. Abd-El-Hafiz is a member of the IEEE Software Computer Society.



## AN APPROACH TO MULTI-RESOLUTION IN TIME DOMAIN BASED ON THE DISCRETE WAVELET TRANSFORM

C. Represa(\*), C. Pereira(\*), A.C.L. Cabeceira (\*\*), I. Barba (\*\*), J. Represa (\*\*)

(\*) Dpt. of Electromechanical Engineering. University of Burgos. 09001 Burgos. Spain.

Phone: +34 947258830 FAX: +34 947258831 E-Mail: [crepresa@ubu.es](mailto:crepresa@ubu.es)

(\*\*) Dpt. of Electricity and Electron. University of Valladolid. 47011 Valladolid. Spain.

Phone: +34 983423223 FAX: +34 983423225 E-Mail: [ibarba@ee.uva.es](mailto:ibarba@ee.uva.es)

**Abstract<sup>1</sup>.**- In this paper, an approach to multi-resolution in time domain (MRTD) is presented. Maxwell equations are discretized using finite differences in time and a derivative matrix in space that allows any desired level of spatial resolution. This derivative matrix acts on the coefficients that represent the expansion of the field components. These coefficients are calculated by means of the Discrete Wavelet Transforms (DWT). In this work hard (PEC and PMC) boundary conditions have been introduced into the algorithm using the method of images. This approach is valid for any kind of wavelet functions. Stability and dispersion properties are also investigated. Some numerical results, showing multi-resolution properties are presented.

**Keywords.**- Multi-resolution in time domain, MRTD, Daubechies wavelets, Discrete Wavelet Transform, DWT.

### 1.- Introduction

The development of electromagnetic fields in scale and wavelet functions [1], has given rise to the techniques known as Multi Resolution in Time Domain (MRTD). These techniques are based on the possibility of increasing the resolution of a signal, from a coarse level to a fine one, using low-resolution functions (scale functions), combined with others of intermediate resolution levels (wavelet functions). Different functions have been used in this type of analysis: Battle-Lemarie [2], Haar [3] or Daubechies [4].

In these techniques, the electric and magnetic field components of Maxwell's curl equations are represented by a manifold expansion in scale and wavelet functions with respect to space, and step functions with respect to time. The method of

moments [5] allows to obtain a set of equations similar to the one used in FDTD (identical, in the case of Haar functions, to the Yee's algorithm). Instead of the field values, the coefficients of this expansion are used in such scheme.

One of the points that affect the complexity of these schemes is the type of functions used for the expansion. For example, if Battle-Lemarié functions are used, an infinite number of coefficients must be used, because of the non-compact support of these functions. Actually, we can truncate the expansion and use a reduced number of them, obtaining an approximate solution. This problem does not appear when, for example, Haar functions are used, since they are compactly supported, so it is not necessary to truncate the expansion.

A second point is the desired resolution level for the solution of the problem. The above mentioned approaches [2-4] use scale functions for a first approximation of the fields; in this case simple functions are obtained, but, if an increasing of the resolution is desired, adding different levels of wavelet functions, the solution becomes unfeasible, as the scheme must be modified for every new level we add. This problem can be solved if a Discrete Wavelet Transform (DWT) is used to derive the coefficients of the expansions, as it has already been used to obtain the time domain solution of electrical networks [6]

In this work, compactly supported Daubechies wavelet functions [1] have been used to make an expansion of the fields. Its coefficients are computed through a Discrete Wavelet Transform. A derivative matrix, also obtained by means of a DWT, allows us to compute the value of the electric and magnetic fields at desired spatial positions and with the desired resolution. We have found the stability criterion of the algorithm for different wavelet functions and in some cases it is wider than the FDTD stability criterion for the

<sup>1</sup> This work was sponsored in part by the Spanish Ministry of Science and Technology, under its project TIC-2000-1612-C03-02.

same spatial resolution (twice in the case of Haar wavelet functions).

**2.- Formulation**

The simplest case of a TEM plane wave propagating in a homogeneous, linear, isotropic and non-dispersive media, with fields  $\mathbf{E}_x$  and  $\mathbf{H}_y$  is analyzed. Then, the equations to solve are:

$$\begin{aligned} \frac{\partial E_x}{\partial z} &= -\mu \frac{\partial H_y}{\partial t} \\ \frac{\partial H_y}{\partial z} &= -\varepsilon \frac{\partial E_x}{\partial t} \end{aligned} \quad (1)$$

In the proposed scheme, every field component is expanded in terms of scaling and wavelet functions, as shown in equation (2), where the coefficients of the lower resolution level ( $a_k^0$ ) are given by the scaling function ( $\phi$ ) and the coefficients of the successive resolution level ( $b_k^j$ ) are given by the wavelet functions ( $\psi$ ):

$$F^n(z) = \sum_k^n a_k^j \phi_k^j(z) = \begin{cases} \sum_k^n a_k^0 \phi_k^0(z) \\ + \sum_{j=1}^{J-1} \sum_k^n b_k^j \psi_k^j(z) \end{cases} \quad (2)$$

The spatial discretization is achieved by dividing the domain into  $N$  cells of size  $\Delta$ , as a starting point, then getting  $N$  sampling points in the center of each cell. This is what we call *resolution level 0* ( $j = 0$ ). If each cell is now divided into  $2^j$  points, the maximum level of desired resolution  $J$  ( $j = J$ ) is reached and then the simulation domain has  $N \cdot 2^J$

sampling points with a distance of  $\Delta z$  between them. This is illustrated in figure 1.

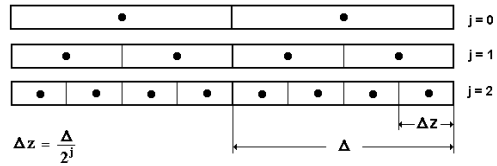


Fig. 1.- Spatial discretization for  $J=2$ .

The coefficients  $a_k^j$  are enough to represent the real values of the field at each sampling point and they are the initial and the final step of the decomposition process involved in the Discrete Wavelet Transform. The multi-resolution analysis performed with the wavelet transform can be understood as a digital filtering process where a signal is decomposed in two parts, one containing the low frequencies, the scale functions ( $\phi$ ), and other part containing the high frequencies, the wavelet functions ( $\psi$ ). The multi-resolution representation through the Discrete Wavelet Transform (DWT) is provided by successive filter banks stages, each one containing a low-pass and a high-pass filter, described in terms of the coefficients of their impulse responses  $L(m)$  and  $H(m)$  ( $m \in \mathbb{Z}$ ) respectively [1]. The filtering process means successive convolutions of the field and the filter coefficients followed by a decimation process that retains only the even indexes. The inverse transform (IDWT) consists in successive interpolations followed by convolutions that gives the field values using the coefficients of the previous decomposition. This is sketched in figure 2.

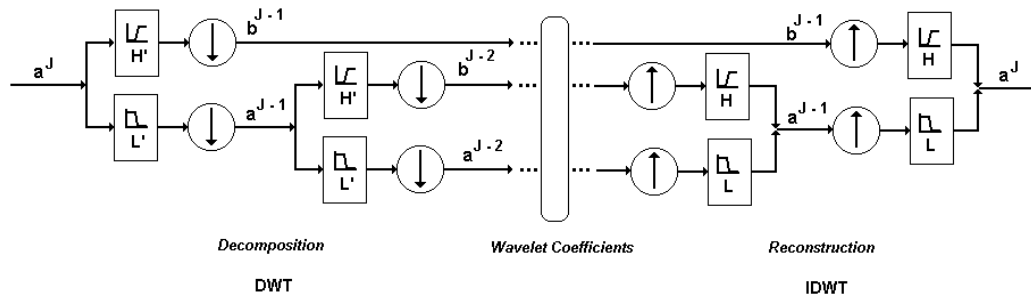


Fig. 2.- A step of the filtering process: the low and high-pass filters outputs the coefficients  $d$  and  $b^j$  respectively.

Then, eqs. (1) are discretized using centered finite differences for the time derivatives and a spatial derivative operator computed through a DWT matrix for the spatial derivatives. Each coefficient is, then, obtained from its values at the same point in a previous time step and from the derivation of

the other field coefficients at an intermediate time step:

$$\begin{aligned} H^{n+\frac{1}{2}} &= H^{n-\frac{1}{2}} - \frac{\Delta t}{\mu} \frac{1}{\Delta} \mathbf{D}^J (\mathbf{E})^n \\ \mathbf{E}^{n+1} &= \mathbf{E}^n - \frac{\Delta t}{\varepsilon} \frac{1}{\Delta} \mathbf{D}^J (\mathbf{H})^{n+\frac{1}{2}} \end{aligned} \quad (3)$$

where  $\Delta t$  and  $\Delta$  are the time and space steps respectively, and  $\mathbf{D}^J$  represents the spatial derivative operator of level  $J$ . This operator [7] acts on the coefficients  $a$  and  $b$  of the field transform (3) and it is denoted by a matrix  $\mathbf{D}$  [8] which can be computed previously. In this way, eqs. (3) can be rewritten as follows for an arbitrary level of resolution  $J$ :

$$\begin{aligned} \begin{bmatrix} \mathbf{E}^{\psi^j} \\ \mathbf{E}^{\phi^0} \end{bmatrix}^{n+1} &= \begin{bmatrix} \mathbf{E}^{\psi^j} \\ \mathbf{E}^{\phi^0} \end{bmatrix}^n - \frac{\Delta t}{\varepsilon} \frac{1}{\Delta} \mathbf{D}^J \begin{bmatrix} \mathbf{H}^{\psi^j} \\ \mathbf{H}^{\phi^0} \end{bmatrix}^{n+\frac{1}{2}} \\ \begin{bmatrix} \mathbf{H}^{\psi^j} \\ \mathbf{H}^{\phi^0} \end{bmatrix}^{n+\frac{1}{2}} &= \begin{bmatrix} \mathbf{H}^{\psi^j} \\ \mathbf{H}^{\phi^0} \end{bmatrix}^{n-\frac{1}{2}} - \frac{\Delta t}{\mu} \frac{1}{\Delta} \mathbf{D}^J \begin{bmatrix} \mathbf{E}^{\psi^j} \\ \mathbf{E}^{\phi^0} \end{bmatrix}^n \end{aligned} \quad (4)$$

where  $j=0, \dots, J-1$ . This matrix  $\mathbf{D}$  is banded with a limited band width, due to the compact support of the Daubechies wavelets, and this width increases as the size of the filters does. Its elements are integrals of the scaling and wavelet functions and its discrete spatial translations of the first derivative (eqs. (6.1)-(6.4)). Because of multi-resolution, this matrix can be decomposed in a set of submatrices of lower resolution, so if we have named the original matrix of highest resolution  $\mathbf{D}^J$ , it is constructed with the one level lower matrices  $\mathbf{A}$ ,  $\mathbf{B}$ ,  $\mathbf{\Gamma}$ ,  $\mathbf{D}$ , then:

$$\mathbf{D}^J = \begin{pmatrix} \mathbf{A}^{J-1} & \mathbf{B}^{J-1} \\ \mathbf{\Gamma}^{J-1} & \mathbf{D}^{J-1} \end{pmatrix} \quad (5)$$

where  $\mathbf{A}^j = \{\alpha_{ij}^j\}$ ,  $\mathbf{B}^j = \{\beta_{ij}^j\}$ ,  $\mathbf{\Gamma}^j = \{\gamma_{ij}^j\}$ ,  $\mathbf{D}^j = \{d_{ij}^j\}$ . The components of every matrix can be calculated in a recursive way, so:

$$\alpha_{ij}^j = 2^j \alpha_{i-1}^j \quad (6)$$

and similar expressions for the other coefficients,  $\beta$ ,  $\gamma$  and  $d$ . The expression  $\alpha_1$  is obtained by means of the following expression:

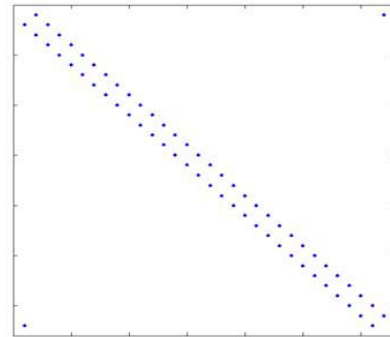
$$\alpha_1 = \int \psi(z-1) \cdot \frac{d}{dz} \psi(z) \cdot dz \quad (7)$$

Similar expressions, combining scale and wavelet functions can be used to calculate the other coefficients  $\beta$  (scale, wavelet),  $\gamma$  (wavelet and scale) and  $d$  (scale and scale). The scale and wavelet functions in every case are obtained by means of the low-pass and the high pass filters,  $L(m)$  and  $H(m)$  respectively:

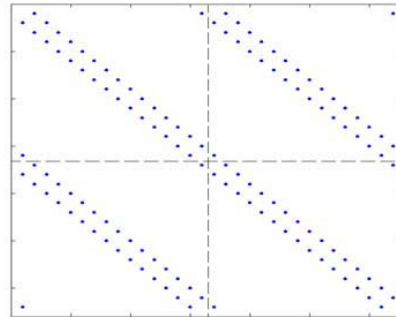
$$\phi(t) = \sum_{m=0}^{L_f-1} L(m) \sqrt{2} \phi(2t-m) \quad (8)$$

$$\psi(t) = \sum_{m=0}^{L_f-1} H(m) \sqrt{2} \phi(2t-m) \quad (9)$$

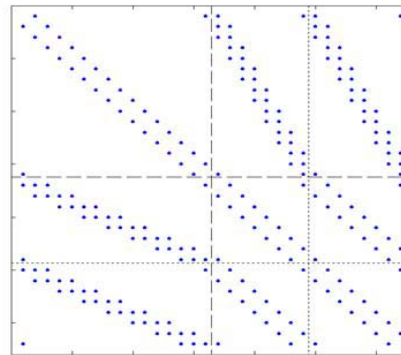
being  $L_f$  the filter length. In figure 3 three different aspects of the derivative matrix  $\mathbf{D}$  for three levels of resolution are depicted, where only the nonzero elements have been plotted.



(a)



(b)



(c)

Fig. 3.- Three different aspects of the derivative matrix  $\mathbf{D}^j$  for three resolution levels: (a)  $j=0$ , (b)  $j=1$ , (c)  $j=2$ .

The use of this derivative matrix allows us to achieve any level of resolution without modifications of the algorithm. Moreover, we can choose at the beginning of the simulation what type

of wavelet function is going to be used, and what regions of the simulation domain we want to solve at higher resolution. This feature will be shown further in the examples.

### 3.- Boundary conditions.

The derivative matrix  $\mathbf{D}$  is built-up in a cyclic form in such a way that it treats the coefficients on both boundaries as contiguous. It results in a cyclic space, that is, an infinite unbounded space. As the simulation domain is not cyclic at all, the character of the matrix must be modified. To do so, we propose to add adjacent columns with the elements related to the boundaries, and getting an *extended matrix*; i.e.

$$\{\alpha_{ij}\} = \begin{pmatrix} \alpha_0 & \alpha_{-1} & 0 & \alpha_1 \\ \alpha_1 & \alpha_0 & \alpha_{-1} & 0 \\ 0 & \alpha_1 & \alpha_0 & \alpha_{-1} \\ \alpha_{-1} & 0 & \alpha_1 & \alpha_0 \end{pmatrix}$$

↓

$$\{\alpha_{ij}\}_{\text{extended}} = \left( \begin{array}{cccc|cccc} \alpha_1 & \alpha_0 & \alpha_{-1} & 0 & 0 & 0 & 0 & 0 \\ 0 & \alpha_1 & \alpha_0 & \alpha_{-1} & 0 & 0 & 0 & 0 \\ 0 & 0 & \alpha_1 & \alpha_0 & \alpha_{-1} & 0 & 0 & 0 \\ 0 & 0 & 0 & \alpha_1 & \alpha_0 & \alpha_{-1} & 0 & 0 \end{array} \right)$$

and similar expressions for  $\{\beta\}$ ,  $\{\gamma\}$ , and  $\{d\}$ . The matrix  $\mathbf{D}$  acting on the column vector  $(\mathbf{b}^J, \mathbf{a}^J)$  at resolution level  $J$  implies that its extension must act on an extended vector too. The additional coefficients needed to represent the boundaries can be obtained using the method of images for PEC or PMC walls. If  $d'_L$  and  $b'_L$  are the scale and wavelet coefficients respectively, belonging to a border cell collocated at position  $\mathbf{z}=L\Delta\mathbf{z}$ , we obtain the additional coefficients  $a'$  and  $b'$  this way:

- for even symmetry:

$$\begin{cases} \mathbf{a}_{N+i}' = +\mathbf{a}_{N-i+1} \\ \mathbf{b}_{N+i}' = -\mathbf{b}_{N-i+1} \end{cases} \text{ on the right}$$

$$\begin{cases} \mathbf{a}_{1-i}' = +\mathbf{a}_i \\ \mathbf{b}_{1-i}' = -\mathbf{b}_i \end{cases} \text{ on the left}$$

- for odd symmetry:

$$\begin{cases} \mathbf{a}_{N+i}' = -\mathbf{a}_{N-i+1} \\ \mathbf{b}_{N+i}' = +\mathbf{b}_{N-i+1} \end{cases} \text{ on the right}$$

$$\begin{cases} \mathbf{a}_{1-i}' = -\mathbf{a}_i \\ \mathbf{b}_{1-i}' = +\mathbf{b}_i \end{cases} \text{ on the left}$$

These boundary conditions allow us to implement in a easy way infinite electric or magnetic walls.

More complex structures require more sophisticated techniques not studied here.

### 4.- Stability analysis

For the algorithm to be stable, the pair  $\Delta t$  and  $\Delta z$  must be chosen in a correct way. We choose these values following the derivation given in [9] where the stability problem is treated as an eigenvalue problem. This means that plane wave eigenmodes will be assumed to propagate in the numerical data space. The spectrum of eigenvalues for these modes due to the numerical space differentiation process will be determined and compared to the stable spectrum of eigenvalues determined by the numerical time differentiation process. By requiring the complete spectrum of spatial eigenvalues to be contained within the stable range, it is ensured that all possible numerical wave modes in the grid are stable. In this way, equations (1) can then be rewritten as follow:

$$\frac{H^{n+\frac{1}{2}} - H^{n-\frac{1}{2}}}{\Delta t} = -\frac{1}{\mu \cdot \Delta z} \sum_{\Gamma} d_i E_{i-1}^n \quad (10)$$

$$\frac{E^{n+1} - E^n}{\Delta t} = -\frac{1}{\varepsilon \cdot \Delta z} \sum_{\Gamma} d_i H_{i-1}^{n+\frac{1}{2}}$$

and this equations can be split into two eigenvalue problems concerning time and space:

$$\frac{H^{n+\frac{1}{2}} - H^{n-\frac{1}{2}}}{\Delta t} = \Lambda H_i^n \quad (11)$$

$$\frac{E^{n+1} - E^n}{\Delta t} = \Lambda E_i^{n+\frac{1}{2}}$$

$$-\frac{1}{\mu \cdot \Delta z} \sum_{\Gamma} d_i E_{i-1}^n = \Lambda H_i^n \quad (12)$$

$$-\frac{1}{\varepsilon \cdot \Delta z} \sum_{\Gamma} d_i H_{i-1}^{n+\frac{1}{2}} = \Lambda E_i^{n+\frac{1}{2}}$$

where only scaling functions of resolution level  $J=0$  have been used. To avoid having any mode increasing without limit during normal time-stepping it is found from equation (11) that the stable spectrum of eigenvalues is:

$$|\text{Im}(\Lambda)| \leq 2 / \Delta t \quad (13)$$

In order to solve equations (12) we introduce a typical mode of the spatial spectrum like (14) into the equations:

$$\begin{aligned} {}^n E_i &= E_0 e^{j(\bar{k}_i \Delta z)} \\ {}^n H_i &= H_0 e^{j(\bar{k}_i \Delta z)} \end{aligned} \quad (14)$$

Then we get the following set of equations:

$$\begin{aligned} -\frac{1}{\mu \cdot \Delta z} \sum_I d_I E_0 e^{j(\tilde{k}+\Delta z)} e^{j(-\tilde{k}+\Delta z)} &= \Lambda H_0 e^{j(\tilde{k}+\Delta z)} \\ -\frac{1}{\varepsilon \cdot \Delta z} \sum_I d_I H_0 e^{j(\tilde{k}+\Delta z)} e^{j(-\tilde{k}+\Delta z)} &= \Lambda E_0 e^{j(\tilde{k}+\Delta z)} \end{aligned} \quad (15)$$

Simplifying and using Euler's identity we get that the spatial eigenvalues are given by:

$$\text{Im}(\Lambda) = \frac{c}{\Delta z} \sum_I d_I \text{sen}(-kl\Delta z) \quad (16)$$

Therefore, the maximum value of this eigenvalues is:

$$|\text{Im}(\Lambda)| \leq \frac{c}{\Delta z} \sum_I |d_I| \quad (17)$$

To guarantee numerical stability, the range of spatial modes must be contained completely within the stable range of time-stepping eigenvalues set by (17) and so:

$$\frac{c}{\Delta z} \sum_I |d_I| \leq \frac{2}{\Delta t} \quad (18)$$

Therefore, the upper bound of the time step  $\Delta t_{\text{MRTD}}$  is:

$$\Delta t_{\text{MRTD}} \leq \frac{2}{\sum_I |d_I|} \frac{\Delta z}{c} \quad (19)$$

Defining a stability factor like (20):

$$s = \frac{c\Delta t_{\text{MRTD}}}{\Delta z} \quad (20)$$

equation (19) establishes that the stability factor must be contained within the range :

$$0 < s \leq \frac{2}{\sum_I |d_I|} \quad (21)$$

Depending on the type of wavelet function used, this range implies that the time step can be set to a different value for the same spatial resolution. If Haar wavelet functions are used, this value can be set double than the time step set in FDTD for the same spatial resolution.

## 5.- Dispersion properties

The use of numerical techniques for solving electromagnetic problems as TLM [10], FDTD or MRTD require always a discretization process. Such a process result in a phase error of the field

propagation, that is, the numerical phase velocity given by the algorithm differ from the phase velocity of the wave in the medium [11]. This fictitious dispersive behaviour must be taken into account specially in considering large structures of simulation because significant differences between real and numerical phase can be obtained. Some studies about dispersion properties of MRTD methods based on Galerkin procedures [12], [13] have been done. Now we proceed to study the dispersion characteristics of the MRTD algorithm based on the DWT using Daubechies' wavelets functions. To do that, a plane monochromatic travelling-wave (22) is introduced into the discretized Maxwell equations (4) and then we search for the relationship between the angular frequency  $\omega$  and the numerical wave number  $\tilde{k}$  :

$$\begin{aligned} {}^n E_i^\zeta &= E_0 e^{j(\tilde{k}\Delta z - \omega n \Delta t)} \\ {}^n H_i^\zeta &= H_0 e^{j(\tilde{k}\Delta z - \omega n \Delta t)} \end{aligned} \quad (22)$$

As starting point, we expand the field components using only scaling functions of resolution level  $\mathbf{J}=0$ , so  $\zeta = \phi$  and the derivative matrix  $\mathbf{D}^0$  will be composed of elements  $\{d_{il}\}$ . The discretized Maxwell equations can be written in this way:

$$\begin{aligned} {}^{n+1} E_i^\phi &= {}^n E_i^\phi - \frac{\Delta t}{\varepsilon} \frac{1}{\Delta z} \left[ \sum_I d_I {}^{n+\frac{1}{2}} H_{i-1}^\phi \right] \\ {}^{n+\frac{1}{2}} H_i^\phi &= {}^{n-\frac{1}{2}} H_i^\phi - \frac{\Delta t}{\mu} \frac{1}{\Delta z} \left[ \sum_I d_I {}^n E_{i-1}^\phi \right] \end{aligned} \quad (23)$$

Substituting (22) into (23), simplifying and using Euler's identity we get this set of equations:

$$\begin{aligned} 2E_0 \text{sen} \frac{\omega \Delta t}{2} &= \frac{\Delta t}{\varepsilon} \frac{1}{\Delta z} \left[ \sum_I d_I H_0 \text{sen}(-\tilde{k}l\Delta z) \right] \\ 2H_0 \text{sen} \frac{\omega \Delta t}{2} &= \frac{\Delta t}{\mu} \frac{1}{\Delta z} \left[ \sum_I d_I E_0 \text{sen}(-\tilde{k}l\Delta z) \right] \end{aligned} \quad (24)$$

and from them we obtain the dispersion relationship where  $c$  is the speed of light in our medium:

$$\frac{2\Delta z}{c\Delta t} \text{sen} \frac{\omega \Delta t}{2} = \sum_I d_I \text{sen}(-\tilde{k}l\Delta z) \quad (25)$$

This expression may be reduced to the ordinary expression  $\omega = c\tilde{k}$ , that is, the non-dispersive case, if spatial resolution  $\Delta z$  is very small in comparison with the wavelength. If Haar wavelet functions are used then we also obtain a non dispersive case at the stability factor  $s = 2$  (i.e. the maximum stable value). In any case, dealing with broadband signals, different expressions will be obtained depending on the relation between the wavelength  $\lambda$  and the

spatial resolution  $\Delta z$ , and on the type of wavelet function we use. In figure 4 it is plotted the normalized phase velocity versus spatial resolution given by the expression (25) for two different values of the stability factor. We can appreciate the feature mentioned before, that is, the normalized phase velocity tend to unity as we increase the resolution. It can also be seen that the higher the order of the wavelet function, the better dispersion characteristics.

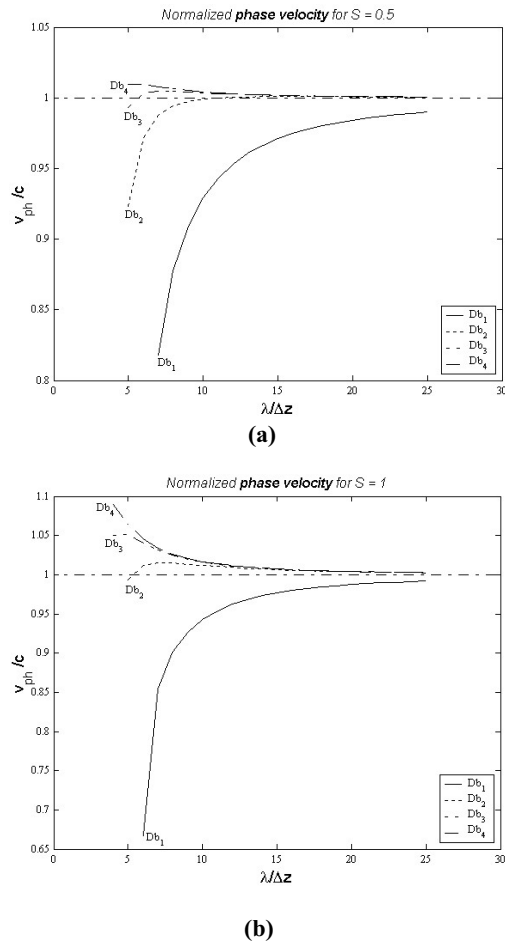


Fig. 4.- Normalized numerical phase velocity versus spatial resolution in lambda units for different wavelet functions:

- (a) with a stability factor  $s=0.5$ , and
- (b) with a stability factor  $s=1.0$

In figure 5 it is depicted a gaussian pulse propagation using different types of wavelet functions: (a) Haar wavelet functions, and (b) Daubechies  $D_2$  wavelet functions. The case (b) exhibit a better dispersive behaviour than the case (a) as it can be expected from previous figure 4.

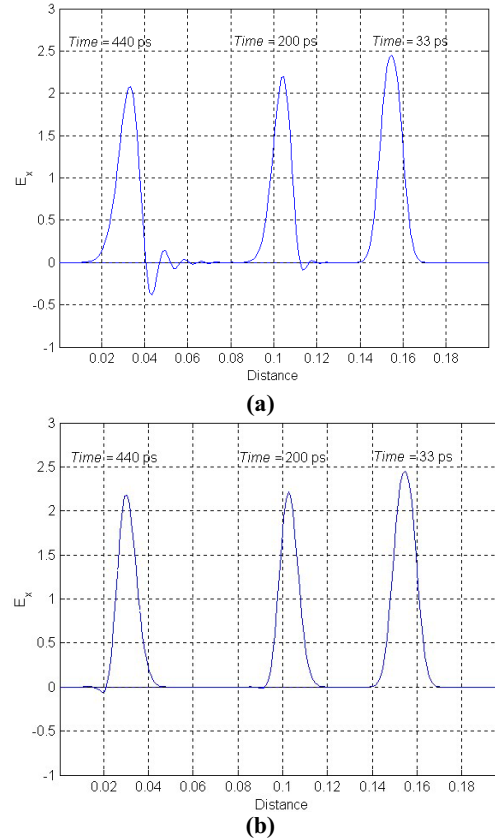


Fig. 5.- Three snapshots of a Gaussian pulse propagation using (a) Haar wavelet functions, and (b) Daubechies  $Db_2$  functions, showing it dispersion properties.

### 6.- Results

To validate our proposed technique some additional examples have been performed. First of all we have evaluated the multi-resolution property of the algorithm. To do that, we have simulated a gaussian pulse excitation into a one-dimensional cavity of 1 m long. The simulation domain is split into two parts of different resolution, one of high resolution on the left side and 400 mm long, and other part of low resolution on the right side and 600 mm long. Figure 6 displays this simulation where it can be clearly seen the differences between the two parts. Figure 7 shows in detail the transition between zones.

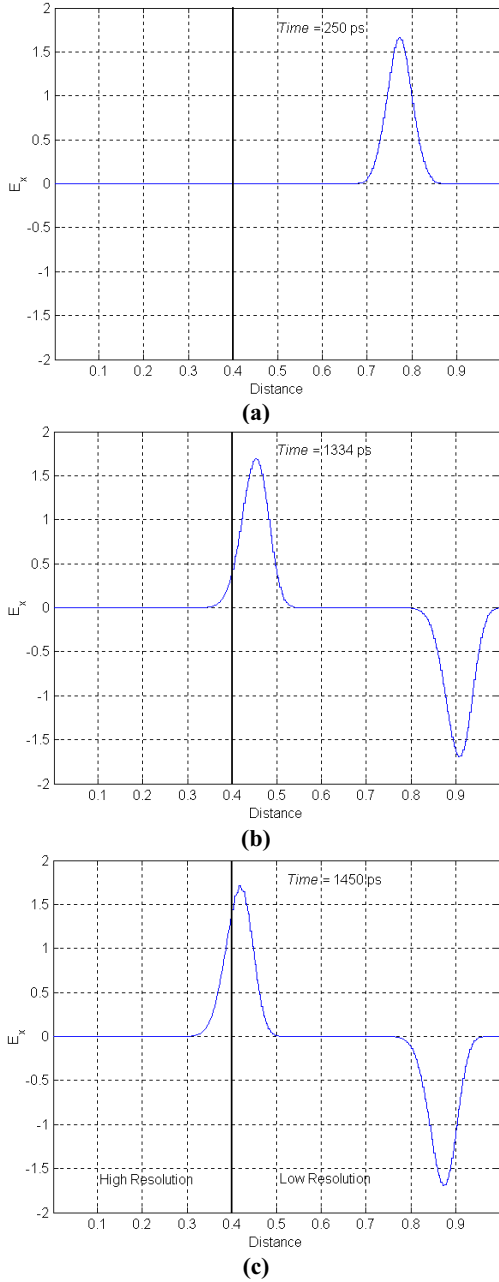


Fig. 6.- Gaussian pulse propagation using Haar wavelet functions. The simulation domain is split into two zones of different resolution.

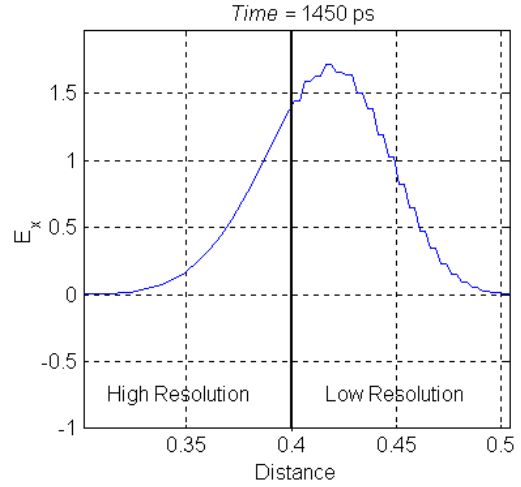


Fig. 7.- Details of the transition between two zones of different resolution.

We have also evaluated the resonant frequencies of a one-dimensional rectangular cavity with a 100 mm distance between electric walls (PEC). A spatial resolution of  $\Delta z = 0.625$  mm and a time discretization of  $\Delta t = 3.127$  ps have been chosen (that means, that, according to the stability criterion we choose  $s = 1.5$ ). The electric and magnetic fields are specified at  $t=0$  and at  $t=1/2\Delta t$  respectively,

$$E_k^0 = \exp\left[-\left(\frac{k - k_c}{k_w}\right)^2\right] \quad (26)$$

$$H_k^{\frac{1}{2}} = \exp\left[-\left(\frac{k - k_c - s/2}{k_w}\right)^2\right] \quad (27)$$

where the width of the pulse is  $k_w = 10$  and its center  $k_c = 80$  in terms of the index of the spatial mesh. After 4096 time steps with a spectral resolution of  $\Delta f = 78.1$  MHz, the resonance spectrum obtained have been plotted in figure 8

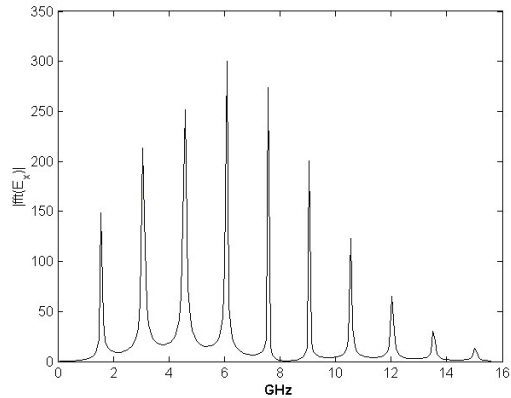


Fig. 8.- Resonant frequencies obtained in a cavity of length 100 mm using Haar wavelet functions.

## 7.- Conclusions

A new approach to Multi-Resolution in Time-Domain has been investigated. In this study a derivative matrix is used to calculate the spatial derivatives of the electromagnetic fields. This matrix acts on the coefficients of the wavelet expansions of the fields obtained from the Discrete Wavelet Transform. The use of this matrix allows us to solve the discretized Maxwell equations at any level of desired spatial resolution and wherever we may want. It has been shown that different types of Daubechies wavelet functions exhibit better dispersion properties for the same spatial resolution and that the time step can be chosen bigger than in other time-domain methods with the same mesh size. In this way, we can also choose at the beginning of the simulation different types of wavelet functions in order to improve our results.

## 9.- References

- [1] I. Daubechies, *Ten Lectures on Wavelets*, CBMS-NSF Ser. App. Math. 61, SIAM: Philadelphia 1992.
- [2] M. Krumpholz and L.P.B. Katehi, "MRTD: New Time-Domain schemes based on multiresolution analysis," *IEEE Trans. Microwave Theory Tech.* 1996; **44**(4):555-571.
- [3] M. Fujii and W.J.R. Hoefer, "A 3-D Haar-Wavelet-Based Multiresolution Analysis Similar to the FDTD Method – Derivation and Application –," *IEEE Trans. Microwave Theory Tech.* 1998; **46**(12):2463-2475.
- [4] Y. W. Cheong, Y. M. Lee, K. H. Ra, and C. C. Shin, "Wavelet-Galerkin scheme of time-dependent inhomogeneous electromagnetic problems," *IEEE Microwave Guided Wave Lett.* 1999, **9**(8):297-299.
- [5] R. F. Harrington, *Field Computation by Moment Methods*, IEEE Press: New York 1992.
- [6] S. Barmada and M. Raugi, "A general tool for circuit analysis based on wavelet transform," *Int. J. Circuit Theory and Applications.* 2000; **28**:461-480.
- [7] G. Beylkin, R. Coifman and V. Rokhlin, "Fast wavelet transform and numerical algorithms," *I. Comm. Pure Appl. Math.* 1991, **44**:141-183.
- [8] G. Beylkin, "On the representation of operators in bases of compactly supported wavelets," *SIAM J. Numer. Anal.* 1992; **6**(6):1716-1740.
- [9] A. Taflove, *Computational Electrodynamics: The Finite-Difference Time-Domain Method*, Artech House 1995.
- [10] C. Christopoulos, *The Transmission-Line Modelling Method: TLM*, IEEE MTT: New York 1995.
- [11] J. Represa, C. Pereira, M. Panizo, F. Tadeo, "A Simple Demonstration of Numerical Dispersion under FDTD," *IEEE Trans. Education.* 1997; **40**(1):98-102.
- [12] E.M. Tentzeris, R.L. Robertson, J.F. Harvey and L.P.B. Katehi, "Stability and Dispersion Analysis of Battle-Lemarie-Based MRTD Schemes," *IEEE Trans. Microwave Theory Tech.* 1999; **47**(7):1004-1013.
- [13] M. Fujii and W.J.R. Hoefer, "Dispersion of Time Domain Wavelet Galerkin Method Based on Daubechies' Compactly Supported Scaling Functions with Three and Four Vanishing Moments," *IEEE Microwave Guided Wave Lett.* 2000; **10**(4):125-127.



**César Represa** was born in Medina del Campo, Spain, in 1971. He received the *Licenciado* degree in Physics from the University of Valladolid in 1995, and the PhD degree in 2001 from the University of Burgos. He was *Profesor Asociado* at the University of Burgos from 1997 to 2000. Since 2000 he has been Assistant Professor at the University of Burgos. His research interest includes numerical methods in electromagnetics.



**Carmen Pereira** was born in Zamora, Spain, in 1951. She received the *Licenciado* degree in Physics in 1974, and the PhD degree in 1983, both from the University of Valladolid, Spain. She was Assistant Professor at the University of Valladolid from 1974 to 1985, and since 1985 has been *Profesor Titular* in Electromagnetics at the Universities of Valladolid and Burgos. Her current research interest includes numerical methods in electromagnetics and microwave devices.



**Ana Cristina L. Cabeceira** was born in Pontevedra, Spain, in 1969. She received the *Licenciada* Degree on Physics in 1992, and the Ph. D. Degree in 1996, both from the University of Valladolid, Spain. From 1992 to 1999 she was Assistant Professor,



then she become *Profesora Titular* in Electromagnetism of the University of Valladolid. Her main research interests include numerical methods for Electromagnetism, as well as characterization of electromagnetics properties of materials.



**Ismael Barba** was born in Palencia, Spain, in 1970. He received his *Licenciado* degree in Physics from the University of Valladolid in 1993. He received his MA degree in Electronical Engineering in 1995, and his PhD in Physics in 1997, all from the same University. He

was Assistant Professor from 1994 to 1999, and since 1999, he is *Profesor Titular* in Electromagnetics in the University of Valladolid. His main research interest includes numerical methods in electromagnetics, and characterization of electromagnetics properties of materials.



**José Represa** was born in Valladolid, Spain, in 1953. He received the *Licenciado* degree in Physics in 1976, and the PhD degree in 1984, both from the University of Valladolid, Spain. He was Assistant Professor from 1976 to 1985,

and since 1985 Professor in Electromagnetics at the University of Valladolid. His current research interest includes numerical methods in electromagnetics, characterization of electromagnetics properties of materials and microwave devices.

## 2003 INSTITUTIONAL MEMBERS

AUSTRALIAN DEFENCE LIBRARY  
Northcott Drive  
Campbell, A.C.T. 2600 AUSTRALIA

BAE SOWERBY RESEARCH CTR.  
FPC 267 Po Box 5  
Filton, Bristol, BS134 7QW  
UNITED KINGDOM

BAE SYSTEMS  
W423A, Warton Aerodrome  
Preston, PR41AY  
UNITED KINGDOM

BAE SYSTEMS, ADV. TECH. CTR  
W. Hanningfield Rd, Tech Centre Lib.  
Gt. Baddow, Chelms., CM2 8HN UK

BEIJING BOOK COMPANY, INC  
701 E Lindon Ave.  
Linden, NJ 07036-2495

CENTER HP COMPUTING  
PO Box 830657  
Birmingham, AL 35283-0657

CULHAM EM  
Bldg F5, Culham  
Abingdon, Oxford, OX14 3ED UK

DARTMOUTH COLL-FELDBERG LIB  
6193 Murdough Center  
Hanover, NH 03755-3560

DARMSTADT U. of TECHNOLOGY  
Schlossgartenstrasse 8  
Darmstadt, Hessen  
GERMANY D-64289

DEFENCE RESEARCH ESTAB. LIB.  
3701 Carling Avenue  
Ottawa, ON, K1A 0Z4 CANADA

DEPARTMENT OF PHYSICS  
Faculty of Sciences of Tunis  
El Manar, TUNISIA 2092

DTIC-OCP/IBRARY  
8725 John J. Kingman Rd. Ste 0944  
Ft. Belvoir, VA 22060-6218

ECI/NCHC  
12 Fl, No. 82, Sec. 2  
Fu Shing South Road  
Taipei, TAIWAN 106

EDINBURGH DSTO  
PO Box 830673  
Birmingham, AL 35283-0673

ELEC. COMM. LAB LIBRARY  
Hikarinooka Yokosuka Shi  
Kanagawa-Ken  
239-0847 MZ JAPAN

EM SOFTWARE & SYSTEMS  
PO Box 1354  
Stellenbosch, S. AFRICA 7599

EMBRAER SA  
Av Brig. Faruna Lima 2170  
Sao Paulo, BRAZIL 12227-901

ENGINEERING INFORMATION, INC  
PO Box 543  
Amsterdam, Netherlands 1000 Am

ERA TECHNOLOGY, LTD  
Cleeve Rd  
Leatherhead, Surrey, UK OX5 1JE

ETSE TELECOMUNICACION  
Biblioteca, Campus Lagoas  
Vigo, 36200 SPAIN

FANFIELD LTD  
Braxted Park  
Witham, Essex, CM8 3XB UK

FLORIDA INTERNATIONAL U.  
10555 W. Flagler St.  
ECE Dept., EAS-3983  
Miami, FL 33174

GEORGIA TECH LIBRARY  
225 North Avenue, NW  
Atlanta, GA 30332-0001

HANGANG UNIVERSITY / IS LIB.  
17 Haengdang-Dong, Seongdong KU  
Seoul, S KOREA 133-791

HKUST, UNIVERSITY LIBRARY  
Clear Water Bay Road  
Kowloon, HONG KONG

HOKKAIDO UNIVERSITY  
Kita 13, Nishi 8, KITA-KU  
Sapporo, JAPAN, 060-8628

HRL LABS, RESEARCH LIBRARY  
3011 Malibu Canyon  
Malibu, CA 90265

IEE INSPEC  
Acquisitions Section  
Michael Faraday House  
6 Hills Way  
Stevenage, Herts UK SG1 2AY

IIT RESEARCH INSTITUTE  
185 Admiral Cochrane Drive  
Annapolis, MD 21401-7396

IND CANTABRIA  
PO Box 830470  
Birmingham, AL 35283

INSTITUTE FOR SCIENTIFIC INFO.  
Publication Processing Dept.  
3501 Market St.  
Philadelphia, PA 19104-3302

INSYS LTD.  
Reddings Wood, Ampthill  
Bedford, MK45 2HD UK

IPS RADIO & SPACE SVC/LIBRARY  
PO Box 5606  
W. Chatswood, 2057 AUSTRALIA

LAND ENGINEERING CO.  
661 Bourke St.  
Melbourne, AUSTRALIA 3000

LEMA-EPFL  
ELB-ECUBLENS  
Lausanne, VD  
Switzerland CH-1015

LIBRARY of CONGRESS  
Reg. Of Copyrights  
Attn: 40T Deposits  
Washington DC, 20559

LINDA HALL LIBRARY  
5109 Cherry Street  
Kansas City, MO 64110-2498

MAAS  
16 Peachfield Road  
Great Malvern, Worc.  
WR 14 4AP UNITED KINGDOM

MISSISSIPPI STATE UNIV LIBRARY  
PO Box 9570  
Mississippi State, MS 39762

NA KANSAI KINOKUNNA CO.  
Attn: M. MIYOSHI  
PO Box 36 (NDLA KANSAI)  
Hongo, Tokyo, JAPAN 113-8688

NATIONAL INSTITUTE OF AIST  
AIST Tsukuba Central 2-1-1-1  
Umezono  
Tsukuba-Shi, Ibariki  
305-8568 JAPAN

NATL GROUND INTELLIGENCE  
220 7<sup>th</sup> Street N.E.  
Charlottesville, VA 22902-5307

NATL RADIOLOGICAL PROT. BD.  
Chilton, Didcot, OXON,  
OX11 0RG UK

NAVAL POSTGRADUATE SCHOOL  
Attn: J. Rozdal  
411 Dyer Rd./ Rm 111  
Monterey, CA 93943-5101

NAVAL RESEARCH LABORATORY  
C. Office, 4555 Overlook Avenue, SW  
Washington, DC 20375

OVIEDO LIBRARY  
LRC 04440  
PO Box 830679  
Birmingham, AL 35283

PENN STATE UNIVERSITY  
126 Paterno Library  
University Park, PA 16802-1808

PHILIPS RESEARCH LAB LIBRARY  
Cross Oak Lane, Salfords  
Redhill, RH1 5HA SURREY UK

QUEEN MARY & WESTFIELD  
COLLEGE  
Mile End Rd.  
London E1 4NS UK

QUEENSLAND CENTER, LIBRARY  
2643 Moggill Road  
Brisbane, QLD, 4069 AUSTRALIA

RENTON TECH LIBRARY/BOEING  
PO BOX 3707  
SEATTLE, WA 98124-2207

ABDUL SHUKKOOR  
Sheikh. Zayed Road, Apt. #1208  
P O Box 72409  
Dubai, UNITED ARAB EMIRATES

SOUTHWEST RESEARCH INST.  
6220 Culebra Road  
San Antonio, TX 78238

SWEDISH DEFENCE RESEARCH  
AGENCY  
P O Box 1165  
Linkoping, SWEDEN S-58111

SWETS BLACKWELL  
440 Creamery Way, Suite A  
Exton, PA 19341

TECHNISCHE INFORMATIONS  
BIBLIOTECH,  
1-1-2 Zeitschriftenzugang  
Welfelgarten 1B  
Hannover, GERMANY 30167

TECHNISCHE UNIV. DELFT  
Mekelweg 4, Delft, Holland, 2628 CD  
NETHERLANDS

TELSTRA RES. LABS LIBRARY  
770 Blackburn Road  
Clayton, VIC, 3168 AUSTRALIA

TOKYO KOKA UNIV  
1404-1 Katakura-Cho  
Hachioji, Tokyo, JAPAN 192-0914

UNIV OF CENTRAL FLORIDA LIB.  
PO Box 162666  
Orlando, FL 32816-2440

UNIV OF COLORADO LIBRARY  
Campus Box 184  
Boulder, CO 80309-0184

UNIV OF MISSOURI-ROLLA LIB.  
1870 Miner Circle  
Rolla, MO 65409-0001

US ARMY COLD REGION RES, LIB.  
72 Lyme Road  
Hanover, NH 03775-1290

RUBENS VALERIO  
2129 Flatbush Ave., #4000  
Brooklyn, NY 11234-4336

VECTOR FIELDS, LTD  
24 Bankside  
Kidlington, Oxford OX51JE



## ACES COPYRIGHT FORM

This form is intended for original, previously unpublished manuscripts submitted to ACES periodicals and conference publications. The signed form, appropriately completed, MUST ACCOMPANY any paper in order to be published by ACES. PLEASE READ REVERSE SIDE OF THIS FORM FOR FURTHER DETAILS.

TITLE OF PAPER:

AUTHORS(S)

PUBLICATION TITLE/DATE:

RETURN FORM TO:

Dr. Atef Z. Elsherbeni  
University of Mississippi  
Dept. of Electrical Engineering  
Anderson Hall Box 13  
University, MS 38677 USA

---

### PART A - COPYRIGHT TRANSFER FORM

(NOTE: Company or other forms may not be substituted for this form. U.S. Government employees whose work is not subject to copyright may so certify by signing Part B below. Authors whose work is subject to Crown Copyright may sign Part C overleaf).

The undersigned, desiring to publish the above paper in a publication of ACES, hereby transfer their copyrights in the above paper to The Applied Computational Electromagnetics Society (ACES). The undersigned hereby represents and warrants that the paper is original and that he/she is the author of the paper or otherwise has the power and authority to make and execute this assignment.

**Returned Rights:** In return for these rights, ACES hereby grants to the above authors, and the employers for whom the work was performed, royalty-free permission to:

1. Retain all proprietary rights other than copyright, such as patent rights.
2. Reuse all or portions of the above paper in other works.
3. Reproduce, or have reproduced, the above paper for the author's personal use or for internal company use provided that (a) the source and ACES copyright are indicated, (b) the copies are not used in a way that implies ACES endorsement of a product or service of an employer, and (c) the copies per se are not offered for sale.
4. Make limited distribution of all or portions of the above paper prior to publication.
5. In the case of work performed under U.S. Government contract, ACES grants the U.S. Government royalty-free permission to reproduce all or portions of the above paper, and to authorize others to do so, for U.S. Government purposes only.

**ACES Obligations:** In exercising its rights under copyright, ACES will make all reasonable efforts to act in the interests of the authors and employers as well as in its own interest. In particular, ACES REQUIRES that:

1. The consent of the first-named author be sought as a condition in granting re-publication permission to others.
2. The consent of the undersigned employer be obtained as a condition in granting permission to others to reuse all or portions of the paper for promotion or marketing purposes.

In the event the above paper is not accepted and published by ACES or is withdrawn by the author(s) before acceptance by ACES, this agreement becomes null and void.

---

AUTHORIZED SIGNATURE

TITLE (IF NOT AUTHOR)

---

EMPLOYER FOR WHOM WORK WAS PERFORMED

DATE FORM SIGNED

### Part B - U.S. GOVERNMENT EMPLOYEE CERTIFICATION

(NOTE: if your work was performed under Government contract but you are not a Government employee, sign transfer form above and see item 5 under Returned Rights).

This certifies that all authors of the above paper are employees of the U.S. Government and performed this work as part of their employment and that the paper is therefor not subject to U.S. copyright protection.

---

AUTHORIZED SIGNATURE

TITLE (IF NOT AUTHOR)

---

NAME OF GOVERNMENT ORGANIZATION

DATE FORM SIGNED

---

## PART C - CROWN COPYRIGHT

(NOTE: ACES recognizes and will honor Crown Copyright as it does U.S. Copyright. It is understood that, in asserting Crown Copyright, ACES in no way diminishes its rights as publisher. Sign only if *ALL* authors are subject to Crown Copyright).

This certifies that all authors of the above Paper are subject to Crown Copyright. (Appropriate documentation and instructions regarding form of Crown Copyright notice may be attached).

---

AUTHORIZED SIGNATURE

TITLE OF SIGNEE

---

NAME OF GOVERNMENT BRANCH

DATE FORM SIGNED

### Information to Authors

#### ACES POLICY

ACES distributes its technical publications throughout the world, and it may be necessary to translate and abstract its publications, and articles contained therein, for inclusion in various compendiums and similar publications, etc. When an article is submitted for publication by ACES, acceptance of the article implies that ACES has the rights to do all of the things it normally does with such an article.

In connection with its publishing activities, it is the policy of ACES to own the copyrights in its technical publications, and to the contributions contained therein, in order to protect the interests of ACES, its authors and their employers, and at the same time to facilitate the appropriate re-use of this material by others.

The new United States copyright law requires that the transfer of copyrights in each contribution from the author to ACES be confirmed in writing. It is therefore necessary that you execute either Part A-Copyright Transfer Form or Part B-U.S. Government Employee Certification or Part C-Crown Copyright on this sheet and return it to the Managing Editor (or person who supplied this sheet) as promptly as possible.

#### CLEARANCE OF PAPERS

ACES must of necessity assume that materials presented at its meetings or submitted to its publications is properly available for general dissemination to the audiences these activities are organized to serve. It is the responsibility of the authors, not ACES, to determine whether disclosure of their material requires the prior consent of other parties and if so, to obtain it. Furthermore, ACES must assume that, if an author uses within his/her article previously published and/or copyrighted material that permission has been obtained for such use and that any required credit lines, copyright notices, etc. are duly noted.

#### AUTHOR/COMPANY RIGHTS

If you are employed and you prepared your paper as a part of your job, the rights to your paper initially rest with your employer. In that case, when you sign the copyright form, we assume you are authorized to do so by your employer and that your employer has consented to all of the terms and conditions of this form. If not, it should be signed by someone so authorized.

**NOTE RE RETURNED RIGHTS:** Just as ACES now requires a signed copyright transfer form in order to do "business as usual", it is the intent of this form to return rights to the author and employer so that they too may do "business as usual". If further clarification is required, please contact: The Managing Editor, R. W. Adler, Naval Postgraduate School, Code EC/AB, Monterey, CA, 93943, USA (408)656-2352.

Please note that, although authors are permitted to re-use all or portions of their ACES copyrighted material in other works, this does not include granting third party requests for reprinting, republishing, or other types of re-use.

#### JOINT AUTHORSHIP

For jointly authored papers, only one signature is required, but we assume all authors have been advised and have consented to the terms of this form.

#### U.S. GOVERNMENT EMPLOYEES

Authors who are U.S. Government employees are not required to sign the Copyright Transfer Form (Part A), but any co-authors outside the Government are.

Part B of the form is to be used instead of Part A only if all authors are U.S. Government employees and prepared the paper as part of their job.

**NOTE RE GOVERNMENT CONTRACT WORK:** Authors whose work was performed under a U.S. Government contract but who are not Government employees are required so sign Part A-Copyright Transfer Form. However, item 5 of the form returns reproduction rights to the U. S. Government when required, even though ACES copyright policy is in effect with respect to the reuse of material by the general public.  
January 2002

## INFORMATION FOR AUTHORS

### PUBLICATION CRITERIA

Each paper is required to manifest some relation to applied computational electromagnetics. **Papers may address general issues in applied computational electromagnetics, or they may focus on specific applications, techniques, codes, or computational issues.** While the following list is not exhaustive, each paper will generally relate to at least one of these areas:

- 1 Code validation.** This is done using internal checks or experimental, analytical or other computational data. Measured data of potential utility to code validation efforts will also be considered for publication.
- 2 Code performance analysis.** This usually involves identification of numerical accuracy or other limitations, solution convergence, numerical and physical modeling error, and parameter tradeoffs. However, it is also permissible to address issues such as ease-of-use, set-up time, run time, special outputs, or other special features.
- 3 Computational studies of basic physics.** This involves using a code, algorithm, or computational technique to simulate reality in such a way that better, or new physical insight or understanding, is achieved.
- 4 New computational techniques** , or new applications for existing computational techniques or codes.
- 5 "Tricks of the trade"** in selecting and applying codes and techniques.
- 6 New codes, algorithms, code enhancement, and code fixes.** This category is self-explanatory, but includes significant changes to existing codes, such as applicability extensions, algorithm optimization, problem correction, limitation removal, or other performance improvement. **Note: Code (or algorithm) capability descriptions are not acceptable, unless they contain sufficient technical material to justify consideration.**
- 7 Code input/output issues.** This normally involves innovations in input (such as input geometry standardization, automatic mesh generation, or computer-aided design) or in output (whether it be tabular, graphical, statistical, Fourier-transformed, or otherwise signal-processed). Material dealing with input/output database management, output interpretation, or other input/output issues will also be considered for publication.
- 8 Computer hardware issues.** This is the category for analysis of hardware capabilities and limitations of various types of electromagnetics computational requirements. Vector and parallel computational techniques and implementation are of particular interest.

Applications of interest include, but are not limited to, antennas (and their electromagnetic environments), networks, static fields, radar cross section, shielding, radiation hazards, biological effects, electromagnetic pulse (EMP), electromagnetic interference (EMI), electromagnetic compatibility (EMC), power transmission, charge transport, dielectric, magnetic and nonlinear materials, microwave components, MEMS technology, MMIC technology, remote sensing and geometrical and physical optics, radar and communications systems, fiber optics, plasmas, particle accelerators, generators and motors, electromagnetic wave propagation, non-destructive evaluation, eddy currents, and inverse scattering.

Techniques of interest include frequency-domain and time-domain techniques, integral equation and differential equation techniques, diffraction theories, physical optics, moment methods, finite differences and finite element techniques, modal expansions, perturbation methods, and hybrid methods. This list is not exhaustive.

A unique feature of the Journal is the publication of unsuccessful efforts in applied computational electromagnetics. Publication of such material provides a means to discuss problem areas in electromagnetic modeling. Material representing an unsuccessful application or negative results in computational electromagnetics will be considered for publication only if a reasonable expectation of success (and a reasonable effort) are reflected. Moreover, such material must represent a problem area of potential interest to the ACES membership.

Where possible and appropriate, authors are required to provide statements of quantitative accuracy for measured and/or computed data. This issue is discussed in "Accuracy & Publication: Requiring, quantitative accuracy statements to accompany data," by E. K. Miller, *ACES Newsletter*, Vol. 9, No. 3, pp. 23-29, 1994, ISBN 1056-9170.

### EDITORIAL REVIEW

**In order to ensure an appropriate level of quality control** , papers are peer reviewed. They are reviewed both for technical correctness and for adherence to the listed guidelines regarding information content.

### JOURNAL CAMERA-READY SUBMISSION DATES

March issue	deadline 8 January
July issue	deadline 20 May
November issue	deadline 20 September

Uploading an acceptable camera-ready article after the deadlines will result in a delay in publishing this article.

## STYLE FOR CAMERA-READY COPY

The ACES Journal is flexible, within reason, in regard to style. However, certain requirements are in effect:

1. The paper title should NOT be placed on a separate page. The title, author(s), abstract, and (space permitting) beginning of the paper itself should all be on the first page. The title, author(s), and author affiliations should be centered (center-justified) on the first page.
2. An abstract is REQUIRED. The abstract should be a brief summary of the work described in the paper. It should state the computer codes, computational techniques, and applications discussed in the paper (as applicable) and should otherwise be usable by technical abstracting and indexing services.
3. Either British English or American English spellings may be used, provided that each word is spelled consistently throughout the paper.
4. Any commonly-accepted format for referencing is permitted, provided that internal consistency of format is maintained. As a guideline for authors who have no other preference, we recommend that references be given by author(s) name and year in the body of the paper (with alphabetical listing of all references at the end of the paper). Titles of Journals, monographs, and similar publications should be in italic font or should be underlined. Titles of papers or articles should be in quotation marks.
5. Internal consistency shall also be maintained for other elements of style, such as equation numbering. As a guideline for authors who have no other preference, we suggest that equation numbers be placed in parentheses at the right column margin.
6. The intent and meaning of all text must be clear. For authors who are NOT masters of the English language, the ACES Editorial Staff will provide assistance with grammar (subject to clarity of intent and meaning).
7. Unused space should be minimized. Sections and subsections should not normally begin on a new page.

## PAPER FORMAT

The preferred format for initial submission and camera-ready manuscripts is 12 point Times Roman font, single line spacing and double column format, similar to that used here, with top, bottom, left, and right 1 inch margins. Manuscripts should be prepared on standard 8.5x11 inch paper.

Only camera-ready electronic files are accepted for publication. The term **camera-ready** means that the material is neat, legible, and reproducible. Full details can be found on ACES site, Journal section.

ACES reserves the right to edit any uploaded material, however, this is not generally done. It is the author(s)

responsibility to provide acceptable camera-ready pdf files. Incompatible or incomplete pdf files will not be processed, and authors will be requested to re-upload a revised acceptable version.

## SUBMITTAL PROCEDURE

All submissions should be uploaded to ACES server through ACES web site (<http://aces.ee.olemiss.edu>) by using the upload button, journal section. Only pdf files are accepted for submission. The file size should not be larger than 5MB, otherwise permission from the Editor-in-Chief should be obtained first. The Editor-in-Chief will acknowledge the electronic submission after the upload process is successfully completed.

## COPYRIGHTS AND RELEASES

Each primary author must sign a copyright form and obtain a release from his/her organization vesting the copyright with ACES. Copyright forms are available at ACES, web site (<http://aces.ee.olemiss.edu>). To shorten the review process time, the executed copyright form should be forwarded to the Editor-in-Chief immediately after the completion of the upload (electronic submission) process. Both the author and his/her organization are allowed to use the copyrighted material freely for their own private purposes.

Permission is granted to quote short passages and reproduce figures and tables from and ACES Journal issue provided the source is cited. Copies of ACES Journal articles may be made in accordance with usage permitted by Sections 107 or 108 of the U.S. Copyright Law. This consent does not extend to other kinds of copying, such as for general distribution, for advertising or promotional purposes, for creating new collective works, or for resale. The reproduction of multiple copies and the use of articles or extracts for commercial purposes require the consent of the author and specific permission from ACES. Institutional members are allowed to copy any ACES Journal issue for their internal distribution only.

## PUBLICATION CHARGES

ACES members are allowed 12 printed pages per paper without charge; non-members are allowed 8 printed pages per paper without charge. Mandatory page charges of \$75 a page apply to all pages in excess of 12 for members or 8 for non-members. Voluntary page charges are requested for the free (12 or 8) pages, but are NOT mandatory or required for publication. A priority courtesy guideline, which favors members, applies to paper backlogs. Authors are entitled to 15 free reprints of their articles and must request these from the Managing Editor. Additional reprints are available to authors, and reprints available to non-authors, for a nominal fee.

**ACES Journal is abstracted in INSPEC, in Engineering Index, and in DTIC.**